

Rigorous bounds on energy dissipation in turbulent shear flow



DISSERTATION

zur Erlangung des Doktorgrades
der Naturwissenschaften
(Dr. rer. nat.)

dem Fachbereich Physik
der Philipps-Universität Marburg
vorgelegt

von

Rolf Nicodemus

aus Hannover

Marburg/Lahn 1997

Vom Fachbereich Physik der
Philipps-Universität als

Dissertation angenommen am: 08.10.97

Erstgutachter: Prof. Dr. Siegfried Großmann

Zweitgutachter: PD Dr. Martin Holthaus

Tag der mündlichen Prüfung: 31.10.97

**Meiner Mutter
gewidmet**

Contents

1 Überblick	5
1.1 Einleitung	5
1.2 Methodik und Ergebnisse	8
2 Improved variational principle for bounds on energy dissipation in turbulent shear flow	15
2.1 Introduction	15
2.2 Formulation of the variational principle	16
2.3 Plane Couette flow with one-dimensional background flows	20
2.4 Illustration	25
2.5 Conclusion: background flow and balance parameter belong together	30
3 Constructive approach to the variational principle	32
3.1 Introduction	32
3.2 Variational principle for plane Couette flow	33
3.3 Implementation of the spectral constraint	40
3.4 Minimization of the upper bound	45
3.5 Characteristic phenomena and problems	50
3.6 Results	52
3.7 Discussion and outlook	58

4	Asymptotic theory of dissipation bounds	62
4.1	Introduction	62
4.2	The two branches of the bifurcation plot	63
4.2.1	The lower branch	64
4.2.2	The upper branch	68
4.3	Scaling solutions to the variational principle	77
4.4	Variational principle for the asymptotic boundary layer shape function	83
4.5	Incorporating a variational parameter for the shape of the boundary segments	87
4.6	Conclusions: the principles behind the principle	90
5	Variational bound on energy dissipation in the unrestricted, three-dimensional plane Couette flow	92
5.1	Introduction	92
5.2	Evaluation of the spectral constraint	92
5.3	Results	97
5.4	Conclusions	107
A	Appendix	110
A.1	Boundary value problem for rescaled profile functions with “infinitely” extended interior	110
A.2	Compound matrix method for the sixth-order Sturm–Liouville problem	115
A.3	Neglecting divergence-freeness	118

List of Figures

2.1	Background flow profiles resulting from the variational principle with over-restrictive profile constraint	27
2.2	Balance parameter a resulting from the variational principle with over-restrictive profile constraint	28
2.3	Bounds on the dimensionless energy dissipation rate $c_\varepsilon(Re)$ derived from the variational principle with over-restrictive profile constraint	29
3.1	Graph of an upper bound on c_ε produced by a generic profile ϕ	39
3.2	Behaviour of $f_1(z)$ for a generic profile ϕ and typical parameters k and R	44
3.3	$f_1(1)$ as a function of R	45
3.4	Behaviour of $R_0\{\phi\}(k)$ as a function of k for a generic profile ϕ	46
3.5	Example of a profile ϕ	47
3.6	Graph of \bar{c}_ε that emerges when the slope p is varied while the width δ of the boundary layers is kept fixed	48
3.7	Illustration of the envelope technique for obtaining optimal upper bounds on c_ε .	49
3.8	Bounds on c_ε for the Couette flow without spanwise degrees of freedom	53
3.9	Balance parameter a for the optimal upper bound on c_ε as a function of the Reynolds number	54
3.10	Optimal parameter δ , which denotes the thickness of the profiles' boundary layers, as a function of the Reynolds number	55
3.11	Optimal parameter p , which denotes the slope of the profiles in the interior, as a function of the Reynolds number	56
3.12	Wavenumber(s) k that minimize $R_0\{\phi\}(k)$, as function(s) of Re	57
3.13	Bounds on c_ε for the unrestricted, three-dimensional Couette flow	60

3.14	Comparison of bounds on c_ε	61
4.1	Comparison of $2\delta k_2/2\pi$, as obtained from the numerical solution, to the constant value (4.58)	76
4.2	Comparison of the optimized parameter δ , as obtained in the numerical solution, to the scaling solution (4.66)	81
4.3	Comparison of the optimized parameter p , as obtained in the numerical solution, to the scaling solution (4.66)	81
4.4	Comparison of the upper bound on c_ε , as obtained numerically, to the asymptotic bound resulting from the scaling solution (4.66)	82
4.5	Graphs of $\psi_{bl}^{(n)}$ for some values of n between 2 and 100	85
4.6	Improved variational bounds on c_ε for the Couette flow without spanwise degrees of freedom	88
5.1	Behaviour of $\phi^{(2)}(z)/\phi'(z)$ in the interval $0 \leq z \leq 0.015$ for $\delta = 0.5$ and $n = 1000$	99
5.2	Behaviour of $\phi^{(2)}(z)/\phi'(z)$ in the vicinity of $z = \delta$ for $\delta = 0.002$ and $n = 4$	99
5.3	Test profile $\phi(z)$ for a generic parameter set	100
5.4	Bounds on c_ε for the unrestricted, three-dimensional plane Couette flow	101
5.5	Three-dimensional surface plot visualizing the \mathbf{k} -dependence of $R_0\{\phi\}(\mathbf{k})$ for the laminar profile	104
5.6	Three-dimensional surface plot visualizing the \mathbf{k} -dependence of $R_0\{\phi\}(\mathbf{k})$ for the optimized profile belonging to the absolute minimum of the upper bound on c_ε	104
5.7	Minimizing wavenumber(s) k_y corresponding to the upper bound on c_ε displayed in figure 5.4	105
5.8	Three-dimensional plot visualizing the metamorphosis of the optimized variational profiles with the increase of the Reynolds number	106
5.9	Comparison of bounds on $c_\varepsilon(Re)$ for the unrestricted, three-dimensional plane Couette flow	108
A.1	Bounds on $c_\varepsilon(Re)$ for the plane Couette flow obtained by neglecting the condition $\nabla \cdot \mathbf{V} = 0$	120

1 Überblick

1.1 Einleitung

Mathematisch strenge und gleichzeitig nicht-triviale Aussagen sind die Juwelen einer jeden physikalischen Theorie. Für die Turbulenz-Theorie gilt dies in besonderem Maße, da hier einerseits nur wenige exakte Aussagen bekannt sind, und andererseits wesentliche Fragestellungen, wie z.B. die Frage nach der Existenz von Intermittenz-Korrekturen im Inertialbereich weder mit Hilfe numerischer Simulationen noch mit Hilfe von Näherungslösungen für die Bewegungsgleichungen oder gar Modellbildungen zufriedenstellend zu beantworten sind. Volle numerische Simulationen müssen sich aufgrund der enormen Anzahl relevanter Freiheitsgrade auf relativ kleine Reynolds-Zahlen beschränken, und dies wird trotz der rasanten Entwicklung der Computer-Technologie noch lange so bleiben. Bei Näherungslösungen oder Modellbildungen hängen die Ergebnisse sehr stark von den gemachten Näherungen bzw. Annahmen ab. Es bleibt die Herausforderung, strenge Aussagen auf der Basis der Navier–Stokes Gleichung zu gewinnen.

In diese Richtung weist eine vor kurzem von Doering & Constantin (1994) eingeführte Methode, deren Ziel eben nicht die näherungsweise Lösung der Bewegungsgleichungen, sondern die Angabe *rigoroser Schranken* für wesentliche, ein turbulentes System charakterisierende Größen ist. Eine solche Größe ist die Energiedissipationsrate ε . Turbulente Systeme müssen immer als offene Systeme aufgefaßt werden: Energie wird von außen auf den großen Längenskalen eingefüttert, durch die turbulente Dynamik auf die verschiedenen Skalen umverteilt und schließlich auf der dissipativen Längenskala η durch Reibung in Wärme umgesetzt. Somit kommt dem Energie-durchfluß durch das System eine ähnliche Rolle zu wie der Freien Energie in abgeschlossenen thermodynamischen Systemen. Die fundamentale Bedeutung von ε wird dadurch unterstrichen, daß die klassischen Turbulenz-Theorien (siehe Kolmogorov 1941; Obukhov 1941; von Weizsäcker 1948; Heisenberg 1948; Onsager 1945) erstaunlich viele Phänomene in turbulenten Strömungen, wie z.B. das Skalenverhalten der Strukturfunktion zweiter Ordnung oder das Wellenzahlspektrum, erklären konnten, indem sie diese Größen über Dimensionsargumente mit ε verknüpften. Darüber hinaus schlagen sich die Intermittenz-Korrekturen (dies sind gerade die Korrekturen zum klassischen Skalenverhalten) unter Umständen direkt in der Re -Abhängigkeit des Dissipations-Beiwertes c_ε nieder (Grossmann 1995; Stolovitzky & Sreenivasan 1995). Der Dissipations-Beiwert c_ε bezeichnet ε in den durch die äußeren Skalen vorgegebenen Einheiten.

Somit wurde das neue, von Doering & Constantin (1994) entwickelte Verfahren zur Berechnung mathematisch strenger *oberer* Schranken für die Energiedissipationsrate in turbulenten Strömungen von der Fachwelt mit großem Interesse aufgenommen. Doering und Constantin belebten eine auf Hopf (1941) zurückgehende Idee wieder, ein mathematisches Geschwindigkeits-Hilfsfeld als Träger der physikalischen Randbedingungen einzuführen. Ausgehend von der Aufspaltung des physikalischen Geschwindigkeitsfeldes in diesen sogenannten Hintergrund-Fluß (“background flow”) und Abweichungen von diesem, leiteten sie aus den Bewegungsgleichungen eine obere Schranke für ε als Lösung eines Variationsprinzips für den Hintergrund-Fluß her. Charakteristisch für dieses Variationsprinzips ist seine spektrale Nebenbedingung (“spectral constraint”): Bei gegebener Reynolds-Zahl sind nur solche Hintergrund-Flüsse für die Variation zulässig, die sicherstellen, daß alle Eigenwerte eines gewissen Eigenwertproblems positiv sind. Der Schrankencharakter der Theorie resultiert aus der Vergrößerung des mathematischen Funktionenraumes für die Abweichungen vom Hintergrund-Fluß. Getragen wird die Formulierung eines solchen Variationsprinzips von der Hoffnung, daß es einerseits technisch handhabbar ist, aber andererseits wesentliche Aspekte des dynamischen Flüssigkeitssystems erfaßt werden.

Tatsächlich ist die Idee, im Rahmen von Variationsprinzipien Schranken für Größen zu berechnen, die Transporteigenschaften turbulenter Strömungen charakterisieren, nicht neu. Sie war bereits in den Arbeiten von Howard und Busse (Howard 1972; Busse 1970, 1978; siehe auch Busse 1996) sehr lebendig, fiel jedoch danach in einen 25 Jahre andauernden Dornröschenschlaf. Ausgangspunkt in Busses Optimum-Theorie (Busse 1970, 1978) ist die Zerlegung des turbulenten Geschwindigkeitsfeldes in einen schichtgemittelten Anteil und die Fluktuationen um diesen. Das resultierende nichtlineare Euler–Lagrange-Problem konnte von Busse im asymptotischen Limes, d.h. für Scherströmungen im Limes $Re \rightarrow \infty$, unter gewissen Näherungen gelöst werden. Trotz offensichtlicher Unterschiede in der Formulierung der Variationsprinzipien von Doering und Constantin auf der einen Seite und von Busse auf der anderen konnte Kerswell (1997) eine enge Verwandtschaft zwischen beiden Methoden aufdecken. Indem er das Doering–Constantin-Variationsprinzip auf ein dem Busse’schen Euler–Lagrange-Problem sehr verwandtes Problem abbildete und dann Busses asymptotische Lösungstechnik auf die neuen Gleichungen anwandte, konnte Kerswell anhand der Beispiele der Energiedissipationsrate in ebenen Scherströmungen und des Wärmetransportes in Rayleigh–Bénard-Konvektion zeigen, daß im asymptotischen Limes beide Methoden zu den gleichen Schranken führen. Es muß betont werden, daß diese Übereinstimmung nicht für die ursprüngliche Formulierung des Variationsprinzips von Doering & Constantin (1994) gilt, sondern erst für die in dieser Arbeit vorgestellte verbesserte Formulierung zutrifft (siehe Kapitel 2 der vorliegenden Arbeit sowie Nicodemus, Grossmann & Holthaus 1997a). Man muß klar sehen, daß Kerswell durch die Übertragung der Busse’schen sogenannten multi- α Lösungen auch die ihnen innewohnenden Näherungen übernimmt. Ferner ist bislang ungeklärt inwieweit diese Lösungen tatsächlich extremal sind. Strenge Aussagen für

endliche Reynolds-Zahlen, insbesondere für den wichtigen Bereich des Turbulenz-Einsatzes, sind mit diesen Lösungen nicht möglich.

Auch wenn durch das Kerswell'sche Resultat seine Grenzen abgesteckt werden, besticht das (erweiterte) Doering–Constantin-Prinzip durch große konzeptionelle Klarheit und Flexibilität in der Anwendbarkeit. Die Benutzung von Schichtmitteln führt in der Busse'schen Formulierung zwangsläufig zu starken Einschränkungen der Übertragbarkeit auf komplexere Geometrien. Derartige Einschränkungen sind in der neuen Formulierung nicht erkennbar. Des weiteren ist man bei der Berechnung von strengen oberen Schranken nicht auf die extremale Lösung des Variationsprinzips unter Berücksichtigung der eigentlichen spektralen Nebenbedingung angewiesen. Zum Beispiel kann man mittels funktionaler Abschätzungen zu stark vereinfachten Nebenbedingungen kommen, die analytische Lösungen für alle Reynolds-Zahlen zulassen (Doering & Constantin 1992, 1994, 1996; Marchioro 1994; Constantin & Doering 1995; Gebhardt *et al.* 1995; Nicodemus *et al.* 1997a). Die so gewonnenen Schranken sind im wesentlichen strukturlos und von der "Qualität" her, d.h. im Hinblick auf die Abweichungen von experimentellen Werten, nicht mit der Busse'schen asymptotischen Schranke vergleichbar. Selbst bei Einbeziehung der vollen, uneingeschränkten spektralen Nebenbedingung liegt ein entscheidender Vorteil der neuen Formulierung in der Tatsache, daß jeder beliebige, den Randbedingungen genügende Hintergrundfluß eine strenge obere Schranke für die Energiedissipationsrate liefert, die sich bis zu einer kritischen Reynolds-Zahl R_c , welche über Auswertung der spektralen Nebenbedingung zu berechnen ist, erstreckt. Genau diese Tatsache ist Ausgangspunkt für die in dieser Arbeit vorgestellte *konstruktive Lösung des Variationsprinzips unter Einbeziehung der vollen, uneingeschränkten spektralen Nebenbedingung* für alle Reynolds-Zahlen von praktischem Interesse. Dabei ist unser Augenmerk nicht nur auf die Berechnung der bestmöglichen Schranke gerichtet, sondern ganz besonders auf die *strukturellen Merkmale, die diese Schranke hervorbringen*, um so letztendlich tiefere physikalische Einsichten zu gewinnen.

Die vorliegende Dissertation gliedert sich in folgender Weise: Orientiert am konkreten Beispiel der ebenen Couette-Strömung, folgt nach dieser Übersicht in Kapitel 2 die Formulierung des erweiterten Doering–Constantin-Prinzips zur Berechnung rigoroser oberer Schranken für die Energiedissipationsrate. Hier wird auch eine Unzulänglichkeit der ursprünglichen Formulierung von Doering & Constantin (1994) beseitigt. Kapitel 3 widmet sich der methodischen Implementierung der spektralen Nebenbedingung im Rahmen einer konstruktiven Lösung des Variationsprinzips. Dabei wird das Modell der ebenen Scherströmung ohne Freiheitsgrade in spannweiser Richtung herangezogen. Für dieses zwei-dimensionale Modell wird in Kapitel 4 eine asymptotische Theorie entwickelt, die wesentliche strukturelle Einsichten liefert. Die anhand des zwei-dimensionalen Modells gewonnenen Erkenntnisse werden schließlich in Kapitel 5 auf das uneingeschränkte, drei-dimensionale ebene Couette-Problem übertragen.

1.2 Methodik und Ergebnisse

Beide Methoden, die ursprüngliche Formulierung des Doering–Constantin-Prinzips auf der einen Seite und Busses Optimum-Theorie auf der anderen, sind konzeptionell eng verwandt mit der Energiestabilitätstheorie (siehe Joseph 1976; Drazin & Reid 1981). Diese liefert für eine Strömung bei gegebener Geometrie eine strenge Grenze in der Reynolds-Zahl, bis zu welcher die laminare Lösung für die betrachtete Geometrie in dem folgenden Sinne stabil ist: Jede beliebig große und beliebig geartete Abweichung von der laminaren Lösung zerfällt von Anfang an mindestens exponentiell in der Zeit. Für die ebene Scherströmung folgt, daß die lineare laminare Lösung bis zur Energiestabilitätsgrenze $Re_{ES} \approx 82.65$ in diesem Sinne stabil ist¹. Der Langzeit-Limes des Dissipations-Beiwertes c_ε ergibt sich somit zu $c_\varepsilon(Re) = Re^{-1}$ für $Re < Re_{ES}$. Während die Busse'sche Theorie dieses Ergebnis formal reproduziert (Busse 1970, 1978), mußte im Rahmen des ursprünglichen Doering–Constantin-Prinzips die laminare Lösung als optimaler Hintergrund-Fluß, der unmittelbar $c_\varepsilon(Re) = Re^{-1}$ als gemeinsame obere und untere Schranke für den Dissipations-Beiwert liefert, schon bei $Re = \frac{1}{2}Re_{ES}$ verlassen werden. Dieser fehlende Faktor 2 in der Reynolds-Zahl ist eine offensichtliche Unzulänglichkeit. Um eine "gesunde" theoretische Basis zu schaffen, müssen Ursprung, Konsequenzen und die Möglichkeit der Behebbarkeit dieses grundsätzlichen Mankos geklärt werden. Kapitel 2 (siehe auch Nicodemus *et al.* 1997a) widmet sich diesem Problem.

In der Tat ist es möglich, diesen Mangel zu beheben, indem man bewußt der naheliegenden Versuchung widersteht, den unangenehm erscheinenden Kreuzterm, der sowohl den Hintergrund-Fluß als auch die Abweichungen von diesem beinhaltet, zu eliminieren. Die Elimination dieses Kreuzterms in der ursprünglichen Formulierung implizierte eine feste, unflexible Gewichtung der verschiedenen Beiträge zur Energiedissipationsrate ε . Deshalb hat es sich als sinnvoll erwiesen, hier einen Gewichtungparameter ("balance parameter") a einzuführen. Als zusätzlicher Freiheitsgrad für die Variation ermöglicht dieser eine Reynolds-Zahl-abhängige Optimierung der relativen Gewichtung der verschiedenen Beiträge. Abgesehen davon, daß nun die laminare Lösung als optimaler Hintergrund-Fluß bis $Re = Re_{ES}$ zulässig wird, ergibt sich eine deutliche Verbesserung der Schranke für alle Reynolds-Zahlen. Im Limes asymptotisch großer Re gewinnt man einen Faktor $27/32$. Es muß betont werden, daß der zusätzliche Variationsparameter a keine technische Verkomplizierung des Variationsprinzips nach sich zieht, da die spektrale Nebenbedingung im wesentlichen unverändert bleibt; die Reynolds-Zahl wird lediglich durch eine reskalierte Reynolds-Zahl ersetzt.

¹Die Reynolds-Zahl ist hier definiert als:

$$Re \equiv \frac{(\text{relative Schergeschwindigkeit } U \text{ der Platten}) \times (\text{Abstand } h \text{ der Platten})}{\text{kinematische Viskosität } \nu}.$$

Des weiteren wird durch die neue Formulierung des Variationsprinzips das Verhalten der optimalen oberen Schranke für den Dissipations-Beiwert direkt an der Energiestabilitätsgrenze geklärt. Ergab die analytische Arbeit von Gebhardt *et al.* (1995) basierend auf der ursprünglichen Formulierung von Doering und Constantin — die spektrale Nebenbedingung wurde mittels funktionaler Abschätzungen berücksichtigt — einen stetig differenzierbaren Verlauf der Schranke an der vermeintlichen “Energiestabilitätsgrenze”, so folgt nun bei analogem Vorgehen ein zwar stetiges, aber nicht stetig differenzierbares Verhalten an der entsprechenden Stelle, siehe Abbildung 2.3. Es zeigt sich, daß dieser Knick im Verlauf der oberen Schranke in gleicher Weise auch bei Berücksichtigung der vollen, uneingeschränkten spektralen Nebenbedingung auftritt: *Die Schranke für den Dissipations-Beiwert steigt direkt oberhalb der Energiestabilitätsgrenze Re_{ES} an*, wie in Abbildung 5.4 gezeigt. Dieses nicht-glatte Verhalten der oberen Schranke geht einher mit einer Unendlichkeitsstelle des Gewichtungsparmeters a an der Stelle $Re = Re_{ES}$, siehe auch Abbildungen 2.2 und 3.9. An einen Phasenübergang erinnernd ändert sich die Interpretation der Abweichungen vom Hintergrund-Fluß sprunghaft beim Übergang von $Re < Re_{ES}$ nach $Re > Re_{ES}$. Für Reynolds-Zahlen unterhalb der Energiestabilitätsgrenze stellen die Abweichungen physikalische Fluktuationen um die laminare Lösung der Bewegungsgleichungen dar und zerfallen exponentiell in der Zeit. Somit liefern die Abweichungen keinen Beitrag zum Langzeit-Limes des Dissipations-Beiwertes, welcher folglich allein durch die Dissipation in der laminaren Strömung bestimmt wird. Für $Re > Re_{ES}$ ist die Situation anders: Die optimierten Hintergrund-Flüsse sind nun keine stationären Lösungen der Bewegungsgleichungen, und die Abweichungen, die nicht mehr als physikalische Fluktuationen im einfachen Sinne interpretiert werden können, tragen sehr wohl zur Gesamtdissipation bei.

Nachdem die Unstimmigkeiten der ursprünglichen Formulierung des Variationsprinzips in einfacher und befriedigender Weise aus dem Weg geräumt sind, widmet sich Kapitel 3 (siehe auch Nicodemus, Grossmann & Holthaus 1997b) der eigentlichen (numerischen) Lösung des Prinzips. Wie schon erwähnt, erfolgt die methodische Entwicklung eines konstruktiven Lösungsverfahrens, welches dann auf andere, kompliziertere Strömungen angewandt werden kann, also insbesondere auf die uneingeschränkte Couette-Strömung, am Modell der ebenen Scherströmung ohne Freiheitsgrade in spannweiser Richtung. Dabei charakterisieren wir den Hintergrund-Fluß durch ein nur höhenabhängiges Profil $\phi(z)$; z ist die Koordinate quer zur Strömungsrichtung. Ausgangspunkt des Lösungsverfahrens ist die Beobachtung, daß jede den Randbedingungen genügende Profilkfunktion ϕ eine strenge obere Schranke für den Dissipations-Beiwert bis zu einer maximalen Reynolds-Zahl $R_c\{\phi\}$ liefert (siehe Abbildung 3.1 zur Illustration). Betrachtet man nun alle Graphen dieser oberen Schranken in der (Re, c_ε) -Ebene, jeder einzelne hervorgerufen von einer konkreten Profilkfunktion, so ergibt sich die optimale *obere Schranke für $c_\varepsilon(Re)$ als untere Einhüllende* dieser Graphen. Der entscheidende Punkt ist nun, *daß die Nichtlinearität des Variationsprinzips effektiv auseinandergesogen werden kann*. Da $R_c\{\phi\}$ diejenige reskalierte Reynolds-Zahl ist, bei der der kleinste Eigenwert des die spektrale Nebenbedingung verkörpernden Eigen-

wertproblems gerade Null wird, reduziert sich die Implementierung der spektralen Nebenbedingung für jedes konkrete, vorgegebene Profil ϕ auf die Auswertung eines *linearen* Eigenwertproblems. Die Nichtlinearität steckt dann in der davon unabhängigen Konstruktion der Hüllkurve in der (Re, c_ε) -Ebene. Um dieses ganze Verfahren numerisch durchführen zu können, muß eine geeignet parametrisierte Klasse von Test-Profilfunktionen ausgewählt werden.

Für die praktische Berechnung der kritischen Reynolds-Zahl wird das relevante Eigenwertproblem in zwei Schritten äquivalent umgeformt: Im ersten Schritt schreiben wir das Eigenwertproblem, dessen Eigenfunktionen stationäre Geschwindigkeitsfelder sind, unter Berücksichtigung der periodischen Randbedingungen in Strömungsrichtung in ein Sturm–Liouville-Eigenwertproblem um. In einem zweiten Schritt wird dieses Sturm–Liouville-Problem mittels der sogenannten *Compound-Matrix-Methode* (siehe z.B. Straughan 1992) in eine numerisch handhabbare Form gebracht. Der entscheidende Punkt hierbei ist die Umsetzung der symmetrischen Randbedingungen des Sturm–Liouville-Problems in Anfangsbedingungen für alle Komponenten des resultierenden Gleichungssystems, ergänzt durch eine zusätzliche einfache Randbedingung für nur eine Komponente. Die Lösung dieses Anfangswertproblems mit Randbedingung liefert dann diejenige reskalierte Reynolds-Zahl $R_0\{\phi\}(k_x)$, bei der für vorgegebene Profildfunktion ϕ und fixierte Wellenzahl k_x in Strömungsrichtung der kleinste Eigenwert Null wird. Die gesuchte kritische Reynolds-Zahl $R_c\{\phi\}$ ergibt sich schließlich aus der Minimierung über alle Wellenzahlen k_x .

Als vielversprechende Klasse von Test-Profilfunktionen bietet sich zunächst eine zwei-parametrische Funktionenschar an (siehe Abbildung 3.5): Parabolische Randsegmente der Dicke δ werden stetig differenzierbar durch ein lineares Profilstück mit Steigung p verbunden. Die Ergebnisse, die das Variationsprinzip für diese Klasse von Test-Profilfunktionen liefert, sind für einen großen Reynolds-Zahl-Bereich — von der Energiestabilitätsgrenze des Couette-Systems ohne Freiheitsgrade in spannweiser Richtung bis zu $Re > 10^7$, d.h. bis weit in den asymptotischen Bereich — in den Abbildungen 3.8 bis 3.12 zusammengefaßt. Unerwarteterweise ist das strukturbestimmende Element eine *Bifurkation der minimierenden Wellenzahlen* (Abbildung 3.12): Oberhalb von $Re_B \approx 860$ selektiert das Variationsprinzip solche Profile zur Minimierung der oberen Schranke, für die der kleinste Eigenwert des Eigenwertproblems der spektralen Nebenbedingung entartet ist, d.h. *zwei Eigenwerte zu verschiedenen k_x -Werten passieren gleichzeitig die Null*. Der untere Ast der minimierenden Wellenzahlen ($k_{x,1}$) nimmt asymptotisch einen konstanten Wert an; dieser stimmt im Rahmen der numerischen Genauigkeit mit dem k_x -Wert überein, der die Energiestabilitätsgrenze als kritische Reynolds-Zahl für das laminare Profil festlegt. Der obere Ast der minimierenden Wellenzahlen ($k_{x,2}$) skaliert im asymptotischen Limes proportional zu Re . Mit der Aufspaltung der minimierenden k_x -Werte ändert sich abrupt das Verhalten der beiden optimierten Profilparameter δ und p (Abbildungen 3.10 und 3.11), beide skalieren umgekehrt proportional zu Re im Limes großer Reynolds-Zahlen. Dies alles übersetzt sich in eine deutlich ausgeprägte Minimumstruktur im Verlauf der oberen Schranke $\bar{c}_\varepsilon(Re)$ für den Dissipationsbeiwert $c_\varepsilon(Re)$ (Abbildung 3.8): Unterhalb von Re_B deutet sich ein $Re^{-1/4}$ -Abfall an. Dieser

wird durch die Bifurkation der Wellenzahlen abgefangen, und nach Durchlaufen eines Minimums bei $Re \approx 1000$ nimmt die Schranke *von unten* kommend ihren (konstanten) asymptotischen Wert an. Bemerkenswerterweise entspricht das $Re^{-1/4}$ -Verhalten genau dem Skalenverhalten, das Busse für eine “single”- α Lösung erhält (Busse 1970, 1978; siehe auch Kerswell 1997), während das asymptotische Re^0 -Verhalten identisch mit dem Busse’schen asymptotischen Skalenverhalten ist und in Übereinstimmung mit den klassischen Turbulenz-Theorien steht.

Viele der numerischen Beobachtungen aus Kapitel 3 finden ihre analytische Erklärung in dem folgenden Kapitel 4 (siehe auch Nicodemus, Grossmann & Holthaus 1997c), welches ein Kernstück der vorliegenden Arbeit bildet. Zunächst kann für sehr allgemeine Klassen von Profilfunktionen, die die Ausbildung von Randschichten zulassen, das Auftreten von (mindestens) zwei Ästen minimierender k_x -Wellenzahlen mathematisch streng gezeigt werden. Technisches Hilfsmittel hierbei sind zwei unabhängige Form-Funktionen (“shape functions”), die die Form der Randschichten der Profile bzw. ihrer Mittelschicht beschreiben. Für die den numerischen Untersuchungen in Kapitel 3 zugrundeliegende Funktionenschar wird das Bifurkations-Diagramm (Abbildung 3.12) für große Reynolds-Zahlen *qualitativ und quantitativ* verstanden. Insbesondere erweist sich die auffällige numerische Koinzidenz des asymptotischen k_x -Wertes des unteren Astes mit dem k_x -Wert an der Energiestabilitätsgrenze als exakte Identität. Schränkt man die Klasse von Profilfunktionen durch eine zusätzliche Monotoniebedingung ein, so folgt weiterhin im Limes großer Reynolds-Zahlen als Konsequenz des Variationsprinzips die Gleichschaltung der beiden Minima von $R_0(k_x)$, d.h. die Entartung der beiden kleinsten Eigenwerte des relevanten Eigenwertproblems bei ihrem Nulldurchgang. Hieraus ergibt sich zwingend ein Skalenverhalten der Profilparameter mit der Reynolds-Zahl. Dieses streng aus dem nichtlinearen Variationsprinzip hergeleitete Skalenverhalten stellt eine Präzisierung des in Kapitel 3 numerisch gefundenen Skalenverhaltens der beiden Profilparameter δ und p dar. Angewandt auf die den numerischen Untersuchungen zugrundeliegende Profilschar erhält man asymptotische Skalenlösungen für die Parameter δ und p , sowie für die obere Schranke $\bar{c}_\varepsilon(Re)$, siehe Abbildungen 4.2 bis 4.4. Für $Re > 2000$ ergibt sich eine bemerkenswerte Übereinstimmung mit den numerisch gefundenen Ergebnissen. Insbesondere muß der dem Minimum folgende Anstieg von \bar{c}_ε bereits als Teil der Asymptotik interpretiert werden.

Ausgehend von dieser Analyse ist es möglich, ein neues Variationsprinzip für den asymptotischen Wert von \bar{c}_ε , d.h. $\lim_{Re \rightarrow \infty} \bar{c}_\varepsilon(Re)$, zu formulieren. In dieses Variationsprinzip geht nur die Form der Randschichten der Variationsprofile ein. Überraschenderweise finden wir bei der numerischen Lösung dieses neuen Variationsprinzips, daß die extremalen Profilfunktionen durch Aufsteilen in unmittelbarer Nähe der Ränder *Randschichten innerhalb der Randsegmente* ausbilden. Somit muß, um die Asymptotik richtig wiederzugeben, die Klasse der Variationsprofile durch einen zusätzlichen Parameter n erweitert werden, der die polynomiale Ordnung der Randsegmente bei $(n - 1)$ -mal stetiger Differenzierbarkeit kennzeichnet. Die dadurch verbesserte obere Schranke des Dissipations-Beiwertes ist in Abbildung 4.6 dargestellt.

Ausgestattet mit diesem Rüstzeug wird in Kapitel 5 (siehe auch Nicodemus, Grossmann & Holthaus 1997d, 1997e) das volle, uneingeschränkte ebene Couette-Problem behandelt. Die Strategie, zuerst das Variationsprinzip an einem verwandten, aber wesentlich einfacheren Problem im Detail zu verstehen, und dann die entwickelte Lösungsmethodik auf das eigentliche, kompliziertere Problem zu übertragen, erweist sich als tragfähig: Alle charakteristischen Merkmale, die wir bei der Analyse der ebenen Scherströmung ohne Freiheitsgrade in spannweiser Richtung gefunden haben, treten in leicht gewandelter Form beim vollen Problem wieder auf.

Auch nach Hinzunahme der dritten Dimension, d.h. der spannweisen Freiheitsgrade, beschränken wir uns weiterhin auf Hintergrund-Flüsse, die sich durch ein nur höhenabhängiges Profil $\phi(z)$ beschreiben lassen. Die periodischen Randbedingungen in x - und y -Richtung führen nun zu zwei unabhängigen Wellenzahlen, k_x und k_y . Folglich ergibt sich für gegebenes ϕ die kritische Reynolds-Zahl $Re_c\{\phi\}$ aus der Minimierung von $R_0\{\phi\}(k_x, k_y)$ in dem nunmehr zweidimensionalen Wellenzahl-Raum. Die Klasse von Test-Profilfunktionen wird durch die drei Parameter n , δ und p charakterisiert, siehe Abbildung 5.3; n ist die polynomiale Ordnung der Randsegmente, δ bestimmt die Ausdehnung dieser Randsegmente, und p ist die Steigung des linearen Verbindungsstückes. An den Nahtstellen sind die Profile $(n-1)$ -mal stetig differenzierbar. Empirisch zeigt sich, daß für jedes Profil die k_x -Komponente der minimierende \mathbf{k} -Vektoren verschwindet (vergleiche hierzu Abbildungen 5.5 und 5.6). Dies spiegelt die Tatsache wider, daß es in Strömungsrichtung keine physikalisch ausgezeichnete Längenskala gibt. Wie in Abbildung 5.7 dargestellt, zeigen die k_y -Komponenten der minimierenden Wellenzahl-Vektoren die gleichen Merkmale wie die k_x -Wellenzahlen im Falle des wohlverstandenen einfacheren Problems (vergleiche Abbildung 3.12): Oberhalb von $Re_B \approx 460$ erscheinen zwei Äste minimierender Wellenzahlen; der untere Ast ($k_{y,1}$) nimmt im asymptotischen Limes den gleichen Wert an, der an der Energiestabilitätsgrenze für das laminare Profil auftritt, während der obere Ast ($k_{y,2}$) im Limes großer Reynolds-Zahlen proportional zu Re skaliert.

Die sich aus der Lösung des Variationsprinzips ergebenden optimierten Profile sind in Abbildung 5.8 dargestellt. Mit Zunahme der Reynolds-Zahl können fünf Bereiche unterschieden werden. (i) Bis $Re = Re_{ES}$ erstreckt sich der laminare Bereich mit seinem linearen Profil. (ii) Im Bereich $Re_{ES} \leq Re \leq Re_1 \approx 160$ deformiert sich das Profil. Die Parameter δ und n bleiben unverändert ($\delta = 0.5$ in Einheiten des Plattenabstandes h , $n = 3$), während die Steigung p von 1 auf annähernd 0 (in Einheiten der relativen Schergeschwindigkeit U der Platten dividiert durch den Plattenabstand h) absinkt. (iii) Im darauffolgenden Bereich $Re_1 \leq Re \leq Re_2 \approx 670$ bilden sich Randschichten aus, d.h. n bleibt weiterhin bei seinem Wert 3, p steigt wieder leicht an, während δ monoton auf seinen minimalen Wert ($\delta \approx 0.14$ in Einheiten des Plattenabstandes h) absinkt. (iv) Danach, im Bereich $Re_2 \leq Re \leq Re_3 \approx 1845$, wächst n dramatisch von 3 auf 34 an. Dieses entspricht einem Aufsteilen der Profile an den Rändern, wodurch neue *innere Randschichten innerhalb der Randsegmente* generiert werden. Als Konsequenz hiervon wächst δ auf seinen maximalen Wert an, so daß die Randsegmente schließlich wieder aneinanderstoßen.

(v) Für $Re \geq Re_3$ folgen die Variationsprofile einfachen Potenzgesetzen: Die Steigung des Profils an den Rändern skaliert proportional zu Re , während die Steigung des Profils in der Mitte umgekehrt proportional mit der Reynolds-Zahl skaliert. Es ist die Gleichschaltung der beiden Minima von $R_0\{\phi\}(0, k_y)$, die sich für dieses Skalenverhalten verantwortlich zeigt. Die beiden für $Re > Re_B$ auftretenden Längenskalen $k_{y,1}^{-1}$ und $k_{y,2}^{-1}$ können im Hinblick auf die aus dem Variationsprinzip resultierenden Profildfunktionen als die Länge des flachen Mittelbereichs des Profils und als die effektive Ausdehnung der (inneren) Randschichten verstanden werden. Somit erklärt sich Bereich (iii) als Übergangsbereich von deformierten Profilen ohne klare Längenskala zu Profilen mit ausgeprägten Randschichten. Auch die asymptotische Koinzidenz der Wellenzahlen des unteren Astes ($k_{y,1}$) mit derjenigen Wellenzahl, die an der Energiestabilitätsgrenze für das laminare Profil auftritt, wird intuitiv klar.

Die sich als Lösung des Variationsprinzips ergebende obere Schranke $\overline{c}_\varepsilon(Re)$ des Dissipations-Beiwertes $c_\varepsilon(Re)$ ist in Abbildung 5.4 dargestellt. Sie weist die schon geläufige Struktur auf. Direkt oberhalb von Re_{ES} steigt sie an, passiert ein Maximum und fällt dann im Bereich (iii) ungefähr proportional zu $Re^{-1/4}$ ab. Im Zusammenhang mit der Bifurkation im k_y -Wellenzahl-Bereich ändert sich dieses Verhalten: Die Schranke durchläuft ein ausgeprägtes Minimum und erreicht schließlich von unten kommend ihren asymptotischen Wert,

$$\lim_{Re \rightarrow \infty} \overline{c}_\varepsilon(Re) \approx 0.01087.$$

Dieser Wert ist entsprechend der Kerswell'schen Vorhersage (Kerswell 1997) mit der Busse'schen Schranke identisch (Busse 1970, 1978), wenn man berücksichtigt, daß letztere mit gewissen Ungenauigkeiten behaftet ist. Somit wurde das Busse'sche Resultat unabhängig bestätigt. Aber der wesentliche Punkt ist, daß in der vorliegenden Arbeit erstmals eine für *alle* Reynolds-Zahlen gültige Schranke von gleicher Qualität berechnet wurde. Diese Schranke zeigt eine nicht-triviale Struktur: Ein ausgeprägtes Minimum gefolgt von einem Re -Bereich zwischen 1000 und 1800, in dem die Krümmung der Schranke ihr Vorzeichen ändert. Diese Änderung des Vorzeichens der Krümmung findet im Bereich (iv) statt und geht mit der *strukturellen Reorganisation* der Randschichten einher. Es ist auffallend, daß dies genau bei solchen Reynolds-Zahlen geschieht, bei denen in typischen experimentell realisierten Scherströmungen der Turbulenz-Einsatz beobachtet wird.

Die Übersichtsgraphik (Abbildung 3.14) zeigt die in dieser Arbeit unter voller Berücksichtigung der spektralen Nebenbedingung berechneten oberen Schranken von c_ε gemeinsam mit der Busse'schen asymptotischen Schranke und früheren Ergebnissen, bei denen die spektrale Nebenbedingung mittels funktionaler Abschätzungen zwar stark vereinfacht, aber auch deutlich übererfüllt wurde. Ebenso in der Abbildung enthalten sind experimentelle Werte des Dissipations-Beiwertes (Reichardt 1959; Lathrop, Fineberg & Swinney 1992). Durch die kor-

rekte Berücksichtigung der spektralen Nebenbedingung gewinnt man gegenüber den früheren Abschätzungen von Doering & Constantin (1992, 1994), Gebhardt *et al.* (1995) und Nicodemus *et al.* (1997a) ungefähr einen Faktor 8. Darüber hinaus waren alle früheren Schranken im wesentlichen strukturlos und damit von beschränkter Aussagekraft. Erst die volle spektrale Nebenbedingung eröffnet die in dieser Arbeit diskutierten Strukturen bei für die Turbulenz-Physik relevanten Reynolds-Zahlen. Zu den experimentellen Daten klafft jedoch eine Lücke von ungefähr einer Größenordnung, und es ist unklar, ob diese Daten asymptotisch überhaupt konstante Werte annehmen. Wäre es möglich, im Rahmen weiter verbesserter Variationsprinzipien einen asymptotischen Abfall, wie er sich in den experimentellen Daten andeutet, im Verhalten der oberen Schranke von c_ε "einzufangen", könnte man definitive Aussagen über mögliche Intermittenz-Korrekturen machen. Für die Formulierung von in dieser Richtung weitertragenden Theorien sind strukturelle Erkenntnisse der Art, wie sie in dieser Arbeit gewonnen wurden, unabdingbar.

2 Improved variational principle for bounds on energy dissipation in turbulent shear flow

2.1 Introduction

While it is not feasible to obtain exact solutions to the equations of motion for turbulent flows, it is possible to derive mathematically rigorous upper bounds on certain quantities characterizing turbulent flow fields, such as the rate of energy dissipation in shear flows or the rate of heat transport in turbulent convection. A detailed theory of upper bounds has been developed by Howard (1972) and Busse (1970, 1978, 1996). The bounds obtained by their method, although still considerably higher than experimentally observed values, have until now resisted any attempt of further improvement (see, e.g. Kerswell & Soward 1996).

Recently a quite different approach has sparked renewed interest in the theory of upper bounds. Instead of starting from the usual Reynolds decomposition, Doering & Constantin (1992, 1994) utilized an idea put forward already by Hopf (1941) and decomposed a turbulent flow field into a stationary “background flow” and a fluctuating component. The background flow should be regarded as an arbitrary mathematical auxiliary field that merely has to carry the boundary conditions of the physical flow field, rather than as a time average of the actual flow. This method turns out to be fairly versatile (see Doering & Constantin 1994, 1996; Constantin & Doering 1995; Marchioro 1994; Gebhardt *et al.* 1995). A given background flow immediately yields an upper bound, provided it satisfies a certain spectral constraint. The best bounds obtainable in this way can therefore be computed from a variational principle for the background flow (Doering & Constantin 1994). A formal connection between this approach and the Howard–Busse theory has been elucidated by Kerswell (1997).

The objective of the present chapter is to point out that the variational principle suggested by Doering and Constantin can still be improved, without introducing additional technical complications. Although our arguments are of a more general kind, we restrict the discussion to the concrete example of energy dissipation in plane Couette flow. In this case the benefits of our formulation of the variational principle are particularly obvious: the laminar flow now becomes an admissible background flow for Reynolds numbers up to the energy stability limit, which is just what should be required on intuitive grounds. This eliminates a shortcoming of the original Doering–Constantin approach. For asymptotically high Reynolds numbers, and employing

one-dimensional background flows only, the improved principle yields upper bounds on the rate of energy dissipation that are systematically by a factor of 27/32 lower than those that can be computed from the original principle.

2.2 Formulation of the variational principle

We consider an incompressible fluid confined between two infinitely extended rigid plates. The lower plate at $z = 0$ is at rest, whereas the upper one at $z = h$ moves with constant velocity U in the positive x -direction. The velocity field $\mathbf{u}(\mathbf{x}, t)$ satisfies the Navier–Stokes equations

$$\partial_t \mathbf{u} + \mathbf{u} \cdot \nabla \mathbf{u} + \nabla p = \nu \Delta \mathbf{u} \quad (2.1)$$

with

$$\nabla \cdot \mathbf{u} = 0, \quad (2.2)$$

where p is the kinematic pressure and ν the kinematic viscosity. We impose no-slip boundary conditions (b.c.) on \mathbf{u} at $z = 0$ and $z = h$,

$$\mathbf{u}(x, y, 0, t) = \mathbf{0}, \quad \mathbf{u}(x, y, h, t) = U \hat{\mathbf{x}} \quad (2.3)$$

($\hat{\mathbf{x}}$ is the unit vector in x -direction), and periodic b.c. on \mathbf{u} and p in x - and y -direction; the periodicity lengths are L_x and L_y . The time-averaged energy dissipation rate per mass is given by

$$\varepsilon_T \equiv \left\langle \left\langle \nu |\nabla \mathbf{u}|^2 \right\rangle \right\rangle_T = \frac{1}{T} \int_0^T dt \left[\frac{\nu}{\Omega} \int_{\Omega} d^3x u_{i|j} u_{i|j} \right]. \quad (2.4)$$

We employ the notation $\langle \cdot \rangle = (1/\Omega) \int_{\Omega} d^3x (\cdot)$ for the volume average and $\langle \cdot \rangle_T = (1/T) \int_0^T dt (\cdot)$ for the time average, $\Omega = L_x L_y h$ denotes the periodicity volume, and $u_{i|j}$ symbolizes $\partial_j u_i(x, y, z, t)$ with $i, j = x, y, z$; summation over repeated indices is implied. The goal is to formulate a variational principle for rigorous upper bounds on the long time limit of ε_T ,

$$\varepsilon \equiv \limsup_{T \rightarrow \infty} \varepsilon_T, \quad (2.5)$$

or on the non-dimensionalized quantity

$$c_\varepsilon(Re) \equiv \frac{\varepsilon}{U^3 h^{-1}}, \quad (2.6)$$

where $Re = Uh/\nu$ is the Reynolds number.

The approach by Doering & Constantin (1992, 1994) rests on a decomposition of the velocity field $\mathbf{u}(\mathbf{x}, t)$ into a *background flow* and *fluctuations*,

$$\mathbf{u}(\mathbf{x}, t) = \mathbf{U}(\mathbf{x}) + \mathbf{v}(\mathbf{x}, t). \quad (2.7)$$

The background flow \mathbf{U} is a stationary and divergence-free vector field satisfying the *physical b.c.*: $\mathbf{U}(x, y, 0) = \mathbf{0}$, $\mathbf{U}(x, y, h) = U\hat{\mathbf{x}}$, and \mathbf{U} is assumed to be periodic in x - and y -direction; otherwise it is completely arbitrary. For the divergence-free fluctuations \mathbf{v} we then have *homogeneous b.c.* for all instants $t \geq 0$, i.e. $\mathbf{v}(x, y, 0, t) = \mathbf{v}(x, y, h, t) = \mathbf{0}$, and \mathbf{v} is periodic in x - and y -direction. With the usual manipulations one arrives at the following equations for \mathbf{u} and \mathbf{v} :

$$\nu \langle |\nabla \mathbf{u}|^2 \rangle = \nu \langle |\nabla \mathbf{U}|^2 \rangle + 2\nu \langle U_{i|j} v_{i|j} \rangle + \nu \langle |\nabla \mathbf{v}|^2 \rangle, \quad (2.8)$$

$$\partial_t \langle \frac{1}{2} \mathbf{v}^2 \rangle + \langle \mathbf{v} \cdot (\mathbf{U} \cdot \nabla \mathbf{U}) \rangle + \langle \mathbf{v} \cdot (\nabla \mathbf{U})_{sym} \cdot \mathbf{v} \rangle = -\nu \langle U_{i|j} v_{i|j} \rangle - \nu \langle |\nabla \mathbf{v}|^2 \rangle, \quad (2.9)$$

where $[(\nabla \mathbf{U})_{sym}]_{ij} \equiv \frac{1}{2} (U_{j|i} + U_{i|j})$. At this point, Doering and Constantin use (2.8) to eliminate the cross background–fluctuation term in (2.9), namely, they form [Eq. (2.8)] + 2 × [Eq. (2.9)]. It is crucial to note that this implies putting a certain fixed weight on the different contributions to the resulting expression for ε_T . In order to avoid such a weighting we introduce a new degree of freedom and consider

$$[\text{Eq. (2.8)}] + a \times [\text{Eq. (2.9)}], \quad a > 1 \quad (2.10)$$

with the *balance parameter* a . Apart from this modification, we now follow closely the spirit of the original Doering–Constantin approach, which can always be recovered by setting $a = 2$. Equation (2.10) leads to the *energy balance equation*

$$\begin{aligned} \varepsilon_T &= \nu \langle |\nabla \mathbf{U}|^2 \rangle - \frac{a}{T} \langle \frac{1}{2} \mathbf{v}(\cdot, T)^2 \rangle + \frac{a}{T} \langle \frac{1}{2} \mathbf{v}(\cdot, 0)^2 \rangle \\ &- a \left\langle \frac{1}{\Omega} \int_{\Omega} d^3x \left[\frac{a-1}{a} \nu |\nabla \mathbf{v}|^2 + \mathbf{v} \cdot (\nabla \mathbf{U})_{sym} \cdot \mathbf{v} + \mathbf{f} \cdot \mathbf{v} \right] \right\rangle_T \end{aligned} \quad (2.11)$$

with

$$\mathbf{f} \equiv \mathbf{U} \cdot \nabla \mathbf{U} - \frac{a-2}{a} \nu \Delta \mathbf{U}, \quad (2.12)$$

which becomes the inequality (see (2.5))

$$\begin{aligned} \varepsilon &\leq \nu \langle |\nabla \mathbf{U}|^2 \rangle \\ &- a \liminf_{T \rightarrow \infty} \left\langle \frac{1}{\Omega} \int_{\Omega} d^3x \left[\frac{a-1}{a} \nu |\nabla \mathbf{v}|^2 + \mathbf{v} \cdot (\nabla \mathbf{U})_{sym} \cdot \mathbf{v} + \mathbf{f} \cdot \mathbf{v} \right] \right\rangle_T. \end{aligned} \quad (2.13)$$

For the evaluation of (2.13) we have to distinguish two different cases.

Case a) \mathbf{f} is a gradient

In this case the term linear in \mathbf{v} on the right hand side of (2.13) vanishes and the resulting bound on the energy dissipation rate is given by

$$\varepsilon \leq \inf_{\mathbf{U}, a > 1} \left\{ \nu \langle |\nabla \mathbf{U}|^2 \rangle \right\}, \quad (2.14)$$

provided \mathbf{U} complies with the following constraints:

- i.) \mathbf{U} is a divergence-free vector field satisfying the physical b.c. and \mathbf{f} is a gradient,
- ii.) the functional

$$H_{U,a}\{\mathbf{w}\} \equiv \frac{1}{\Omega} \int_{\Omega} d^3x \left[\frac{a-1}{a} \nu |\nabla \mathbf{w}|^2 + \mathbf{w} \cdot (\nabla \mathbf{U})_{sym} \cdot \mathbf{w} \right] \quad (2.15)$$

is positive semi-definite, $H_{U,a}\{\mathbf{w}\} \geq 0$, for all stationary divergence-free vector fields \mathbf{w} satisfying the homogeneous b.c.

Condition ii.) is equivalent to the statement that all eigenvalues λ of the hermitian eigenvalue problem

$$\begin{aligned} \lambda \mathbf{V} &= -2 \frac{a-1}{a} \nu \Delta \mathbf{V} + 2 (\nabla \mathbf{U})_{sym} \cdot \mathbf{V} + \nabla P, \\ 0 &= \nabla \cdot \mathbf{V}, \quad \mathbf{V} \text{ satisfies the homogeneous b.c.} \end{aligned} \quad (2.16)$$

are non-negative; P is a Lagrange multiplier for the divergence condition. Following Doering & Constantin (1994), who consider the eigenvalue problem without an adjustable parameter ($a = 2$), we denote the requirement that all eigenvalues of the eigenvalue problem (2.16) be non-negative as

$$\text{spectral constraint: all } \lambda \geq 0. \quad (2.17)$$

Case b) \mathbf{f} is no gradient

In this case we bound the second term on the right hand side of (2.13) by

$$\begin{aligned} & \left\langle \frac{1}{\Omega} \int_{\Omega} d^3x \left[\frac{a-1}{a} \nu |\nabla \mathbf{v}|^2 + \mathbf{v} \cdot (\nabla \mathbf{U})_{sym} \cdot \mathbf{v} + \mathbf{f} \cdot \mathbf{v} \right] \right\rangle_T \\ & \geq \inf_{\mathbf{w}} \left\{ \frac{1}{\Omega} \int_{\Omega} d^3x \left[\frac{a-1}{a} \nu |\nabla \mathbf{w}|^2 + \mathbf{w} \cdot (\nabla \mathbf{U})_{sym} \cdot \mathbf{w} + \mathbf{f} \cdot \mathbf{w} \right] \right\}, \end{aligned} \quad (2.18)$$

where we seek the infimum in the space of all stationary divergence-free vector fields \mathbf{w} satisfying the homogeneous b.c. If \mathbf{V} is the minimizing vector field, it solves the *Euler–Lagrange equations*

$$\begin{aligned} \mathbf{0} &= -2 \frac{a-1}{a} \nu \Delta \mathbf{V} + 2 (\nabla \mathbf{U})_{sym} \cdot \mathbf{V} + \nabla P + \mathbf{f}, \\ 0 &= \nabla \cdot \mathbf{V}, \quad \mathbf{V} \text{ satisfies the homogeneous b.c.}, \end{aligned} \quad (2.19)$$

so that the inequality (2.18) becomes

$$\left\langle \frac{1}{\Omega} \int_{\Omega} d^3x \left[\frac{a-1}{a} \nu |\nabla \mathbf{v}|^2 + \mathbf{v} \cdot (\nabla \mathbf{U})_{sym} \cdot \mathbf{v} + \mathbf{f} \cdot \mathbf{v} \right] \right\rangle_T \geq \frac{1}{2\Omega} \int_{\Omega} d^3x \mathbf{f} \cdot \mathbf{V}. \quad (2.20)$$

The requirement

$$H_{U,a}\{\mathbf{w}\} > 0 \quad \text{for all divergence-free } \mathbf{w} \neq \mathbf{0} \text{ satisfying the homogeneous b.c.} \quad (2.21)$$

guarantees the uniqueness of the solution \mathbf{V} to the Euler–Lagrange equations (2.19) and ensures that this solution indeed minimizes the right hand side of (2.18). The uniqueness can be shown as follows: if there were any other solution $\mathbf{W} \neq \mathbf{V}$, then the difference $\mathbf{W} - \mathbf{V}$ would be a non-vanishing eigensolution to the eigenvalue problem (2.16) with eigenvalue $\lambda = 0$. This contradicts the requirement (2.21), which implies that all eigenvalues of (2.16) are strictly positive. The minimizing character of \mathbf{V} stems from the convexity of the expression in curly brackets on the right hand side of (2.18).

Putting all things together, we see that in this case b) the resulting bound on the energy dissipation rate is given by

$$\varepsilon \leq \inf_{U, a > 1} \left\{ \nu \langle |\nabla \mathbf{U}|^2 \rangle - \frac{1}{2} a \langle \mathbf{V} \cdot (\mathbf{U} \cdot \nabla \mathbf{U}) \rangle + \frac{1}{2} (a-2) \nu \langle \mathbf{V} \cdot \Delta \mathbf{U} \rangle \right\}, \quad (2.22)$$

provided

- i.) \mathbf{U} is a divergence-free vector field satisfying the physical b.c. and \mathbf{f} is no gradient,
- ii.) \mathbf{V} is a solution to the Euler–Lagrange equations (2.19),
- iii.) the functional (2.15) is strictly positive definite, $H_{\mathbf{U},a}\{\mathbf{w}\} > 0$ for all divergence-free vector fields $\mathbf{w} \neq \mathbf{0}$ satisfying the homogeneous b.c. Equivalently, all eigenvalues λ of the eigenvalue problem (2.16) must be positive, so that now we have the

$$\text{spectral constraint: all } \lambda > 0. \quad (2.23)$$

The main technical problem encountered in the original Doering–Constantin approach is to verify their spectral constraint for a given background flow, i.e. to show that all eigenvalues of the eigenvalue problem (2.16) with $a = 2$ are non-negative (case a) or positive (case b). In this respect our formulation generates no additional complications because our constraining eigenvalue problem is formally identical with the original one, the only difference being that the kinematic viscosity is rescaled by a factor $2(a-1)/a$. Since $-\Delta$ is a positive definite unbounded operator, the spectral constraint enforces the positivity of this scaling factor, as anticipated in (2.10) by the condition $a > 1$.

It should be noted that our formulation differs from the original one in two major points. Firstly, if $\Delta\mathbf{U}$ is no gradient then the minimizing field \mathbf{V} must be determined by solving the Euler–Lagrange equations (2.19) even if $\mathbf{U} \cdot \nabla\mathbf{U}$ is a gradient, since the contribution to \mathbf{f} that is proportional to $\Delta\mathbf{U}$ vanishes only if $a = 2$, see (2.12). Secondly, our variational principle concerns not only the background flow \mathbf{U} but also the balance parameter a . We will see that in the case of one-dimensional background flows both issues can be dealt with easily; solving the Euler–Lagrange equations and minimizing over a will be independent from the intricate problem of verifying the spectral constraint. Hence, the additional freedom gained by the balance parameter a entails no additional difficulties, but will result in an improved bound on ε .

2.3 Plane Couette flow with one-dimensional background flows

To become more specific we restrict the following discussion to one-dimensional background flows, i.e. to flows which can be described by a *profile function* ϕ ,

$$\mathbf{U} = U\phi(\zeta)\hat{\mathbf{x}}; \quad \phi(0) = 0, \quad \phi(1) = 1, \quad (2.24)$$

depending on the dimensionless variable $\zeta \equiv z/h$. Clearly, such a \mathbf{U} is a divergence-free vector field satisfying the physical b.c. Additionally we impose $\phi(\zeta) = 1 - \phi(1 - \zeta)$, so that the profile is adapted to the symmetry of the physical problem.

a) Laminar profile, $\phi(\zeta) = \zeta$

In this case \mathbf{U} is the laminar solution to the equations of motion (2.1) and (2.2), and we have $\mathbf{f} = \mathbf{0}$. Hence, case a) of our variational principle applies. Provided all eigenvalues of the eigenvalue problem (2.16) are non-negative, the estimate (2.14) yields

$$\varepsilon = \nu \frac{U^2}{h^2} \quad \text{or} \quad c_\varepsilon(Re) = Re^{-1}, \quad (2.25)$$

respectively. We have strict equalities here since upper and lower bounds on the long time limit of ε_T coincide, as long as the laminar profile fulfills the spectral constraint (Doering & Constantin 1994). We are thus led to the following question: what is the maximal Reynolds number Re (or inverse kinematic viscosity ν^{-1}) up to which the laminar profile is admitted as a valid test profile for the variational principle?

Since the viscosity enters into the eigenvalue problem (2.16) only in rescaled form, we can tune the Reynolds number by suitably adjusting the value of a . In order to find the maximal “critical” Reynolds number for the laminar profile we have to set $a = \infty$, so that the scaling factor $2(a-1)/a$ of the viscosity takes on the highest value possible, namely 2. The eigenvalue problem then becomes

$$\begin{aligned} \lambda \mathbf{V} &= -2\nu \Delta \mathbf{V} + \frac{U}{h} \begin{pmatrix} 0 & 0 & 1 \\ 0 & 0 & 0 \\ 1 & 0 & 0 \end{pmatrix} \cdot \mathbf{V} + \nabla P, \\ 0 &= \nabla \cdot \mathbf{V}, \quad \mathbf{V} \text{ satisfies the homogeneous b.c.} \end{aligned} \quad (2.26)$$

This is exactly the eigenvalue problem appearing in energy stability theory for the plane Couette flow (see e.g. Joseph 1976; Drazin & Reid 1981). Hence, the laminar profile is an admissible test profile up to the Reynolds number Re_{ES} characterizing the energy stability limit (Joseph 1976; Drazin & Reid 1981),

$$Re_{ES} \approx 2\sqrt{1707.76} \approx 82.65, \quad (2.27)$$

and consequently (2.25) is valid for all $Re \leq Re_{ES}$.

In the original Doering–Constantin approach ($a = 2$) one had to discard the laminar profile already for Reynolds numbers $Re > \frac{1}{2}Re_{ES}$, which necessarily led to non-optimal upper bounds on c_ε for Reynolds numbers $\frac{1}{2}Re_{ES} < Re \leq Re_{ES}$. The introduction of the balance parameter cures this obvious shortcoming and guarantees that c_ε as obtained from the variational principle has the known $1/Re$ -behaviour up to $Re = Re_{ES}$.

b) Non-laminar profile, $\phi(\zeta) \neq \zeta$

In this case we have

$$\mathbf{f} = -\frac{a-2}{a} \nu \frac{U}{h^2} \phi''(\zeta) \hat{\mathbf{x}} \quad \text{with} \quad \phi''(\zeta) \neq 0. \quad (2.28)$$

The boundary conditions (2.24) together with the symmetry condition ensure that \mathbf{f} cannot be a gradient if $a \neq 2$, so that now we have to resort to case b) of our variational principle. Because of the special form that the inhomogeneous term \mathbf{f} acquires for non-laminar profiles, one can find an analytical solution to the Euler–Lagrange equations (2.19):

$$\mathbf{V} = \frac{1}{2} \frac{a-2}{a-1} U [\zeta - \phi(\zeta)] \hat{\mathbf{x}}, \quad (2.29)$$

$$P = P_0 + \frac{1}{2} \frac{a-2}{a-1} U^2 \left[\frac{1}{2} \phi(\zeta)^2 - \int_0^\zeta d\xi \xi \phi'(\xi) \right]. \quad (2.30)$$

Note that \mathbf{V} vanishes if $a = 2$, so that we do not need to distinguish between the cases $a \neq 2$ and $a = 2$. Moreover, the right hand side of (2.29) is proportional to the difference between $\phi(\zeta)$ and the laminar profile ζ , which leads us back to the laminar case a) in the limit $\phi(\zeta) \rightarrow \zeta$. Provided all eigenvalues of (2.16) are positive, the estimate (2.22) yields

$$\varepsilon \leq \inf_{\phi, a > 1} \left\{ \left[1 + \frac{a^2}{4(a-1)} D\{\phi\} \right] \nu \frac{U^2}{h^2} \right\}; \quad (2.31)$$

the inequality for c_ε reads

$$c_\varepsilon \leq \inf_{\phi, a > 1} \left\{ \left[1 + \frac{a^2}{4(a-1)} D\{\phi\} \right] Re^{-1} \right\}. \quad (2.32)$$

Here we have employed the abbreviation $D\{\phi\}$ for the functional

$$D\{\phi\} \equiv \int_0^1 d\zeta [\phi'(\zeta)]^2 - 1. \quad (2.33)$$

This functional is strictly positive for $\phi(\zeta) \neq \zeta$, which means that for each non-laminar profile and each $a > 1$ the factor $1 + \left(\frac{1}{4} a^2 / (a-1)\right) D\{\phi\}$ appearing in (2.31) and (2.32) exceeds one. Therefore, each non-laminar profile produces a bound that is strictly higher than the laminar bound (2.25).

In a manner analogous to the procedure for the laminar profile one has to investigate on the basis of the eigenvalue problem (2.16) up to which Reynolds number a given profile ϕ is admissible as a test profile. Because of the positive-definiteness of $-\Delta$, the spectrum of the hermitian operator defined by the right hand side of (2.16) is lowered when the rescaled kinematic viscosity is decreased. Thus, for a given ϕ we define the *critical Reynolds number* $R_c\{\phi\}$ as that Reynolds number where the lowest eigenvalue λ of (2.16) with fixed balance parameter $a = \infty$ (i.e. $2(a-1)/a = 2$ is maximal) passes through zero. For $Re \geq R_c\{\phi\}$ one has to discard ϕ as a test profile for the variation. In addition, if $a > 1$ is finite, one finds the constraint

$$Re < \frac{a-1}{a} R_c\{\phi\}. \quad (2.34)$$

The factor $a^2/(a-1)$ in (2.31) and (2.32) has a local minimum for $a = 2$ and increases monotonically with a for $a > 2$. A given ϕ thus produces the following upper bound on c_ε :

$$c_\varepsilon \leq \left[1 + \frac{a_{opt}^2}{4(a_{opt}-1)} D\{\phi\} \right] Re^{-1} \quad \text{for } 0 \leq Re < R_c\{\phi\} \quad (2.35)$$

with

$$a_{opt} = \begin{cases} 2 & \text{for } 0 \leq Re < \frac{1}{2}R_c\{\phi\} \\ \frac{R_c\{\phi\}}{R_c\{\phi\}-Re} & \text{for } \frac{1}{2}R_c\{\phi\} \leq Re < R_c\{\phi\} \end{cases}; \quad (2.36)$$

hence

$$c_\varepsilon \leq \begin{cases} [1 + D\{\phi\}] Re^{-1} & \text{for } 0 \leq Re < \frac{1}{2}R_c\{\phi\} \\ \left[1 + \frac{D\{\phi\}R_c\{\phi\}^2}{4(R_c\{\phi\}-Re)Re} \right] Re^{-1} & \text{for } \frac{1}{2}R_c\{\phi\} \leq Re < R_c\{\phi\} \end{cases}. \quad (2.37)$$

In this way we have accomplished the optimization of the balance parameter and are left with the task of varying the profile function. But it is possible to deduce some general statements even *without* solving the variational principle for ϕ . To this end, we denote the expression on the right hand side of (2.37) as $\bar{c}_\varepsilon(Re)$. This is a continuous function of the Reynolds number, and even continuously differentiable at $Re = \frac{1}{2}R_c\{\phi\}$. For every given profile, $\bar{c}_\varepsilon(Re)$ has exactly one local minimum in the whole interval $0 \leq Re < R_c\{\phi\}$; this minimum appears in the upper half interval $\frac{1}{2}R_c\{\phi\} \leq Re < R_c\{\phi\}$. Because the variational principle tests *all* profile functions ϕ satisfying the required conditions, the minimum point determined by a particular ϕ is the only point that this profile could possibly contribute to the resulting upper bound on $c_\varepsilon(Re)$. Thus,

each ϕ leads to a point in the (Re, c_ε) -plane,

$$\phi \mapsto (Re_{min}\{\phi\}, \overline{c_\varepsilon}(Re_{min}\{\phi\})). \quad (2.38)$$

The Reynolds number $Re_{min}\{\phi\}$ of the minimum point can be expressed as

$$Re_{min}\{\phi\} = X_0\{\phi\} R_c\{\phi\}, \quad (2.39)$$

where $X_0\{\phi\}$ is the unique (real) zero X_0 with $\frac{1}{2} \leq X_0 < 1$ of the cubic polynomial

$$x^3 - 2x^2 + \left(1 - \frac{3}{4}D\{\phi\}\right)x + \frac{1}{2}D\{\phi\} = 0. \quad (2.40)$$

This follows directly by minimizing $\overline{c_\varepsilon}(Re)$ with respect to Re . Although an analytical expression for the desired zero of (2.40) is available for all $D\{\phi\} > 0$, we will discuss only the two limiting cases. In the *laminar limit* $\phi(\zeta) \rightarrow \zeta$ the functional $D\{\phi\}$ vanishes and the zero $X_0\{\phi\}$ tends to 1. Inserting $Re_{min}\{\phi\}$ into (2.36) shows that a_{opt} tends to infinity in this limit,

$$\lim_{Re \searrow Re_{ES}} a_{opt} = \infty. \quad (2.41)$$

Therefore, the optimal bounds on c_ε resulting from the variational principle will be continuous at the energy stability limit. On the other hand, for sufficiently high Reynolds numbers the spectral constraint (2.23) singles out those profile functions as admissible for the variational principle that have large slopes within thin boundary layers and remain almost constant in the interior (Doering & Constantin 1994). Hence the functional $D\{\phi\}$ tends to infinity in the *asymptotic limit* $Re \rightarrow \infty$, which implies that the zero $X_0\{\phi\}$ tends to $2/3$ and a_{opt} approaches its asymptotic value 3,

$$\lim_{Re \rightarrow \infty} a_{opt} = 3. \quad (2.42)$$

The optimal value of the balance parameter a , considered as a function of the Reynolds number, is decreasing from infinity at the energy stability limit Re_{ES} to its asymptotic limit $a_\infty = 3$ and never reaches the value $a = 2$ that has tacitly been taken for granted before.

In the original approach (Doering & Constantin 1994) a given profile ϕ yields an upper bound on c_ε in a similar way, but the range of Reynolds numbers within which this profile is admissible is only half as large as in our case. Since, as remarked before, the factor $a^2/(a-1)$ appearing

in (2.32) has a minimum for $a = 2$, in the common interval this bound agrees with ours:

$$c_\varepsilon \leq \overline{c_\varepsilon}(Re) \quad \text{for} \quad 0 \leq Re \leq \frac{1}{2}R_c\{\phi\}. \quad (2.43)$$

Here the minimizing point is $(R_c\{\phi\}/2, \overline{c_\varepsilon}(R_c\{\phi\}/2))$, which has to be compared with (2.38). Therefore, in our formulation a given profile function ϕ leads to a *lowered* bound on c_ε at a *higher* Reynolds number Re . The improvement due to the balance parameter a relies on the fact that each ϕ becomes admissible within an enlarged Re -interval. Note that in both cases exactly the same eigenvalue problem must be solved to check the spectral constraint.

Under the assumption that in both formulations the upper bounds on c_ε are approaching constant values in the asymptotic limit $Re \rightarrow \infty$, dubbed $\overline{c_{\varepsilon\infty}}$ and $\overline{c_{\varepsilon\infty}^{DC}}$, respectively, we can calculate the relative factor

$$g_\infty \equiv \frac{\overline{c_{\varepsilon\infty}}}{\overline{c_{\varepsilon\infty}^{DC}}} = \lim_{Re \rightarrow \infty} \frac{\overline{c_\varepsilon}(X_0\{\phi\} R_c\{\phi\})}{\overline{c_\varepsilon}(R_c\{\phi\}/2)} = \frac{27}{32}. \quad (2.44)$$

Considering the same class of one-dimensional background flows, our formulation yields asymptotic upper bounds on the rate of energy dissipation that are systematically lowered by a factor of 27/32 compared to those that can be computed from the original Doering–Constantin approach.

2.4 Illustration

In this section we wish to illustrate the general statements derived in the preceding section. Our aim is not to calculate the best bounds that the improved variational principle has to offer, but rather to elucidate the new aspects in a simple way. Instead of verifying the spectral constraint for a given ϕ on the basis of the eigenvalue problem (2.16), one can check the positivity of the functional $H_{U,a}\{\mathbf{w}\}$,

$$H_{U,a}\{\mathbf{w}\} = \frac{1}{\Omega} \int_{\Omega} d^3x \left[\frac{a-1}{a} \nu |\nabla \mathbf{w}|^2 + \frac{U}{h} \phi' w_x w_z \right], \quad (2.45)$$

by means of the inequality

$$\left| \frac{1}{\Omega} \int_{\Omega} d^3x \frac{U}{h} \phi' w_x w_z \right| \leq \frac{\langle |\nabla \mathbf{w}|^2 \rangle}{2\sqrt{2}} \int_0^{h/2} dz z \frac{U}{h} |\phi'|. \quad (2.46)$$

This estimate can be shown by repeatedly using Schwarz' inequality and utilizing the symmetry property of the profile function (Gebhardt *et al.* 1995; see also Doering & Constantin 1992,

1994). Thus,

$$H_{U,a}\{\mathbf{w}\} \geq \left[\frac{a-1}{a} \nu - \frac{Uh}{2\sqrt{2}} \int_0^{1/2} d\zeta \zeta |\phi'| \right] \langle |\nabla \mathbf{w}|^2 \rangle. \quad (2.47)$$

If the profile function $\phi(\zeta)$ satisfies the condition

$$\int_0^{1/2} d\zeta \zeta |\phi'(\zeta)| \leq 2\sqrt{2} \frac{a-1}{a} Re^{-1} \quad \left(\text{or} \quad \int_0^{1/2} d\zeta \zeta |\phi'(\zeta)| < 2\sqrt{2} \frac{a-1}{a} Re^{-1} \right), \quad (2.48)$$

then the non-negativity (or the positivity) of the functional $H_{U,a}\{\mathbf{w}\}$ is guaranteed. It should be realized that (2.48) is a sufficient but not a necessary condition; it is more restrictive than the spectral constraint. In addition to the b.c. (2.24) and the symmetry requirement we assume $\phi'(\zeta) \geq 0$, so that the modulus signs $||$ in (2.48) can be skipped.

After the replacement of the variational principle's spectral constraint (condition ii.) in case a) and condition iii.) in case b), respectively) by the *over-restrictive profile constraint* (2.48), a certain ϕ can, in general, no longer be admitted as a test profile for Reynolds numbers up to $R_c\{\phi\}$ as defined in the preceding section. Rather, (2.48) leads to the border

$$R_c^S\{\phi\} \equiv \frac{2\sqrt{2}}{\int_0^{1/2} d\zeta \zeta \phi'(\zeta)}. \quad (2.49)$$

For example, the laminar profile $\phi(\zeta) = \zeta$ yields

$$R_c^S\{\zeta\} = 16\sqrt{2} \approx 22.63, \quad (2.50)$$

which has to be contrasted to (2.27), i.e. $R_c\{\zeta\} = Re_{ES} \approx 82.65$. Thus $R_c^S\{\zeta\}$ is by about a factor 4 smaller than $R_c\{\zeta\}$. Nevertheless, it is instructive to consider the variational principle with the stronger constraint (2.48) since then even the variation of the profile ϕ can be done analytically. For finite $a > 1$ we now have the constraint

$$Re < \frac{a-1}{a} R_c^S\{\phi\} \quad (2.51)$$

instead of (2.34), which is exactly (2.48).

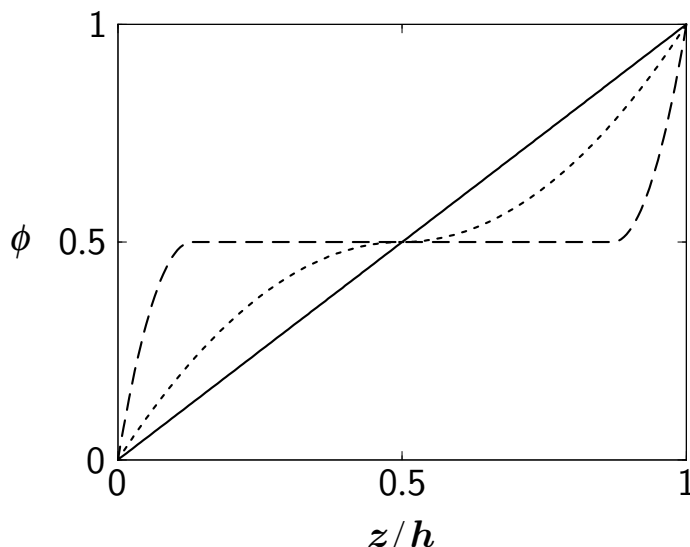


Figure 2.1: Background flow profiles resulting from the variational principle with the over-restrictive profile constraint (2.48). Solid line: $0 \leq Re \leq 16\sqrt{2}$; short dashes: $Re = 20\sqrt{2}$; long dashes: $Re = 64\sqrt{2}$.

Without going into the cumbersome technical details (see also Gebhardt *et al.* (1995) for comparison) we summarize our results. We have to distinguish three Re -ranges,

$$\begin{aligned}
 \text{(I)} \quad & 0 \leq Re \leq 16\sqrt{2}, \\
 \text{(II)} \quad & 16\sqrt{2} < Re \leq 20\sqrt{2}, \\
 \text{(III)} \quad & 20\sqrt{2} < Re < \infty.
 \end{aligned} \tag{2.52}$$

In these ranges the minimizing profile function behaves as sketched in figure 2.1: in (I) ϕ is equal to the laminar profile, $\phi(\zeta) = \zeta$. In (II) the profile develops parabolic boundary layers which reach the middle of the domain Ω (i.e. $\zeta = \frac{1}{2}$), while the slope at $\zeta = \frac{1}{2}$ decreases from one to zero with increasing Re . When Re is increased beyond $20\sqrt{2}$, the thickness δ of these parabolic boundary layers is getting smaller and smaller; in the interior ϕ remains constant, $\phi(\zeta) = \frac{1}{2}$ for $\delta \leq \zeta \leq 1 - \delta$. Asymptotically, δ vanishes as $\sim 1/Re$. The analytic expression for δ in (III) reads

$$\delta = \frac{4\sqrt{2}}{Re} \frac{3\sqrt{Re - 2\sqrt{2}} + \sqrt{Re - 18\sqrt{2}}}{\sqrt{Re - 2\sqrt{2}} + \sqrt{Re - 18\sqrt{2}}} \xrightarrow{Re \rightarrow \infty} \frac{8\sqrt{2}}{Re}. \tag{2.53}$$

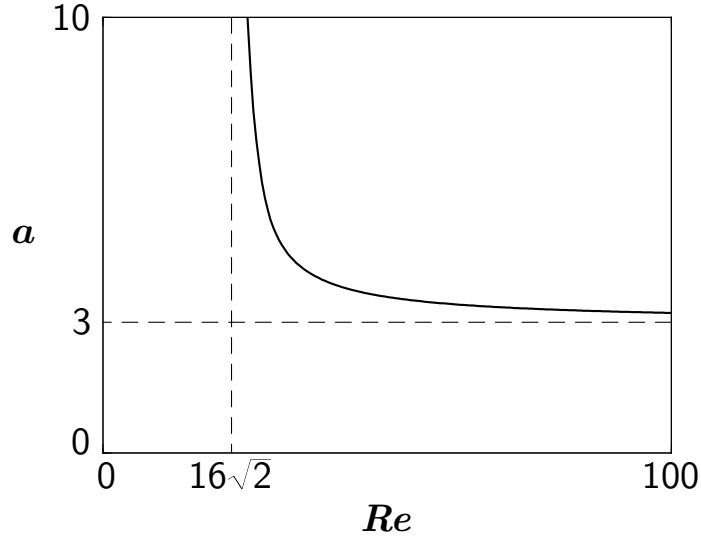


Figure 2.2: Balance parameter a resulting from the variational principle with the over-restrictive profile constraint (2.48).

Correspondingly, the functional $D\{\phi\}$ defined by (2.33) diverges for $Re \rightarrow \infty$, as anticipated in §3.

The minimizing balance parameter a turns out to be

$$a = \begin{cases} \infty & \text{(i.e. } 2 \frac{a-1}{a} = 2) & \text{(I)} \\ 2 + \frac{16\sqrt{2}}{Re-16\sqrt{2}} & \text{(II)} \\ \frac{3}{2} \left(1 + \sqrt{\frac{Re-2\sqrt{2}}{Re-18\sqrt{2}}} \right) & \text{(III)} \end{cases} . \quad (2.54)$$

For $Re > 16\sqrt{2}$ this parameter decreases monotonically from ∞ to its asymptotic value $a_\infty = 3$, as depicted in figure 2.2.

Finally, the resulting bounds on c_ε are given by

$$\frac{1}{Re} \leq c_\varepsilon(Re) \leq \begin{cases} \frac{1}{Re} & \text{(I)} \\ \left(1 - \frac{12\sqrt{2}}{Re} \right) \frac{4}{Re} & \text{(II)} \\ \frac{3}{16\sqrt{2}} \frac{\sqrt{Re-2\sqrt{2}} + \sqrt{Re-18\sqrt{2}}}{3\sqrt{Re-2\sqrt{2}} + \sqrt{Re-18\sqrt{2}}} + \frac{1}{\left(3\sqrt{Re-2\sqrt{2}} + \sqrt{Re-18\sqrt{2}} \right)^2} & \text{(III)} \end{cases} . \quad (2.55)$$

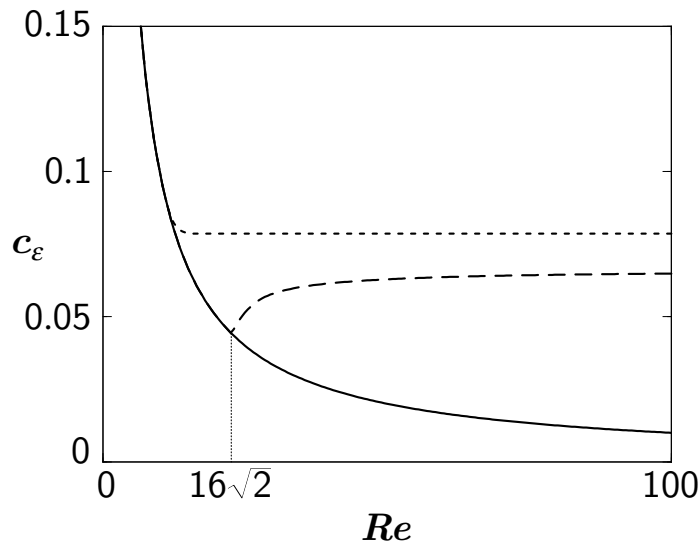


Figure 2.3: Bounds on the dimensionless energy dissipation rate $c_\varepsilon(Re)$ derived from the variational principle with the over-restrictive profile constraint (2.48). Solid line: lower bound Re^{-1} ; long dashes: upper bound with optimized parameter a (see inequality (2.55)); short dashes: upper bound obtained in Gebhardt *et al.* (1995) for $a = 2$ fixed (see inequality (2.58)).

Note that the upper bound is continuous but not continuously differentiable at $Re = 16\sqrt{2}$, see figure 2.3. The limit $Re \rightarrow \infty$ yields

$$c_\varepsilon(\infty) \leq \lim_{Re \rightarrow \infty} \overline{c}_\varepsilon(Re) = \frac{3}{32\sqrt{2}}. \quad (2.56)$$

As before, we denote the upper bound on $c_\varepsilon(Re)$ by $\overline{c}_\varepsilon(Re)$.

These results have to be compared with those derived in Gebhardt *et al.* (1995), where the over-restrictive profile constraint (2.48) was used to calculate bounds on c_ε analytically within the framework established by Doering and Constantin ($a = 2$ fixed). The analogous three Re -ranges found there are

$$\begin{aligned} \text{(I')} \quad & 0 \leq Re \leq 8\sqrt{2}, \\ \text{(II')} \quad & 8\sqrt{2} < Re \leq 12\sqrt{2}, \\ \text{(III')} \quad & 12\sqrt{2} < Re < \infty; \end{aligned} \quad (2.57)$$

in particular, the first range (I') is only half as wide as in our case. The corresponding bounds on c_ε are given by

$$\frac{1}{Re} \leq c_\varepsilon(Re) \leq \begin{cases} \frac{1}{Re} & \text{(I')} \\ \left(1 - \frac{12\sqrt{2}}{Re} + \frac{96}{Re^2}\right) \frac{4}{Re} & \text{(II')} \\ \frac{1}{9\sqrt{2}} & \text{(III')} \end{cases} . \quad (2.58)$$

The improvement due to the parameter a is measured by the ratio of the right hand side of (2.55) and the right hand side of (2.58),

$$\tilde{g}(Re) \equiv \frac{\overline{c_\varepsilon}(Re)}{\overline{c_\varepsilon}^{DC}(Re)}. \quad (2.59)$$

This ratio has a minimum at $Re = 16\sqrt{2}$,

$$\tilde{g}(16\sqrt{2}) = \frac{9\sqrt{2}}{16\sqrt{2}} = \frac{9}{16} \approx 0.56, \quad (2.60)$$

and increases monotonically with increasing Re to its asymptotic value $27/32$,

$$\lim_{Re \rightarrow \infty} \tilde{g}(Re) = \frac{3 \cdot 9\sqrt{2}}{32\sqrt{2}} = \frac{27}{32} \approx 0.84. \quad (2.61)$$

A graphical comparison of the bounds (2.55) and (2.58) is shown in figure 2.3.

2.5 Conclusion: background flow and balance parameter belong together

In this chapter we have been concerned with an improved *formulation* of the Doering–Constantin variational principle for bounds on turbulent energy dissipation, rather than with its *solution*. The necessity of devoting the utmost care to an optimal formulation is obvious: what has been lost by a non-optimal formulation of a variational principle can not be regained by even the most sophisticated techniques for solving it.

The feasibility of improving the background flow method rests on two key observations. The first of these is that if one refrains from what appears to be straightforward, namely, if one does *not* eliminate the unwanted cross background–fluctuation term from (2.9) but rather keeps this term with a certain weight quantified by the balance parameter a , one gains a new freedom that can be exploited to improve the bounds. The second observation is that the required solution to the Euler–Lagrange equations (2.19) can easily be written down analytically if one

restricts oneself to background flows which only have a height-dependent profile but no spanwise structure. Then the technical difficulties encountered in our formulation are the same as those of the original approach — in both cases one has to solve the same eigenvalue problem in order to check whether a given profile is an admissible candidate for the computation of the bound, albeit in our case the kinematic viscosity is rescaled —, but the improved formulation leads to systematically lowered bounds.

Finally, we wish to stress that the usefulness of introducing the balance parameter is by no means restricted to the case of plane Couette flow. It should be obvious by now that the arguments employed in §§ 2 and 3 can easily be adapted to other problems. When computing upper bounds on *any* property of a turbulent flow that is amenable to the background flow method, background flow and balance parameter should henceforth be regarded as belonging together.

3 Constructive approach to the variational principle

3.1 Introduction

Mathematically rigorous results are scarce in the theory of turbulence. One of the few approaches which aim at rigorosity arises from the attempt to derive inequalities for determining bounds on quantities that characterize turbulent flows. This approach had reached a certain state of maturity already 25 years ago (see Howard 1972); perhaps the most notable among the earlier contributions is the Optimum Theory developed by Busse (1970, 1978, 1996). For instance, this theory still gives for asymptotically high Reynolds numbers the best rigorous upper bound on the rate of energy dissipation in turbulent Couette flow that could be calculated so far.

The recent formulation by Doering and Constantin of a variational principle for bounding the energy dissipation rate in turbulent shear flow (Doering & Constantin 1994), channel flow (Constantin & Doering 1995), and convection (Doering & Constantin 1996) has therefore met with considerable interest. What is the actual scope of this new principle? Is it just a non-obvious reformulation of previous theories, or can one obtain further deep insights from it? These questions have already found a partial answer in the work of Kerswell (1997), who showed that the Doering–Constantin principle, if improved by a further variational parameter (see chapter 2 of this thesis), yields precisely the same asymptotic bound on the energy dissipation rate for the plane Couette flow, or the rate of heat transport in Rayleigh–Bénard convection, as the Optimum Theory. But still, Kerswell had to rely on certain assumptions implicit in the Optimum Theory, and rigorous bounds for finite Reynolds numbers remained out of reach. In order to fully explore the possibilities opened up by the Doering–Constantin principle, this principle has to be attacked head-on.

This is what we will do in the present chapter. Namely, we develop a numerical scheme that allows us to exploit the variational principle in the entire range from “low” to “high” Reynolds numbers, where the resulting bound shows a distinct asymptotic scaling behaviour. In addition to extracting the best possible numbers from the variational principle, we also analyse the mathematical structures behind those numbers.

In order to reach these goals we resort to a compromise. Although we will state results pertaining to the full unrestricted plane Couette flow, we will illustrate our techniques with the help of a simplified example, namely the Couette flow without spanwise degrees of freedom. This model

problem exhibits virtually all salient features also encountered in the analysis of the unrestricted Couette problem, while allowing us to keep the technicalities within reasonable limits. On the other hand, this restriction makes possible a fairly detailed discussion of the crucial issues, which will then provide the starting points for the analytical theory developed in the next chapter.

The present chapter is concerned with the numerical aspects of the variational principle. In §2 we will state the principle for obtaining upper bounds on energy dissipation in plane Couette flow, and relate this principle to the works by Busse (1970, 1978, 1996) and Kerswell (1997). The main technical difficulty in evaluating the principle is caused by its spectral constraint, which seems to have prevented previous numerical work (Doering & Hyman 1997) from reaching the asymptotic regime. In §3 we show how to bring this spectral constraint into a form that can be dealt with efficiently even at asymptotically high Reynolds numbers, while §4 describes the optimization procedure for a specific class of test functions. We then state in §5 some characteristic phenomena and problems, before presenting our findings in §6. The final §7 offers a brief discussion, together with an overview of several results obtained up to now.

The aim of the present numerically oriented chapter is twofold. On the one hand, we wish to provide a detailed example that can serve as a definite guideline when applying the extended Doering–Constantin principle to different, more complicated flows; on the other hand, we want to acquire some knowledge about how the principle works, and to collect clues for the analytical approach. The most important observation made here, namely a bifurcation of the minimizing wavenumber that determines the optimal upper bound on the dissipation rate, will be depicted in figure 3.12. In the following chapter of this thesis we will take up loose ends, and develop an analytical asymptotic theory of optimal upper bounds. This theory will be capable of explaining all features found in the numerical investigation.

3.2 Variational principle for plane Couette flow

We consider the standard plane Couette geometry: an incompressible fluid with kinematic viscosity ν is confined between two infinitely extended rigid plates. The lower plate is at rest and coincides with the plane $z = 0$ of a Cartesian coordinate system, whereas the upper one at $z = h$ moves with constant velocity U in the positive x -direction. The dynamics of the fluid's velocity field $\mathbf{u}(\mathbf{x}, t)$ are governed by the equations

$$\partial_t \mathbf{u} + \mathbf{u} \cdot \nabla \mathbf{u} + \nabla p = \nu \Delta \mathbf{u} \quad (\text{Navier–Stokes equations}), \quad (3.1)$$

$$\nabla \cdot \mathbf{u} = 0 \quad (\text{incompressibility}), \quad (3.2)$$

$$\mathbf{u}(x, y, 0, t) = \mathbf{0}, \quad \mathbf{u}(x, y, h, t) = U \hat{\mathbf{x}} \quad (\text{no-slip boundary conditions}); \quad (3.3)$$

$\hat{\mathbf{x}}$ denotes the unit vector in x -direction. Periodic boundary conditions (b.c.) in x - and y -direction are imposed on \mathbf{u} and on the kinematic pressure p ; the periodicity lengths are L_x and

L_y . Denoting the periodicity volume as $\Omega = L_x L_y h$, the time-averaged rate of energy (per mass) dissipated by the fluid is given by

$$\varepsilon_T \equiv \frac{1}{T} \int_0^T dt \left\{ \frac{\nu}{\Omega} \int_{\Omega} d^3x \left[\sum_{i,j=x,y,z} (\partial_j u_i)^2 \right] \right\}. \quad (3.4)$$

The objective of the background flow method is to calculate mathematically rigorous bounds on the long-time limit ε of ε_T ,

$$\varepsilon \equiv \lim_{T \rightarrow \infty} \varepsilon_T, \quad (3.5)$$

or on the non-dimensionalized dissipation rate

$$c_\varepsilon(Re) \equiv \frac{\varepsilon}{U^3 h^{-1}}, \quad (3.6)$$

where $Re = Uh/\nu$ is the Reynolds number.

Energy stability theory, applied to the plane Couette flow, asserts (see Joseph 1976; Drazin & Reid 1981) that any initial deviation from the laminar solution $\mathbf{u}(\mathbf{x}, t) = (Uz/h) \hat{\mathbf{x}}$ decays at least exponentially in time as long as the Reynolds number remains less than the energy stability limit $Re_{ES} \approx 82.65$. Thus,

$$c_\varepsilon(Re) = Re^{-1} \quad \text{for } Re < Re_{ES}. \quad (3.7)$$

In addition, the laminar flow yields a rigorous lower bound $\underline{c}_\varepsilon$ for all Re , namely $c_\varepsilon(Re) \geq \underline{c}_\varepsilon(Re) \equiv Re^{-1}$ (Doering & Constantin 1994). Hence, the actual task is to formulate a theory for calculating *upper bounds* on c_ε for $Re \geq Re_{ES}$.

This task was tackled by Busse in the framework of his Optimum Theory (Busse 1970, 1978, 1996), which is based on a decomposition of the velocity field into a z -dependent plane-averaged flow and the accompanying fluctuations. This decomposition leads in a straightforward manner to a nonlinear Euler–Lagrange problem, for which Busse, using an asymptotic solution technique, found the so-called multi- α solutions. In this way he was able to derive an asymptotic upper bound on c_ε ,

$$\lim_{Re \rightarrow \infty} c_\varepsilon(Re) \lesssim 0.010. \quad (3.8)$$

The right hand side of (3.8) does not depend on the Reynolds number, so that the Optimum Theory is in accordance with the classical scaling behaviour (Kolmogorov 1941; Obukhov 1941;

von Weizsäcker 1948; Heisenberg 1948; Onsager 1945; for a discussion of the connection between $c_\varepsilon(Re)$ and intermittency corrections see Grossmann 1995). As a consequence of the various approximations involved in the multi- α solutions, the numerical value of the constant is afflicted with some uncertainty¹.

The approach recently pioneered by Doering & Constantin (1992, 1994) rests on a quite different decomposition of the velocity field. Instead of considering some kind of averaged mean flow, these authors revive an idea already put forward by Hopf (1941) and introduce an auxiliary stationary and divergence-free flow field $\mathbf{U}(\mathbf{x})$ that has to carry the boundary conditions of the physical flow: $\mathbf{U}(x, y, 0) = \mathbf{0}$, $\mathbf{U}(x, y, h) = U\hat{\mathbf{x}}$, and $\mathbf{U}(\mathbf{x})$ is assumed to be periodic in x - and y -direction. Otherwise this auxiliary field, dubbed the *background flow*, can be chosen arbitrarily. The decomposition of the flow field then reads

$$\mathbf{u}(\mathbf{x}, t) = \mathbf{U}(\mathbf{x}) + \mathbf{v}(\mathbf{x}, t), \quad (3.9)$$

where the divergence-free deviation $\mathbf{v}(\mathbf{x}, t)$ from the background flow satisfies homogeneous b.c. for all instants $t \geq 0$, i.e. $\mathbf{v}(x, y, 0, t) = \mathbf{v}(x, y, h, t) = \mathbf{0}$, and \mathbf{v} is periodic in x - and y -direction.

In the following we restrict ourselves to background flows that can be written in the form

$$\mathbf{U}(\mathbf{x}) \equiv U\phi(\zeta)\hat{\mathbf{x}}; \quad \phi(0) = 0, \quad \phi(1) = 1, \quad (3.10)$$

with a merely height-dependent profile function ϕ ; the argument $\zeta \equiv z/h$ is the dimensionless coordinate in the cross-stream direction. We thus exclude background flows that have a spanwise structure. In addition, we require $\phi(\zeta) = 1 - \phi(1 - \zeta)$, so that our background flow profiles reflect the symmetry of the geometry. Defining the profile functional

$$D\{\phi\} \equiv \int_0^1 d\zeta [\phi'(\zeta)]^2 - 1 \quad (3.11)$$

and introducing the dimensionless balance parameter a , the variational principle for calculating the best upper bounds on $c_\varepsilon(Re)$ that the background flow method with the trial flows (3.10) has to offer stems from the inequality (see chapter 2 for a detailed derivation)

$$c_\varepsilon(Re) \leq \inf_{\phi, a > 1} \left\{ \left[1 + \frac{a^2}{4(a-1)} D\{\phi\} \right] Re^{-1} \right\}, \quad (3.12)$$

¹According to F. H. Busse (private communication, 1996), this uncertainty may be of the order of 20%.

which is subject to a *spectral constraint*: ϕ and a have to be chosen such that all eigenvalues λ of the linear eigenvalue problem

$$\left. \begin{aligned} \lambda \mathbf{V} &= -2h^2 \Delta \mathbf{V} + R\phi' \begin{pmatrix} 0 & 0 & 1 \\ 0 & 0 & 0 \\ 1 & 0 & 0 \end{pmatrix} \mathbf{V} + \nabla P, \\ 0 &= \nabla \cdot \mathbf{V}, \quad \mathbf{V} \text{ satisfies the homogeneous b.c.} \end{aligned} \right\} \quad (3.13)$$

for the stationary velocity fields \mathbf{V} are positive. The balance parameter a enters into this eigenvalue problem via the rescaled Reynolds number

$$R \equiv \frac{a}{a-1} Re. \quad (3.14)$$

It is the presence of this balance parameter that distinguishes the variational principle (3.12) from the original principle first formulated by Doering & Constantin (1994). The balance parameter is necessary to ensure that the background flow method reproduces the known $1/Re$ -behaviour of $c_\varepsilon(Re)$ up to the energy stability limit Re_{ES} , see chapter 2.

The above principle generalizes energy stability theory in the following sense. For computing the energy stability limit Re_{ES} one decomposes the actual flow field into a sum of the stationary laminar flow and the corresponding fluctuations, and relates the time-derivative of the fluctuations' kinetic energy to a certain functional of these fluctuations (Joseph 1976; Drazin & Reid 1981). The limit is then derived by considering this functional in an enlarged space consisting of all stationary divergence-free vector fields that satisfy the same homogeneous b.c. as the fluctuations. The present decomposition (3.9) relies on a background flow \mathbf{U} that is generally not a stationary solution to the equations of motion, so that the deviations \mathbf{v} can not be considered as fluctuations around a physically realized flow. Nevertheless, following Doering & Constantin (1994) one can utilize the Navier–Stokes equations to relate ε_T to a functional of these deviations, and then derive bounds on the long-time averaged dissipation rate by seeking this functional's extrema in the enlarged space of all stationary divergence-free fields satisfying the homogeneous b.c., thereby directly paralleling the line of reasoning adopted in energy stability theory. It is the enlargement of the space of admitted functions which effectuates that, even after optimization of the background flow \mathbf{U} , the background flow method can in general not yield the exact values of $c_\varepsilon(Re)$, but provides rigorous upper bounds $\overline{c}_\varepsilon(Re)$. Deviations of experimentally measured energy dissipation rates from these upper bounds thus characterize to which extent the actual solutions to the Navier–Stokes equations explore the enlarged function space.

Even though this background flow approach and Busse's Optimum Theory appear to be profoundly different on a first glance — somewhat arbitrary fields \mathbf{U} here, genuine mean flows

there — there exists an intriguing connection between them that has recently been unraveled by Kerswell (1997). By implementing the spectral constraint with the help of a Lagrange multiplier technique, this author was able to recast the technical problem of optimizing the background flow into a nonlinear Euler–Lagrange problem quite similar to that appearing in Busse’s theory. Applying Busse’s multi- α technique to this new problem and comparing in this way the best bounds $\overline{c}_\varepsilon^{BF}(Re)$ obtainable with the background flow method to the bounds $\overline{c}_\varepsilon^{OT}(Re)$ provided by the Optimum Theory, Kerswell obtained the exact identity

$$\lim_{Re \rightarrow \infty} \overline{c}_\varepsilon^{BF}(Re) = \lim_{Re \rightarrow \infty} \overline{c}_\varepsilon^{OT}(Re). \quad (3.15)$$

In spite of this formal identity there remain significant differences between the minimizing background flow and the mean flow occurring in Busse’s theory. If the profile function ϕ is chosen optimally, the plane-averaged fluctuations around the background flow vanish (see Kerswell 1997) as do, by construction, the fluctuations around Busse’s plane-averaged flow, but nevertheless in the limit $Re \rightarrow \infty$ this latter flow has a slope of $\frac{1}{4}U/h$ in the interior (Busse 1970, 1978, 1996), whereas the slope of the optimal profile ϕ vanishes.

It should be kept in mind that the background flow $\mathbf{U}(\mathbf{x}) = U\phi(\zeta)\hat{\mathbf{x}}$ is *not* a horizontally-averaged mean flow. However, as also emphasized by Kerswell (1997), the optimal background profile seems to invite comparison with experimental data. We do not aim at such a comparison, but merely consider the optimal profile as the result of the variational principle. Nevertheless, when describing the profile in the vicinity of the plates, we will use the term “boundary layers”, without implying that these are equal to the physical boundary layers.

From the computational viewpoint, a considerable advantage of the background flow method stems from its great flexibility. It can easily be adapted to other flow geometries, and for the purpose of constructing upper bounds on c_ε it is *not* necessary to know the optimal profile (or the optimal three-dimensional background flow) beforehand. *Any* profile ϕ of the required form, in combination with an *arbitrary* $a > 1$, gives rise to a maximal Reynolds number Re_c up to which the spectral constraint is fulfilled; by means of (3.12) one then obtains from that particular pair (ϕ, a) an exact upper bound on c_ε for all $Re < Re_c$.

The further treatment of the variational principle can be simplified considerably by observing that the optimization of the balance parameter a separates from the optimization of the profile function itself. Let us assume for the moment that we already have a method to evaluate the spectral constraint, i.e. to determine for an arbitrary ϕ that rescaled Reynolds number $Re_c\{\phi\}$ where the lowest eigenvalue of (3.13) passes through zero. Then according to (3.12) this ϕ yields

an upper bound on c_ε ,

$$c_\varepsilon \leq \left[1 + \frac{a_{opt}^2}{4(a_{opt} - 1)} D\{\phi\} \right] Re^{-1} \quad \text{for } 0 \leq Re < R_c\{\phi\}. \quad (3.16)$$

Taking into account the spectral constraint and (3.14), the optimization of a gives

$$a_{opt} = \begin{cases} 2 & \text{for } 0 \leq Re < \frac{1}{2}R_c\{\phi\} \\ \frac{R_c\{\phi\}}{R_c\{\phi\} - Re} & \text{for } \frac{1}{2}R_c\{\phi\} \leq Re < R_c\{\phi\} \end{cases}. \quad (3.17)$$

Hence we obtain

$$c_\varepsilon \leq \begin{cases} [1 + D\{\phi\}] Re^{-1} & \text{for } 0 \leq Re < \frac{1}{2}R_c\{\phi\} \\ \left[1 + \frac{D\{\phi\}R_c\{\phi\}^2}{4(R_c\{\phi\} - Re)Re} \right] Re^{-1} & \text{for } \frac{1}{2}R_c\{\phi\} \leq Re < R_c\{\phi\} \end{cases}. \quad (3.18)$$

This inequality yields a strategy towards a constructive solution to the variational principle that comprises two essentially independent steps: we first have to compute for every profile ϕ from a suitable class of test functions the corresponding value $R_c\{\phi\}$; in a second step we have to minimize the bounds provided by (3.18) by varying the profiles within the chosen class.

Figure 3.1 shows a typical graph of an upper bound (3.18) produced by a generic profile ϕ . Considered as a function of the Reynolds number, such an upper bound is continuous and even continuously differentiable at $Re = \frac{1}{2}R_c\{\phi\}$; it has exactly one minimum in the whole interval $0 \leq Re < R_c\{\phi\}$. This minimum appears in the upper half of this interval, i.e. for $\frac{1}{2}R_c\{\phi\} \leq Re < R_c\{\phi\}$.

The variation over a set of profile functions ϕ amounts to considering all their graphs in the (Re, c_ε) -plane; the optimal upper bound on $c_\varepsilon(Re)$ is then given by the lower envelope of these graphs. Provided the Re -dependence of this envelope is merely weak as compared with a graph originating from a particular profile ϕ , the only point that this ϕ can possibly contribute to the optimal bound $\bar{c}_\varepsilon(Re)$ — if any point at all — is its minimum point. The proviso obviously holds close to possible extrema of the bound, and in the limit $Re \rightarrow \infty$, where the bound becomes flat. Thus, we obtain a mapping from a profile ϕ to a point in the (Re, c_ε) -plane,

$$\phi \mapsto (Re_{min}\{\phi\}, \bar{c}_\varepsilon(Re_{min}\{\phi\})); \quad (3.19)$$

here $\bar{c}_\varepsilon(Re_{min}\{\phi\})$ denotes the right hand side of (3.18) (for the profile ϕ considered) at $Re = Re_{min}\{\phi\}$. Minimizing the bound (3.18) with respect to Re , one sees that the Reynolds number

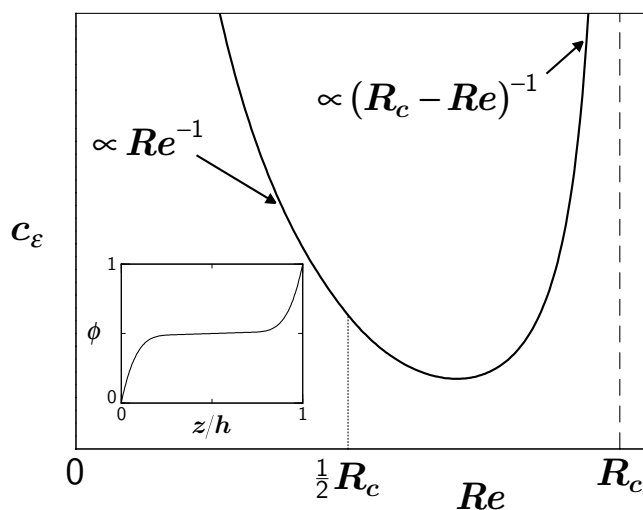


Figure 3.1: Graph of an upper bound on c_ε produced by the generic profile ϕ sketched in the inset.

$Re_{min}\{\phi\}$ of the minimum point can be expressed as

$$Re_{min}\{\phi\} = X_0\{\phi\} R_c\{\phi\}, \quad (3.20)$$

where $X_0\{\phi\}$ is the unique (real) zero of the cubic polynomial

$$x^3 - 2x^2 + \left(1 - \frac{3}{4}D\{\phi\}\right)x + \frac{1}{2}D\{\phi\} = 0 \quad (3.21)$$

that can be found between $\frac{1}{2}$ and 1, i.e. $\frac{1}{2} \leq X_0\{\phi\} < 1$. This idea of associating with each profile ϕ a *profile point* in the (Re, c_ε) -plane, such that the lower envelope of all these points yields the desired upper bound on $c_\varepsilon(Re)$, is of central importance for our approach to the variational principle. We emphasize that by its very construction the mapping (3.19) already embodies the spectral constraint.

The practical computation of upper bounds on the dissipation rate now hinges on the solution of two problems: one has to provide a method for calculating $R_c\{\phi\}$ for each given profile ϕ , i.e. for finding the rescaled Reynolds number (3.14) where the smallest eigenvalue of the eigenvalue problem (3.13) passes through zero, and one has to develop a procedure for minimizing $\overline{c}_\varepsilon(Re)$, i.e. for optimizing the profile by varying its parameters. These two issues will be taken up separately in the following two sections.

3.3 Implementation of the spectral constraint

In order to non-dimensionalize the problem, we now choose the gapwidth h as the unit of length. By virtue of the linearity of the eigenvalue problem (3.13) and its homogeneous b.c. it is not necessary to explicitly specify a scale V_0 of velocity. For the sake of notational simplicity we denote the dimensionless quantities by the same symbols as their dimension-carrying counterparts. Thus, the eigenvectors \mathbf{V} of (3.13) are henceforth regarded as dimensionless functions of the dimensionless variables x , y and z ; the height variable z becomes equal to the variable ζ employed in (3.10).

Utilizing the periodic b.c., the ansatz

$$\mathbf{V}(\mathbf{x}) = \mathbf{v}(z) e^{i(k_x x + k_y y)}, \quad P(\mathbf{x}) = p(z) e^{i(k_x x + k_y y)} \quad (3.22)$$

transforms the eigenvalue equation (3.13) into the system

$$\lambda v_x = -2 \left(\partial_z^2 - (k_x^2 + k_y^2) \right) v_x + R \phi' v_z + i k_x p, \quad (3.23)$$

$$\lambda v_y = -2 \left(\partial_z^2 - (k_x^2 + k_y^2) \right) v_y + i k_y p, \quad (3.24)$$

$$\lambda v_z = -2 \left(\partial_z^2 - (k_x^2 + k_y^2) \right) v_z + R \phi' v_x + p', \quad (3.25)$$

$$0 = i k_x v_x + i k_y v_y + v_z' \quad (3.26)$$

with the b.c.

$$\mathbf{v}(0) = \mathbf{v}(1) = \mathbf{0}. \quad (3.27)$$

If both wavenumbers k_x and k_y vanish, i.e. if $\mathbf{k} \equiv (k_x, k_y)^T = \mathbf{0}$, so that $\mathbf{V}(\mathbf{x})$ and $P(\mathbf{x})$ are functions of z only, then (3.26) together with (3.27) enforces $v_z(z) = 0$. In this case all eigenvalues are strictly positive, $\lambda_n = 2\pi^2 n^2$ with $n = 1, 2, \dots$. Hence, in this trivial situation the spectral constraint is always satisfied, so that we only have to consider $\mathbf{k} \neq \mathbf{0}$ in the following.

It turns out that *all* methodical and conceptual aspects that characterize the solution procedure for the three-dimensional Couette flow appear even when the spanwise degrees of freedom are suppressed. However, in this simplified two-dimensional case the technical effort is reduced dramatically. To give but one example, the fourth-order Sturm–Liouville problem that will appear in the analysis of the simplified flow becomes a sixth-order problem in the general case, so that the system of six coupled differential equations (3.34)–(3.39) then has to be replaced by a system of 20 equations. In order to elucidate the salient features of our approach without hiding essential points behind technicalities, we confine ourselves for this and the following chapter to

the case

$$v_y(z) = 0, \quad k_y = 0, \quad (3.28)$$

and defer the detailed discussion of the unrestricted, three-dimensional Couette flow to chapter 5.

Now the condition (3.26) allows us to express $v_x(z)$ in terms of $v'_z(z)$,

$$v_x(z) = i \frac{v'_z(z)}{k_x}, \quad (3.29)$$

and to obtain an expression for $p(z)$ from (3.23),

$$p = \frac{1}{k_x^2} \left(2v_z''' - (2k_x^2 - \lambda)v_z' \right) + i \frac{R}{k_x} \phi' v_z. \quad (3.30)$$

Inserting these expressions into (3.25) we arrive at a fourth-order equation for $v_z(z)$,

$$v_z^{(4)} - \frac{1}{2} \left(4k_x^2 - \lambda \right) v_z'' + \frac{1}{2} k_x^2 \left(2k_x^2 - \lambda \right) v_z + i k_x R \phi' v_z' + \frac{1}{2} i k_x R \phi'' v_z = 0, \quad (3.31)$$

with the b.c.

$$v_z(0) = v_z'(0) = 0 \quad \text{and} \quad v_z(1) = v_z'(1) = 0. \quad (3.32)$$

Equations (3.31) and (3.32) constitute an intricate Sturm–Liouville eigenvalue problem, the solution of which can not be obtained analytically for a general curved profile ϕ . A numerical integration of (3.31) necessitates to pose suitable initial conditions at a single boundary, say $z = 0$. Defining the four-vectors

$$\mathbf{V}_z(z) \equiv (v_z(z), v_z'(z), v_z''(z), v_z'''(z))^T,$$

we consider the two fundamental solutions $\mathbf{V}_{z,1}$ and $\mathbf{V}_{z,2}$ to (3.31) that emerge from the initial conditions $\mathbf{V}_{z,1}(0) = (0, 0, 1, 0)^T$ and $\mathbf{V}_{z,2}(0) = (0, 0, 0, 1)^T$, respectively. The most general solution to (3.31) which satisfies the b.c. (3.32) at $z = 0$ is then given by a superposition of these two fundamental solutions. The additional b.c. at $z = 1$ yield the further constraint

$$\text{Det} \begin{pmatrix} v_{z,1}(1) & v_{z,2}(1) \\ v'_{z,1}(1) & v'_{z,2}(1) \end{pmatrix} = v_{z,1}(1) v'_{z,2}(1) - v_{z,2}(1) v'_{z,1}(1) = 0. \quad (3.33)$$

Hence, when directly solving the boundary value problem (3.31, 3.32) by stepwise integration

starting from $z = 0$, one has to adjust the parameters λ , k_x , and R (for given ϕ) such that (3.33) is fulfilled. However, (3.33) presents a severe numerical problem, since it involves the subtraction of two numbers of almost identical magnitude. An elegant way to overcome this difficulty is known as *compound matrix method* in the literature (see e.g. Straughan 1992): instead of integrating a system of equations for v_z and its derivatives, one first reformulates the system in terms of determinants of the kind (3.33).

To this end, we define a new six-vector

$$\mathbf{y}(z) \equiv (y_1(z), y_2(z), y_3(z), y_4(z), y_5(z), y_6(z))^T.$$

The components of this vector are the 2×2 minors of the 4×2 matrix that contains $\mathbf{V}_{z,1}$ as its first and $\mathbf{V}_{z,2}$ as its second column, i.e. of the solution matrix to the system considered above:

$$\begin{aligned} y_1 &= v_{z,1}v'_{z,2} - v'_{z,1}v_{z,2}, & y_2 &= v_{z,1}v''_{z,2} - v''_{z,1}v_{z,2}, & y_3 &= v_{z,1}v'''_{z,2} - v'''_{z,1}v_{z,2}, \\ y_4 &= v'_{z,1}v''_{z,2} - v''_{z,1}v'_{z,2}, & y_5 &= v'_{z,1}v'''_{z,2} - v'''_{z,1}v'_{z,2}, & y_6 &= v''_{z,1}v'''_{z,2} - v'''_{z,1}v''_{z,2}. \end{aligned}$$

The fourth-order equation (3.31) then leads to a system of six coupled differential equations,

$$y'_1 = y_2, \tag{3.34}$$

$$y'_2 = y_3 + y_4, \tag{3.35}$$

$$y'_3 = y_5 + \frac{1}{2}(4k_x^2 - \lambda)y_2 - ik_x R \phi' y_1, \tag{3.36}$$

$$y'_4 = y_5, \tag{3.37}$$

$$y'_5 = y_6 + \frac{1}{2}(4k_x^2 - \lambda)y_4 + \frac{1}{2}k_x^2(2k_x^2 - \lambda)y_1 + i\frac{1}{2}k_x R \phi'' y_1, \tag{3.38}$$

$$y'_6 = \frac{1}{2}k_x^2(2k_x^2 - \lambda)y_2 + ik_x R \phi' y_4 + i\frac{1}{2}k_x R \phi'' y_2. \tag{3.39}$$

The initial conditions (3.32) at $z = 0$ yield

$$\mathbf{y}(0) = (0, 0, 0, 0, 0, 1)^T, \tag{3.40}$$

and (3.33) gives an additional boundary condition at $z = 1$,

$$y_1(1) = 0. \tag{3.41}$$

This kind of asymmetric b.c. (3.40, 3.41) turns out to be very convenient for numerical analysis. An additional simplification can be obtained by reducing the complex system (3.34)–(3.39) to a real one: starting from the decomposition $\mathbf{y}(z) = \mathbf{f}(z) + ik_x \mathbf{g}(z)$ with real vector functions

$\mathbf{f}(z)$ and $\mathbf{g}(z)$, then taking $g_1(z) = 0$ successively produces the equations

$$\left. \begin{aligned} g_1 = 0, \quad g_2 = 0, \quad g_4 = -g_3, \quad g_5 = \frac{1}{2}R\phi'f_1, \\ g_6 = \frac{1}{2}(4k_x^2 - \lambda)g_3 + \frac{1}{2}R\phi'f_2, \quad f_3 = \frac{1}{2}(4k_x^2 - \lambda)f_1 + f_4, \end{aligned} \right\} \quad (3.42)$$

where we have used $\phi'(z) \neq 0$. These equations are consistent with the initial conditions (3.40), so that we arrive at a closed system of merely six real differential equations:

$$f_1' = f_2, \quad (3.43)$$

$$f_2' = \frac{1}{2}(4k_x^2 - \lambda)f_1 + 2f_4, \quad (3.44)$$

$$g_3' = -\frac{1}{2}R\phi'f_1, \quad (3.45)$$

$$f_4' = f_5, \quad (3.46)$$

$$f_5' = \frac{1}{2}k_x^2(2k_x^2 - \lambda)f_1 + \frac{1}{2}(4k_x^2 - \lambda)f_4 + f_6, \quad (3.47)$$

$$f_6' = \frac{1}{2}k_x^2(2k_x^2 - \lambda)f_2 + k_x^2R\phi'g_3. \quad (3.48)$$

The corresponding initial conditions are

$$f_6(0) = 1, \quad \text{all other components vanish at } z = 0; \quad (3.49)$$

the condition at $z = 1$ reads

$$f_1(1) = 0. \quad (3.50)$$

For a given profile ϕ and a given set of parameters λ , k_x , and R , the unique solution to the initial value problem (3.43)–(3.49) together with the expressions (3.42) constitute the unique solution to the initial value problem (3.34)–(3.40). Thus, solving the Sturm–Liouville eigenvalue problem (3.31, 3.32) becomes equivalent to solving the boundary value problem (3.43)–(3.50).

Not only is the number of equations effectively halved by going from the complex system (3.34)–(3.39) to the real system (3.43)–(3.48), but also the equations themselves become simpler; in particular, the profile ϕ enters into the final system only through its first derivative. It seems that this system captures the symmetries in an optimal way, which is also reflected by the fact that it contains only the square of the wavenumber k_x . Hence, we can consider the absolute value $k \equiv |k_x|$ instead of k_x in the following.

For $\lambda \leq 2k^2$ and monotonous profiles with $\phi'(z) > 0$, there is only one crucial minus sign in the system (3.43)–(3.48), namely the one on the right hand side of (3.45). This fact allows us to understand intuitively how the initial value problem “works”: starting with f_6 (see (3.49)), the

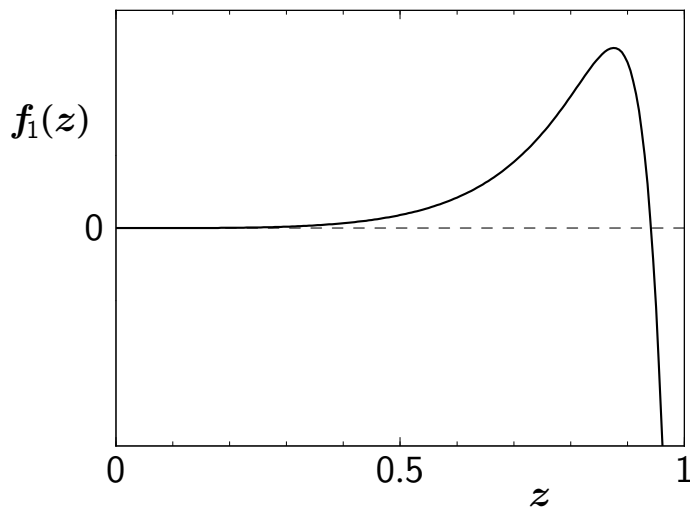


Figure 3.2: Behaviour of $f_1(z)$ for a generic profile ϕ and typical parameters k and R ; the value of λ has been set to zero.

components f_5 , f_4 , f_2 and f_1 are driven successively. According to (3.45), g_3 is then driven with an opposite sign — the strength of the drive being regulated by the product $R\phi'$ — and acts back on f_6 . If this feedback is so strong that f_6 itself becomes negative, the whole dynamics are repeated with opposite sign.

Figure 3.2 depicts the behaviour of the component $f_1(z)$ for a generic profile ϕ and typical parameters k and R ; the value of λ has been set to zero. Obviously, the b.c. (3.50) is fulfilled — an eigenvalue of (3.13) has been found — when a zero of $f_1(z)$ occurs at $z = 1$. As is clear from the above discussion, all eigenvalues of (3.13) will be positive for $R = 0$. Remember that our aim is to determine for any given profile ϕ that R -value $R_c\{\phi\}$ where the lowest eigenvalue passes through zero. We do so by keeping $\lambda = 0$ fixed when solving the system (3.43)–(3.48) numerically for a representative set of wavenumbers k , and monitor for each such k the dependence of $f_1(1)$ on R . In this way we identify the lowest value $R_0\{\phi\}(k)$ of the rescaled Reynolds number where the condition (3.50) is satisfied, i.e. the lowest zero of $f_1(1)$ as a function of R . The continuous dependence of the (discrete) eigenvalues of (3.13) on both the profile ϕ and the parameters R and k guarantees that this zero indeed corresponds, for the considered ϕ and k , to the passage of the lowest eigenvalue through zero. To give an example, figure 3.3 shows the dependence of $f_1(1)$ on R for the same profile ϕ and the same wavenumber k as considered in figure 3.2. The first zero of this function gives $R_0\{\phi\}(k)$.

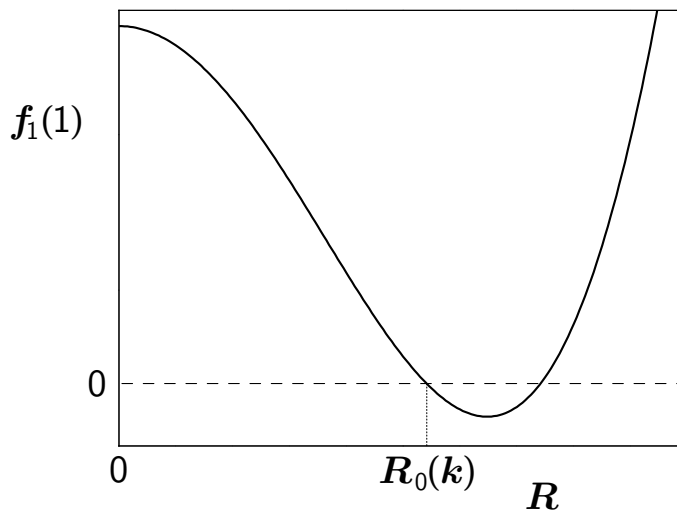


Figure 3.3: $f_1(1)$ as a function of R for the same profile ϕ and the same wavenumber k as considered in figure 3.2. The first zero of this function gives the value $R_0\{\phi\}(k)$.

The value $R_0\{\phi\}(k)$ found in this way is a functional of the profile ϕ and a function of the wavenumber k . Since the periodicity length L_x (and hence the wavenumber k_x) is a dummy variable in the actual problem, one has to determine the desired value $R_c\{\phi\}$ in a further step by minimizing over all k :

$$R_c\{\phi\} \equiv \min_{k>0} \{R_0\{\phi\}(k)\}. \quad (3.51)$$

Thus, for each profile ϕ the evaluation of the spectral constraint requires both the solution of a set of linear eigenvalue problems labeled by the wavenumber k , *and* a subsequent minimization. Figure 3.4 illustrates the k -dependence of $R_0\{\phi\}(k)$, again for a generic ϕ . It should be noted that both steps, the identification of the first zero of the R -dependent function $f_1(1)$ for each k , and the minimization over k , can efficiently be implemented with the help of standard numerical routines.

3.4 Minimization of the upper bound

Having supplied a method for computing $R_c\{\phi\}$ for arbitrary profiles ϕ , and thus for finding their profile points (3.19), we can now turn to the actual minimization of the upper bound on $c_\varepsilon(Re)$.

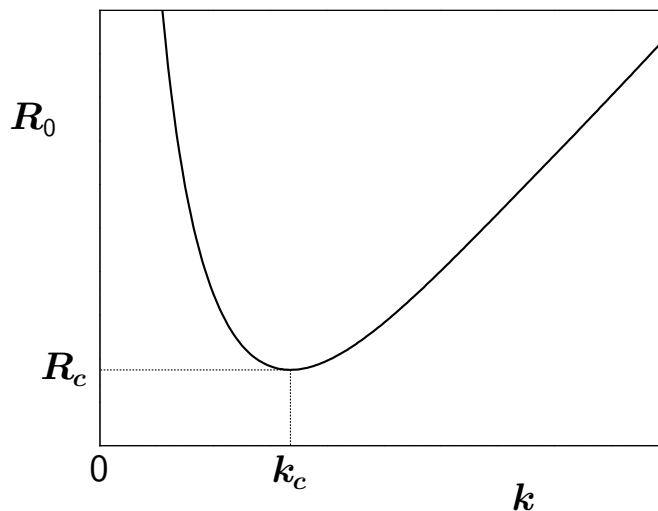


Figure 3.4: Behaviour of $R_0\{\phi\}(k)$ as a function of k for a generic profile ϕ , and the ensuing minimum $R_c\{\phi\}$ at the wavenumber k_c .

We first have to specify the class of test profiles within which the variation is going to take place. To this end, we characterize these profiles ϕ by as few as possible and physically reasonable parameters. An educated guess for an useful class of test profiles can be made by recalling previous results: following Doering & Constantin (1992, 1994), one can verify the admissibility of a profile to the variational principle (3.12) by means of functional estimates. In this way the actual spectral constraint (3.13) is oversatisfied, so that one does no longer obtain the best possible bounds, but with such an *over-restrictive profile constraint* the variational principle can be solved analytically (see chapter 2). For $Re > 20\sqrt{2}$ the resulting profiles consist of parabolic boundary segments of thickness $\delta < \frac{1}{2}$ and a connecting line with zero slope in the interior, $\phi(z) = \frac{1}{2}$ for $\delta < z < 1 - \delta$. However, remembering that the slope of Busse's (1970, 1978, 1996) mean flows does not vanish, whereas Kerswell (1997) obtained zero-slope profiles for $Re \rightarrow \infty$ when applying multi- α techniques to his Euler–Lagrange problem, it is clear that the slope p of the profiles in the interior of the fluid should be one of the variational parameters.

Hence, a simple but promising class of test profiles consists of functions $\phi(z)$ with parabolic boundary segments of thickness δ ($0 < \delta < \frac{1}{2}$) that merge into a straight line with slope p ($0 < p \leq 1$). We require that $\phi(z)$ be continuous and continuously differentiable at the merging points $z = \delta$ and $z = 1 - \delta$. Our variational profiles are thus fully characterized by the two

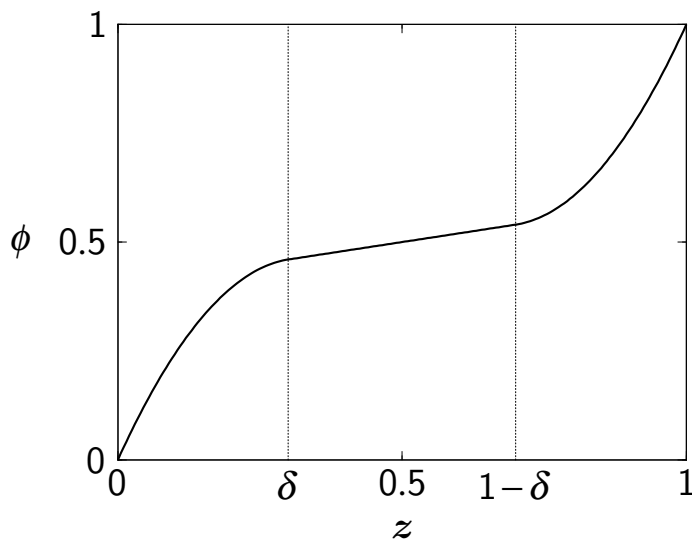


Figure 3.5: Example of a profile $\phi(z)$ as defined by (3.52) ($\delta = 0.3$ and $p = 0.2$).

parameters δ and p ,

$$\phi(z) = \begin{cases} (\delta p + (1-p))z/\delta - \frac{1}{2}(1-p)(z/\delta)^2 & \text{for } 0 \leq z \leq \delta \\ \frac{1}{2}(1-p) + pz & \text{for } \delta < z < 1-\delta \\ 1 - (\delta p + (1-p))(1-z)/\delta + \frac{1}{2}(1-p)((1-z)/\delta)^2 & \text{for } 1-\delta \leq z \leq 1 \end{cases} \quad (3.52)$$

their derivatives read

$$\phi'(z) = \begin{cases} p + (1-p)(1-z/\delta)/\delta & \text{for } 0 \leq z \leq \delta \\ p & \text{for } \delta < z < 1-\delta \\ p + (1-p)(1-(1-z)/\delta)/\delta & \text{for } 1-\delta \leq z \leq 1 \end{cases} \quad (3.53)$$

Figure 3.5 depicts such a profile $\phi(z)$.

The profile functional (3.11) now becomes a function of δ and p ,

$$D\{\phi\} = \left(\frac{2}{3\delta} - 1\right)(1-p)^2 \equiv \mathcal{D}(\delta, p). \quad (3.54)$$

After $R_c\{\phi\} \equiv \mathcal{R}_c(\delta, p)$ has been computed numerically and the zero $X_0\{\phi\} \equiv \mathcal{X}_0(\delta, p)$ of the cubic polynomial (3.21) has been determined, each parameter pair (δ, p) can be mapped according

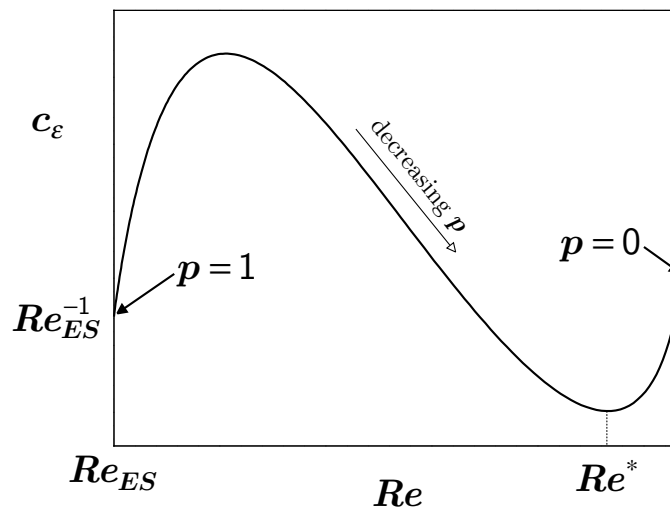


Figure 3.6: Graph of \bar{c}_ε that emerges when the slope p is varied between 1 and 0 while the width δ of the boundary layers is kept fixed. Starting at the point $(Re = Re_{ES}, c_\varepsilon = Re_{ES}^{-1})$, the Reynolds number increases monotonously with decreasing p . For constructing the optimal upper bound only points in the vicinity of the minimum at Re^* are of interest.

to (3.19) to its profile point in the (Re, c_ε) -plane; the lower envelope of all these points will yield the graph of the optimal upper bound on the dissipation rate.

We display in figure 3.6 a graph that emerges by connecting all the profile points when p is varied while δ is kept fixed. Such a graph will be referred to as a p -graph. Starting at the point $(Re = Re_{ES}, c_\varepsilon = Re_{ES}^{-1})$ marking the energy stability limit (where $p = 1$), the Reynolds number increases monotonously with decreasing p . At a certain Reynolds number Re^* , there occurs a characteristic minimum. Comparing such p -graphs for various values of δ , we find that this minimum is shifted to larger Re when δ is decreased; in addition, the height of the maximum between Re_{ES} and Re^* increases. The lower envelope of all these p -graphs is formed by points close to their respective minima, so that only such points have to be taken into account when searching the optimal upper bound.

Since we are not only interested in obtaining a finite number of points of the graph of $\bar{c}_\varepsilon(Re)$, but we also wish to extract the Re -dependence of the optimal profile parameters with as little numerical scatter as possible, it turns out to be advantageous if the abscissas of the minima of the individual p -graphs employed in the construction of the lower envelope are about evenly spaced.

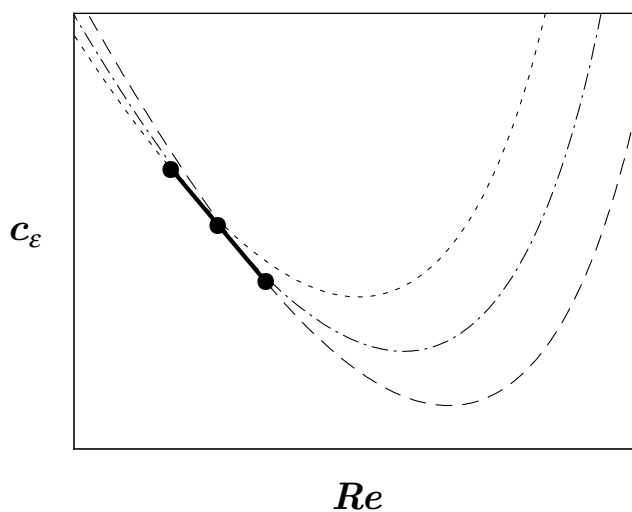


Figure 3.7: Illustration of the envelope technique for obtaining optimal upper bounds on $c_\varepsilon(Re)$. The dashed lines are p -graphs close to their respective minima (cf. figure 3.6); their parameters δ have been chosen such that the abscissas of these minima are about evenly spaced. Bullets indicate three points that belong to the optimal bound. There is one such point for each p -graph; they are determined in the order of increasing Re by the requirement that the slope of the connecting lines be minimal. The parameter pairs (δ, p) corresponding to these points characterize the profiles (3.52) that are optimal at the respective values of Re .

From the solution of the variational principle with over-restrictive profile constraint (chapter 2) we expect that the optimized parameter δ will scale with the inverse Reynolds number,

$$\delta_{opt} \sim \alpha Re^{-1} \quad (+ \text{ possible small corrections}),$$

with some constant α . In order to resolve the bound $\overline{c_\varepsilon}(Re)$ on an almost linear scale, i.e. with an almost constant stepsize ΔRe , we therefore consider a set of p -graphs with parameters δ that are consecutively diminished by quadratically decreasing steps:

$$\Delta\delta = - \left(\delta^2 / \alpha \right) \Delta Re. \quad (3.55)$$

To obtain a linear resolution on a logarithmic scale we adjust the stepsize $\Delta\delta$ accordingly.

Figure 3.7 illustrates the envelope technique used in practice for finding the parameters of optimal profiles. Starting with a point on the leftmost p -graph, we single out a point on the next

p -graph by the requirement that the slope of the line connecting the two points be minimal. Repeating this process, we can determine for each δ that contributes a p -graph the corresponding value p that belongs to the optimal profile (3.52) at the respective value of the Reynolds number. Connecting all points obtained in this way by line segments, we obtain a piecewise linear approximation to the graph of the optimal upper bound on the dissipation rate.

With the help of this algorithm we can construct optimal upper bounds on $c_\varepsilon(Re)$ for all Reynolds numbers of practical interest. The algorithm is not only efficient in the sense that it does not require large amounts of CPU-time, it is also quite accurate: it provides optimal parameters which possess no scatter beyond numerical roundoff errors when considered as functions of the Reynolds number, even when Re varies over several orders of magnitude. This smoothness of the numerical data will allow us to identify a well defined scaling behaviour of the optimal parameters.

3.5 Characteristic phenomena and problems

When performing the optimization described in the preceding two sections in practice, one encounters some characteristic phenomena that accompany the increase of the Reynolds number. These phenomena are not merely technical or numerical issues, but reflect the structure of the entire process that determines the optimal bound.

Above all, it has to be realized that the spectral constraint (3.13) acts as a sort of filter for the admissible profiles when Re , and hence R , becomes large. Regardless of the particular parametrization, the constraint singles out only those profiles that possess a large slope in the vicinity of the boundaries, but are comparatively flat in the interior. This can be understood as follows: the eigenvalue problem (3.13) takes on its simplest possible form if the derivative of the profile function is constant. The only profile with constant derivative satisfying the required b.c. (3.10) is that of laminar flow. With this profile the eigenvalue problem becomes that which appears in the energy stability theory of plane Couette flow, the only difference is that the Reynolds number now is replaced by the rescaled Reynolds number R , see (3.14). Consequently, for the laminar profile the critical value R_c is equal to Re_{ES} . If there were no need to keep $\phi(0) = 0$ and $\phi(1) = 1$ fixed, one could readily obtain the desired increase of $R_c\{\phi\}$ by simply decreasing the slope of the profile, i.e. by utilizing linear profiles ϕ with a slope less than 1 within the entire fluid layer. However, in order to satisfy these b.c. we have to modify such linear profiles appropriately. The decisive point to observe is that the eigenvectors \mathbf{V} of (3.13) not only have to vanish at the boundaries $z = 0$ and $z = 1$, but also the increase of \mathbf{V} in the vicinity of these boundaries is hindered by the condition $\nabla \cdot \mathbf{V} = 0$. Hence, if we steepen the linear profiles only in the vicinity of the boundaries so that they satisfy the b.c. posed in (3.10), then such a modification will influence the eigenvalue problem much less than any other possible profile modification within the interior would do, thus keeping $R_c\{\phi\}$ as high as possible. This

is the selection mechanism for the profiles that remain admissible for the variational principle (3.12) in the regime of large Re . Profiles with steep slopes within thin boundary layers thus emerge by necessity, so that the following issues are not tied to our particular parametrization (3.52) but are intrinsic features of the background flow method applied to the plane Couette flow.

Intimately connected to the shape of the admissible profiles is the behaviour of $R_0\{\phi\}(k)$, considered as a function of the wavenumber k . Namely, the minimum structure of these functions changes at Reynolds numbers around 860: the single minimum occurring at lower Re splits into two separate minima. One therefore obtains two branches of minimizing wavenumbers, one of them approaching a constant with increasing Reynolds number, the other scaling proportionally to Re . This fact forces us to keep track of two substantially different k -regimes when seeking the minima of $R_0\{\phi\}(k)$ for large Re , and to ensure that the numerically selected value $R_c\{\phi\}$ (cf. figure 3.4) actually corresponds to the global minimum. It will turn out that, as a consequence of the variational principle, both minima adopt the *same* value R_c , and that this balance is crucial for the scaling properties of the variational parameters and of $\bar{\tau}_\varepsilon(Re)$ itself.

The inevitable emergence of large k -values poses two problems for the numerical procedure. The first of these problems shows up in the behaviour of the zeros of $f_1(1)$ considered as a function of R , see figure 3.3. For a fixed boundary-layer-type profile ϕ and large wavenumbers, the lowest two zeros approach each other and finally coalesce in the limit $k \rightarrow \infty$. More generally, the zeros tend to get paired with increasing k . To give an example for the required numerical accuracy, we state the first four zeros for the parameters $\delta = 0.2$, $p = 0.1$, and $k_x/2\pi = 10$: the first and second zero occur at $R_{0,1} = 5163.1861608127(1)$ and $R_{0,2} = 5163.1861608128(1)$, the third and fourth at $R_{0,3} = 9249.8064085203(1)$ and $R_{0,4} = 9249.8064085204(1)$; here and in the following the numbers in brackets give the uncertainty of the last digit. We are thus faced with the problem of distinguishing two closely spaced zeros, which can be overcome by first locating the minimum between those zeros and then using this minimum as starting value in a root-finding routine. The feasibility of this strategy rests on the fact that the first pair of zeros remains well separated from the second.

The second numerical problem stemming from large wavenumbers concerns the system of differential equations (3.43)–(3.48), with λ set to zero: it needs to be rescaled in order to reach the regime of large k . We define the new variables

$$\begin{aligned} q_1(z) &\equiv k^4 f_1(z) e^{-2kz}, & q_2(z) &\equiv \frac{1}{2} k^3 f_2(z) e^{-2kz}, & q_3(z) &\equiv 2k^3 g_3(z) e^{-2kz}, \\ q_4(z) &\equiv k^2 f_4(z) e^{-2kz}, & q_5(z) &\equiv \frac{1}{2} k f_5(z) e^{-2kz}, & q_6(z) &\equiv f_6(z) e^{-2kz}. \end{aligned}$$

The powers of k in this transformation are determined by the requirement that all components of the rescaled system be of the same order of magnitude even for large k ; the common damping

factor $\exp(-2kz)$ compensates an exponential growth of the components of the previous system (3.43)–(3.48). We will discuss in the next chapter of this thesis why the value of the damping constant must be precisely $2k$.

Thus, the system of equations suitable for high- Re -analysis reads

$$q'_1 = 2k[-q_1 + q_2], \quad (3.56)$$

$$q'_2 = 2k\left[\frac{1}{2}q_1 - q_2 + \frac{1}{2}q_4\right], \quad (3.57)$$

$$q'_3 = -2kq_3 - \frac{R}{k}\phi'q_1, \quad (3.58)$$

$$q'_4 = 2k[-q_4 + q_5], \quad (3.59)$$

$$q'_5 = 2k\left[\frac{1}{4}q_1 + \frac{1}{2}q_4 - q_5 + \frac{1}{4}q_6\right], \quad (3.60)$$

$$q'_6 = 2k[q_2 - q_6] + \frac{R}{2k}\phi'q_3; \quad (3.61)$$

its initial conditions $\mathbf{q}(0) = (0, 0, 0, 0, 0, 1)^T$ are supplemented by the boundary condition $q_1(1) = 0$. With the help of this system we have computed $\overline{c}_\varepsilon(Re)$ for Reynolds numbers up to 10^7 , without encountering any kind of stability problem.

3.6 Results

Figure 3.8 shows the optimal upper bound on $c_\varepsilon(Re)$ that results from optimizing the test profiles (3.52), together with the lower bound $\underline{c}_\varepsilon(Re) = Re^{-1}$ (solid line at the left). Besides utilizing the techniques described above, we could obtain an additional slight improvement of the upper bound by taking into account that the profile point contributed by an individual ϕ deviates slightly from its minimum point (see (3.19)) if the slope of $\overline{c}_\varepsilon(Re)$ does not vanish.

The energy stability limit for the Couette flow with suppressed spanwise degrees of freedom is determined as

$$Re_{ES} = 177.21418680(1). \quad (3.62)$$

Below this Reynolds number the upper and lower bound on c_ε coincide, see (3.7), so that

$$c_\varepsilon(Re_{ES}) = Re_{ES}^{-1} = 0.56428890827(4) \times 10^{-2}. \quad (3.63)$$

At Re_{ES} the upper bound resulting from the variational principle is continuous, but obviously not continuously differentiable; $\overline{c}_\varepsilon(Re)$ increases with Re for Reynolds numbers slightly above Re_{ES} . This is no artifact tied to our particular class of test profiles, but a generic feature of the method. Even much more sophisticated parametrizations of the profiles yield the same

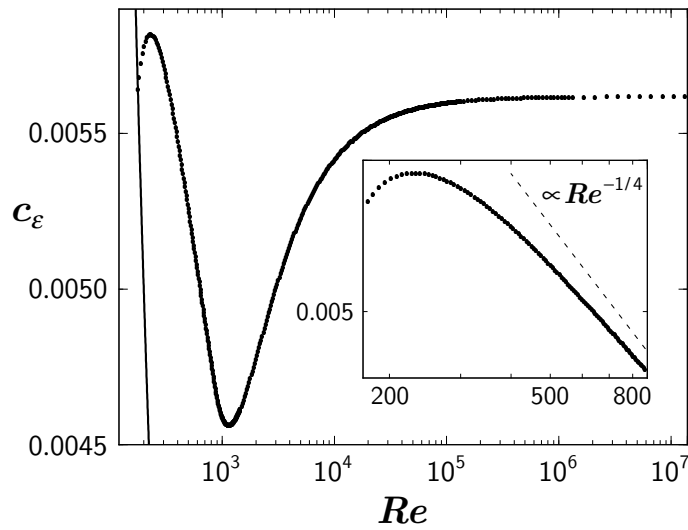


Figure 3.8: Bounds on c_ε . Points denote the optimal upper bound $\overline{c_\varepsilon}(Re)$ that can be obtained from the test profiles (3.52); the solid line at the left is the lower bound $\underline{c_\varepsilon}(Re) = Re^{-1}$. The inset shows the upper bound on a doubly logarithmic scale for Reynolds numbers between Re_{ES} and Re_B , see (3.66); the dashed line has the “asymptotic” slope predicted by (3.68).

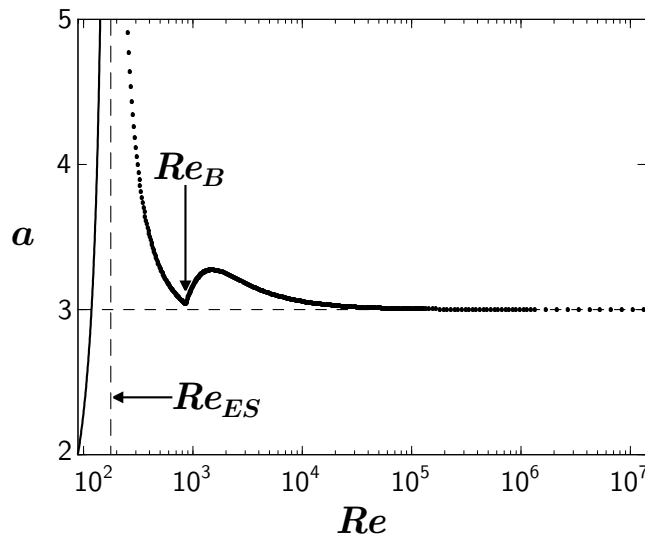


Figure 3.9: Balance parameter a for the optimal upper bound on c_ε as a function of the Reynolds number. For $Re < Re_{ES}$ this parameter is known analytically, see (3.17), and drawn as a solid line. For $Re > Re_{ES}$ the data points correspond to the bound depicted in figure 3.8. The vertical arrow marks the bifurcation number Re_B , see (3.66).

qualitative picture in the vicinity of Re_{ES} , and the possible quantitative improvement turns out to be insignificant.

This interesting fact is related to the balance parameter a : the upper bound provided by the variational principle (3.12) with over-restrictive profile constraint, as calculated analytically in the preceding chapter, shows a similar discontinuity of the derivative, albeit already at $Re = 16\sqrt{2}$, whereas there is no such discontinuity in the corresponding result obtained by Gebhardt *et al.* (1995) from the original Doering–Constantin principle, which implicitly fixes the balance parameter at the value $a = 2$. The Re -dependence of the optimal balance parameter that corresponds to the bound $\bar{c}_\varepsilon(Re)$ displayed in the previous figure is depicted in figure 3.9. Starting with the Doering–Constantin value $a = 2$ at $Re = \frac{1}{2}Re_{ES}$, it tends to infinity at $Re = Re_{ES}$. There is a kind of transition in the sense that the deviations \mathbf{v} from the background flow \mathbf{U} change their role abruptly at $Re = Re_{ES}$. Namely, for Reynolds numbers below Re_{ES} these deviations are fluctuations around a physically realizable flow, i.e. around a stationary solution to the equations of motion, but this is no longer the case for $Re > Re_{ES}$. The balance parameter then descends to the asymptotic value $a = 3$ which is known from analytical considerations (chapter 2). It shows a kink at a Reynolds number Re_B , the significance of which will become obvious later.

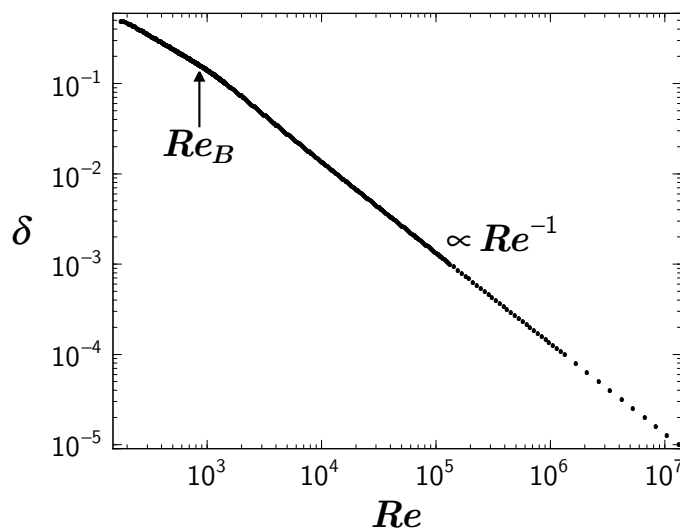


Figure 3.10: Optimal parameter δ , which denotes the thickness of the profiles' boundary layers, as a function of the Reynolds number. The arrow marks the bifurcation number Re_B .

A further characteristic feature of the optimal upper bound on c_ε shown in figure 3.8 is a distinct minimum that appears at about those Reynolds numbers where real shear flows become turbulent. We then find a cross-over at Reynolds numbers between 10^4 and 10^5 to an asymptotic regime. In the asymptotic limit $Re \rightarrow \infty$ the bound approaches the constant value

$$\lim_{Re \rightarrow \infty} \bar{c}_\varepsilon(Re) = 0.56184(1) \times 10^{-2}. \quad (3.64)$$

In order to obtain more insight into the structure of the problem, we now consider the optimal profile parameters δ (the thickness of the boundary layers) and p (the profile slope in the interior) as functions of Re for $Re > Re_{ES}$. Figures 3.10 and 3.11 reveal that both parameters obey simple scaling laws in the asymptotic regime,

$$\delta \sim \alpha Re^{-1}, \quad p \sim \beta Re^{-1}; \quad (3.65)$$

with constants α and β . Note that this Re -dependence of the profile parameters is a true outcome of the optimization procedure and does *not* follow from our choice (3.55) of the pre-optimized values of δ that have contributed a p -graph to this procedure. This choice was made for numerical efficiency only. If the δ -stepsize is chosen differently, we still obtain the scaling (3.65). The accuracy of our method is emphasized by the fact that the numerically obtained optimal parameters do not show any noticeable scatter.

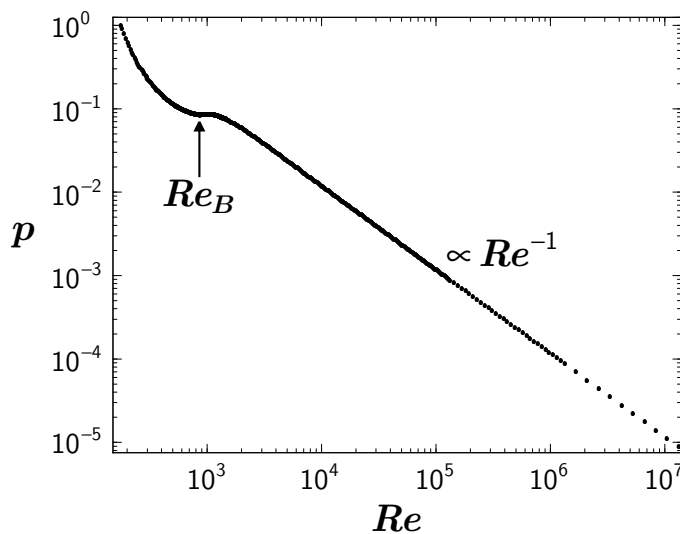


Figure 3.11: Optimal parameter p , which denotes the slope of the profiles in the interior, as a function of the Reynolds number. The arrow again marks the bifurcation number Re_B .

The most remarkable observation is that the Re -dependence of both parameters exhibits a pronounced change at

$$Re_B \approx 860, \quad (3.66)$$

as indicated by the arrows in figures 3.10 and 3.11. The width δ of the boundary layer alters its Re -dependence from an approximate $Re^{-3/4}$ -law to the Re^{-1} -scaling. The change of the slope p is even more dramatic; p has a kink at Re_B . Likewise, the optimized balance parameter a has a kink, as shown in figure 3.9. These abrupt changes are caused by a phenomenon that has already been mentioned in § 5, namely the splitting of the single minimum of the functions $R_0\{\phi\}(k)$ into a double minimum. The variational problem possesses the property that for $Re > Re_B$ the optimal parameter p (for given δ , cf. figures 3.6 and 3.7) is uniquely determined by the condition that both minimal values of $R_0\{\phi\}(k)$ be equal. Expressed in mathematical terms: *two eigenvalues of (3.13) characterized by two different wavenumbers pass through zero simultaneously*. The resulting bifurcation of those wavenumbers that characterize the passage of the lowest eigenvalues of (3.13) through zero is featured in figure 3.12. For high Re the upper k -branch k_2 apparent in this figure scales proportionally to Re , whereas the lower branch k_1 approaches a constant value in the limit $Re \rightarrow \infty$. This *asymptotic* value coincides, within numerical accuracy, with the wavenumber k_{ES} that characterizes the zero eigenvalue *at the*

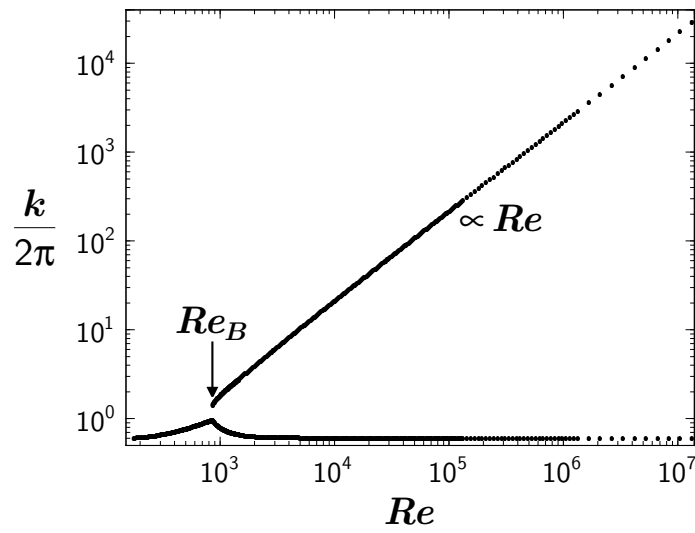


Figure 3.12: Plot of the wavenumber(s) k that minimize $R_0\{\phi\}(k)$, as function(s) of Re . For Reynolds numbers above Re_B two different k -branches appear. This corresponds to the simultaneous passage of two different eigenvalues of (3.13) through zero. The apparent discontinuity at the bifurcation point results from the finite Re -resolution.

energy stability limit:

$$\lim_{Re \rightarrow \infty} \frac{k_1}{2\pi} = \frac{k_{ES}}{2\pi} = 0.6026776(1). \quad (3.67)$$

This striking observation provides a key for an analytical asymptotic theory that will be elaborated in the next chapter of this thesis.

The splitting of a single minimum into a double minimum, strongly reminiscent of a pitchfork bifurcation, is a clear signature of the nonlinearity that is inherent in the optimization process as a whole. Even though the main technical problem of the background flow method consists in determining the value $R_0\{\phi\}(k)$ for each individual ϕ and k from a *linear* eigenvalue problem, it has to be kept in mind that both the minimization over the wavenumbers and the optimization of the profiles are essentially *nonlinear* operations. The bifurcation in k -space brought about by these nonlinearities entails strong consequences for the optimal upper bound on c_ε . If we take the scaling behaviour of δ for Reynolds numbers below the bifurcation ($\delta \propto Re^{-3/4}$) and set both the slope p and the balance parameter a to their asymptotic values ($p = 0$ and $a = 3$), we can simulate the asymptotic behaviour that *would* prevail if there were no bifurcation. Then (3.16) and (3.54) immediately yield

$$\overline{c_\varepsilon} \sim \text{const.} \times Re^{-1/4}. \quad (3.68)$$

For comparison, the inset in figure 3.8 presents a doubly logarithmic plot of the upper bound in the interval $Re_{ES} \leq Re \leq Re_B$; it also depicts a straight line with the ‘‘asymptotic’’ slope that is predicted by (3.68). The bifurcation takes place before this $Re^{-1/4}$ -behaviour is fully developed, then leading to both the minimum of the upper bound and its actual asymptotic Re^0 -scaling. But interestingly enough, the $Re^{-1/4}$ -dependence of $\overline{c_\varepsilon}(Re)$ is exactly what one finds in Busse’s theory for the case of a single boundary layer approximation (i.e. for a single- α solution; see Busse 1970, 1978 and Kerswell 1997), whereas the Re^0 -scaling is equal to the scaling behaviour of Busse’s asymptotic solution (3.8).

3.7 Discussion and outlook

After the pioneering works by Doering & Constantin (1992, 1994) and the following developments by Nicodemus, Grossmann & Holthaus (1997a) (see chapter 2 of this thesis) and Kerswell (1997) had already established the background flow method as a theoretical tool for computing rigorous upper bounds on quantities that characterize turbulent flows, the techniques developed in this chapter constitute a constructive approach towards the actual solution of this method’s variational principle. This approach is quite different from, and complementary to, the work of Kerswell (1997): there the variational problem was transformed into a nonlinear Euler–Lagrange

type problem. If this problem could be solved exactly, it would give the best bounds that the background flow method can provide. However, an exact solution is exceedingly difficult; up to now only an approximate multi- α solution for asymptotically high Reynolds numbers is available. In contrast, we have divided the problem of calculating upper bounds into pieces that can be dealt with more easily, and deduce rigorous bounds for *any* value of Re , not only for $Re \rightarrow \infty$. The price we have to pay is that the quality of our bounds depends on the choice of the test profiles. With unfortunate choices we may miss the best possible bound; however, this deficiency can be compensated by experience.

The primary objective of this chapter has been the solution procedure itself, rather than its application to a particular flow. The example problem studied here, a plane Couette flow with suppressed spanwise degrees of freedom, is of considerable interest since it illustrates in condensed form all essential steps that also occur in the analysis of physical problems, such as unrestricted shear flows or Rayleigh–Bénard heat convection.

In particular, the variational computation of upper bounds on energy dissipation rate for the unrestricted, three-dimensional Couette flow directly parallels the simplified case. All characteristic features, from the occurrence of a bifurcation in k -space to the shape of the graph of the optimal upper bound, are met again, even though the corresponding equations are *much* more involved. We report in figure 3.13 our findings for this problem, see chapter 5. This upper bound has been computed with the help of profiles that are parametrized in a more sophisticated manner than the profiles (3.52) considered up to now; the mathematical motivation for this improved parametrization will be given in chapter 4. The upper bound for the unrestricted Couette flow separates from the lower one at

$$Re_{ES} = 82.65014887(1); \quad (3.69)$$

correspondingly, the value of c_ε at the energy stability limit is given by

$$c_\varepsilon(Re_{ES}) = Re_{ES}^{-1} = 0.012099191758(2). \quad (3.70)$$

In the asymptotic limit the bound approaches the constant value

$$\lim_{Re \rightarrow \infty} \overline{c}_\varepsilon(Re) = 0.01087(1), \quad (3.71)$$

which is only minutely above (but within the uncertainty interval of) Busse's result (3.8). Hence, when backed by our techniques the background flow method competes in the asymptotic regime with the best other method known so far, and it is unrivaled in the important regime of intermediate Reynolds numbers.

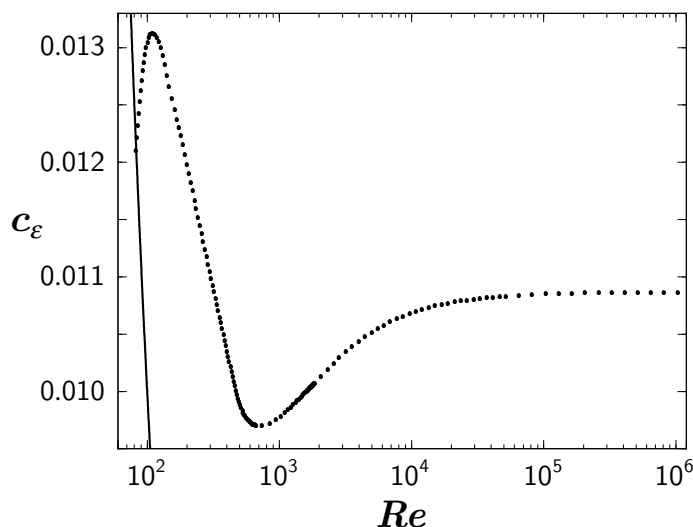


Figure 3.13: Bounds on c_ε for the unrestricted, three-dimensional Couette flow. Points denote the numerically computed variational upper bound $\overline{c}_\varepsilon(Re)$; the solid line on the left is the lower bound $\underline{c}_\varepsilon(Re) = Re^{-1}$.

The most significant step made in the present chapter is the identification of the mechanism that dictates the cross-over from intermediate to high Reynolds numbers and determines the asymptotic scaling behaviour of the optimal upper bounds, namely the bifurcation in k -space displayed in figure 3.12. In the following chapter we will develop an analytical asymptotic theory for our example problem. This will not only result in a detailed understanding of the bifurcation itself and of the scaling behaviour (3.65) of the optimized profile parameters, but also reveal which kind of further parameter is necessary in order to improve the numerically obtained asymptotic value of \overline{c}_ε .

Finally, we summarize in figure 3.14 the present status of research on the rigorous theory of upper bounds on the dimensionless dissipation rate c_ε for the turbulent plane Couette flow, including relevant experimental data for the energy dissipation rate. We recognize that replacing the over-restrictive profile constraint employed in earlier works (Doering & Constantin 1992, 1994; Gebhardt *et al.* 1995; Nicodemus *et al.* 1997a) by the actual spectral constraint (3.13) gives an improvement by about a factor of 8. But the gap that remains between the rigorous upper bounds and the experimentally measured dissipation rates still spans an order of magnitude. Moreover, the question whether the true dissipation rates exhibit a scaling correction in the limit $Re \rightarrow \infty$, perhaps a logarithmic correction as discussed by Doering & Constantin (1994), still remains to be answered.

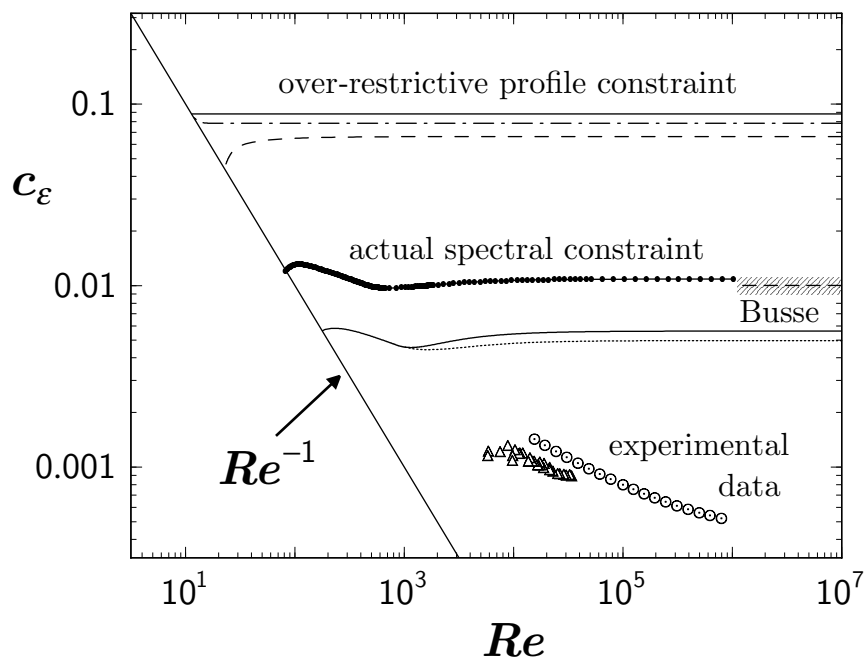


Figure 3.14: Comparison of bounds on $c_\varepsilon(Re)$. — Solid slanted straight line: lower bound $\underline{c}_\varepsilon(Re) = Re^{-1}$. — Topmost horizontal solid line: upper bound obtained by Doering & Constantin (1992, 1994) with the help of an over-restrictive profile constraint and piecewise linear profiles; $\overline{c}_\varepsilon(Re) \approx 0.088$ for $Re > 11.32$. — Dashed-dotted line: improved bound on $c_\varepsilon(Re)$ derived by Gebhardt *et al.* (1995) from the analytical solution of the Doering–Constantin principle with the over-restrictive constraint; $\overline{c}_\varepsilon(Re) \approx 0.079$ for $Re > 16.98$. — Long-dashed line: further improvement due to the introduction of the balance parameter, see chapter 2; $\overline{c}_\varepsilon(Re) \rightarrow 0.066$. This bound is still calculated analytically utilizing the over-restrictive profile constraint. — Heavy dots: upper bound for the unrestricted, three-dimensional plane Couette flow obtained in chapter 5 from the variational principle (3.12) with the actual spectral constraint (3.13), cf. figure 3.13; $\overline{c}_\varepsilon(Re) \rightarrow 0.01087(1)$. — Following dashed line: asymptotic upper bound (3.8) derived by Busse (1970, 1978); $\overline{c}_\varepsilon(Re) \rightarrow 0.010(1)$. The shaded area denotes the estimated uncertainty of this bound. — Solid line below: upper bound computed in this chapter for the restricted, two-dimensional Couette flow, cf. figure 3.8; $\overline{c}_\varepsilon(Re) \rightarrow 0.56184(1) \times 10^{-2}$. — Dotted line: improvement obtained in chapter 4 by optimizing the shape of the profiles’ boundary segments, see (4.76) and (4.75); $\overline{c}_\varepsilon(Re) \rightarrow 0.4980133(1) \times 10^{-2}$. — Triangles: experimental dissipation rates for the plane Couette flow measured by Reichardt (1959). — Circles: experimental dissipation rates for the Taylor–Couette system with small gap as measured by Lathrop, Fineberg & Swinney (1992).

4 Asymptotic theory of dissipation bounds

4.1 Introduction

The numerical exploration of the extended Doering–Constantin variational principle for computing bounds on the rate of energy dissipation in turbulent shear flow (Doering & Constantin 1994; Nicodemus, Grossmann & Holthaus 1997a, chapter 2 of this thesis), as reported in the preceding chapter, has revealed some fairly systematic features: at a certain Reynolds number the minimizing wavenumbers bifurcate, such that the optimal upper bound on the dissipation rate is determined by both minima simultaneously. Moreover, the optimized parameters of the variational profiles exhibit a simple scaling behaviour. These findings call for an analytical explanation.

In the present chapter we will develop a detailed asymptotic theory for the model problem considered in chapter 3, the plane Couette flow without spanwise degrees of freedom. From the numerical solution of the variational problem for the unrestricted, three-dimensional Couette problem (chapter 5) we know that this model actually captures all relevant facts.

The plan of our analysis is the following: in §2 we study the two minimizing wavenumber branches on the basis of the spectral constraint. The most important technical tools introduced there are two types of *shape functions*, which are no variational profiles themselves, but which contain the essential information about the profiles either in the interior or in the boundary layers. These functions will allow us to show that in the asymptotic regime one of the minimizing wavenumbers is determined *solely* by the shape of the profiles in the interior, the other one *solely* by the shape of the profiles in their boundary layers. We build our arguments mainly on two lemmas, which have been formulated such that the propositions are as mild as possible, but which will be found to have far-reaching implications. Together with a third, more technical lemma which has been banished to the appendix, they will allow us to understand the asymptotics of the two minimizing wavenumbers.

An understanding of the two minimizing wavenumbers, however, does not automatically imply an understanding of the optimal upper bound on the dissipation rate, since the two minima of $R_0\{\phi\}(k)$ might have different values, and it is only the global minimum that matters for the variational principle (see (3.51)). The astonishing observation that both minima actually take on the same value is explained in §3. It will be shown that, besides the characterization of the

profiles by two shape functions, only a certain monotony property is required to prove *both* the locking of the two minima to the same value *and* the *Re*-scaling behaviour of the optimal profile parameters; it will even be possible to express the power law prefactors in terms of the shape functions.

The next step then is to show in §4 that the optimal asymptotic upper bound of the dissipation rate is determined entirely by the behaviour of the variational profiles in the boundary layers, and to formulate a much simpler variational principle for this asymptotic bound. The solution of this new principle will reveal that the best bounds derivable from the extended Doering–Constantin principle can be obtained only if the variational profiles contain a parameter which governs their shape within the boundary layers. This insight will be taken up in §5 in order to compute the upper bound with the help of such a generalized class of test profiles for all Reynolds numbers, resulting in the bound that had already been included in the overview given in figure 3.14.

Finally, we will draw our conclusions in §6.

4.2 The two branches of the bifurcation plot

Let us recall a key result obtained in the numerical solution of the variational principle (3.12) with the spectral constraint (3.13) for the restricted plane Couette flow: for Reynolds numbers above $Re_B \approx 860$ the critical Reynolds number $R_c\{\phi\}$, up to which a given profile ϕ remains an admissible test function, is associated with *two* different wavenumbers k_1 and k_2 . This implies a degeneracy of the eigenvalue problem (3.13): two eigenvalues pass through zero simultaneously. After optimization over all profiles, one of these two k -branches scales linearly with Re , the other becomes constant. The two branches of minimizing wavenumbers resulting from a particular choice of test profiles have been depicted in figure 3.12, which will be referred to as a *bifurcation plot*. In this section we will pin down the mathematical features that lead to the emergence of the two branches, and thereby obtain analytical insight into the structure of the eigenvalue problem posed by the spectral constraint.

The starting point of our analysis is the boundary value problem (3.56)–(3.61) for the six-vector $\mathbf{y}(z)$, which arises in the reformulation of the spectral constraint:

$$y'_1 = 2k[-y_1 + y_2], \quad (4.1)$$

$$y'_2 = 2k\left[\frac{1}{2}y_1 - y_2 + \frac{1}{2}y_4\right], \quad (4.2)$$

$$y'_3 = -2ky_3 - \frac{R}{k}\phi'y_1, \quad (4.3)$$

$$y'_4 = 2k[-y_4 + y_5], \quad (4.4)$$

$$y'_5 = 2k\left[\frac{1}{4}y_1 + \frac{1}{2}y_4 - y_5 + \frac{1}{4}y_6\right], \quad (4.5)$$

$$y_6' = 2k[y_2 - y_6] + \frac{R}{2k}\phi'y_3 \quad (4.6)$$

with initial condition

$$\mathbf{y}(0) = (0, 0, 0, 0, 0, 1)^T \quad (4.7)$$

and boundary condition

$$y_1(1) = 0. \quad (4.8)$$

R is the rescaled Reynolds number, see (3.14), $k > 0$ the absolute value of the wavenumber pertaining to the x -direction, and $\phi(z)$ is some profile function. We will denote these quantities as the *input* to the system (4.1)–(4.6). The equivalence of this boundary value problem to the spectral constraint (3.13) has been established in §§ 3 and 5 of chapter 3. Our goal here is to elucidate how the magnitude of the wavenumber k determines the sensitivity of this problem to the shape of the profiles ϕ . Namely, if we have profiles with boundary segments of thickness δ , see (3.52) for a specific example, and if we keep k fixed while letting δ tend to zero, then the above boundary value problem becomes sensitive *solely* to the shape of the profiles in the interior, whereas it is *solely* the shape of the boundary segments that becomes essential if we take k proportional to δ^{-1} while δ approaches zero.

Thus, in the following we consider quite general families of profile functions ϕ_δ parametrized by the width δ of their boundary segments, $0 < \delta < \frac{1}{2}$. Each profile can be divided into three parts, corresponding to the intervals $0 \leq z \leq \delta$ (“left boundary layer”), $\delta \leq z \leq 1 - \delta$ (“interior”) and $1 - \delta \leq z \leq 1$ (“right boundary layer”). Rather than focussing directly on the Reynolds number, we use δ as the control parameter. The limit of interest is $\delta \rightarrow 0$; different powers of $1/\delta$ characterize different orders of magnitude.

4.2.1 The lower branch

If the wavenumber k entering the problem (4.1)–(4.6) is kept (almost) fixed while the profiles, and hence δ , are varied, we have

$$k = O(\delta^0) \quad \text{and} \quad k^{-1} = O(\delta^0). \quad (4.9)$$

It will be useful to introduce functions $\psi(z)$ which, although they are no variational profiles themselves, contain information about the shape of the actual profile functions $\phi(z)$. The purpose of these functions will become clear from the following lemma:

Lemma 4.2.1 *Let $\psi(z)$ be some continuously differentiable function defined in the interval $[0, 1]$ which satisfies the equation*

$$\psi'\left(\frac{1}{2}\right) = 1, \quad (4.10)$$

and let R_ψ be a positive constant. In addition, let $\phi_\delta(z)$ be a family of continuously differentiable functions defined in $[0, 1]$ which are parametrized by δ , $0 < \delta < \frac{1}{2}$, and also depend continuously on some additional parameter $p_\delta > 0$. Assume further that the following properties hold:

i.) ϕ_δ and p_δ depend continuously on the parameter δ ;

ii.) for each δ the function ϕ_δ in the interior is determined by ψ according to

$$\phi'_\delta(z) = p_\delta \psi'(z) \quad \text{for } \delta < z < 1 - \delta; \quad (4.11)$$

iii.) within the boundary layers, i.e. for $0 \leq z \leq \delta$ and $1 - \delta \leq z \leq 1$, one has

$$\phi'_\delta(z) = p_\delta \times O\left(\delta^{-5/2}\right). \quad (4.12)$$

Then it follows that the first component of the solution vector \mathbf{y}_ψ originating from the initial value problem (4.1)–(4.7) with input quantities k , $R = R_\psi$, and $\phi(z) = \psi(z)$ differs from the first component of the solution vector \mathbf{y}_δ corresponding to the input k , $R = R_\psi/p_\delta$, and $\phi(z) = \phi_\delta(z)$ in the entire interval $[0, 1]$ at most by an amount of order $O(\delta)$,

$$y_{\delta,1}(z) = y_{\psi,1}(z) + O(\delta). \quad (4.13)$$

Proof. The verification of this lemma is straightforward but tedious. After rewriting the initial value problem (4.1)–(4.7) as an equivalent vector integral equation, one can make in each of the three regimes $0 \leq z \leq \delta$, $\delta \leq z \leq 1 - \delta$, and $1 - \delta \leq z \leq 1$ an ansatz of the form

$$y_{\delta,i}(z) = y_{\psi,i}(z) + O(\delta^{\alpha_i}), \quad i = 1, \dots, 6.$$

Employing the properties (4.9), (4.11), and (4.12), one can fix the exponents α_i and show by means of integral estimates that one indeed has obtained a solution within each interval. Gluing the three parts of the solution together, one finds a solution in the entire interval $[0, 1]$ which satisfies (4.13). The statement then follows from the fact that the solution to the initial value problem is unique. \square

Note the spirit of this lemma: the reference function $\psi(z)$ is no profile, since it does not have to satisfy the profiles' boundary conditions, but it is used nonetheless as an input for the initial value problem. Even though the derivative of $\phi_\delta(z)$ is not related to that of $\psi(z)$ within the boundary layers, the difference of the first components of the corresponding solution vectors

remains small. Because of the normalization (4.10) the parameter p_δ is the slope of ϕ_δ at $z = \frac{1}{2}$. Thus, p_δ can be considered as a generalization of the parameter p employed previously in (3.52).

In order to make the lemma work we now introduce *shape functions for the interior*, i.e. functions $\psi_{int}(z)$ which are continuously differentiable in $[0, 1]$, fulfill the requirement

$$\psi'_{int}\left(\frac{1}{2}\right) = 1 \quad (4.14)$$

and the additional symmetry condition

$$\psi'_{int}(z) = \psi'_{int}(1 - z). \quad (4.15)$$

We then take a fixed k together with ψ_{int} as input to the system (4.1)–(4.6), and set R_ψ to the smallest positive R -value for which the boundary value problem (4.1)–(4.8) is satisfied,

$$R_\psi = R_0\{\psi_{int}\}(k), \quad (4.16)$$

generalizing the notation introduced in §3 of chapter 3. If we now restrict the family $\phi_\delta(z)$ to functions with the properties

$$\phi_\delta(0) = 0, \quad \phi_\delta(1) = 1 \quad \text{and} \quad \phi_\delta(z) = 1 - \phi_\delta(1 - z), \quad (4.17)$$

so that each ϕ_δ becomes a candidate profile for the variational principle, see (3.10)–(3.13), then the statement (4.13) of the lemma, applied in the limit $\delta \rightarrow 0$, immediately asserts

$$\lim_{\delta \rightarrow 0} p_\delta R_0\{\phi_\delta\}(k) = R_0\{\psi_{int}\}(k), \quad (4.18)$$

with p_δ denoting the slope of ϕ_δ at $z = \frac{1}{2}$. Moreover, considering $R_0\{\psi_{int}\}(k)$ as a function of the wavenumber k , this function will exhibit a global minimum for some $k > 0$. By construction, the minimizing wavenumber does not depend on the boundary layer thickness δ , and therefore is of the required order $O(\delta^0)$. The equation (4.18) thus states that for sufficiently small δ the minima corresponding to the actual profiles ϕ_δ can be understood in terms of a shape function that specifies the profiles in the interior only.

Hence, for families of profiles ϕ_δ that merely possess the “weak” properties (4.17), (4.11), and (4.12), we have obtained a rather strong statement: *for small δ , and provided k is of the order $O(\delta^0)$, the k -dependencies of $R_0\{\phi_\delta\}(k)$ are mirror images of the k -dependence of $R_0\{\psi_{int}\}(k)$, where the function $\psi_{int}(z)$ contains the information about the shape of the profiles ϕ_δ in the*

interior. This implies that for small δ the behaviour of the profiles within the boundary layers plays no role, if k is kept constant.

Focussing now on the minima

$$R_1\{\phi_\delta\} \equiv \min_{k=O(\delta^0)} \{R_0\{\phi_\delta\}(k)\}, \quad (4.19)$$

we obtain from (4.18) that

$$\lim_{\delta \rightarrow 0} p_\delta R_1\{\phi_\delta\} = R_c\{\psi_{int}\} \quad (4.20)$$

with

$$R_c\{\psi_{int}\} \equiv \min_{k>0} \{R_0\{\psi_{int}\}(k)\}, \quad (4.21)$$

again generalizing the notation used in §3 of chapter 3, see (3.51). The minimizing k will be denoted as $k_c\{\psi_{int}\}$.

We can harvest the first fruits of this abstract reasoning when we apply these arguments to the profile functions (3.52), which have been employed for the numerical analysis in chapter 3 of this thesis. Here the parameter p_δ equals the previous p , and a corresponding shape function for the interior — uniquely determined up to a constant — is just the laminar profile,

$$\psi_{int}(z) = z. \quad (4.22)$$

If we take the scaling properties (3.65),

$$\delta \sim \alpha Re^{-1}, \quad p \sim \beta Re^{-1},$$

for δ and p for granted — this gap will be closed later — then we have within the two boundary layers

$$p^{-1}\phi'(z) = O(\delta^{-1}) \left[p + O(\delta^{-1}) \right] = O(\delta^{-2}). \quad (4.23)$$

Thus, with $R_\psi = R_0\{\psi_{int}(z) = z\}(k)$ and $p_\delta = p$ the condition (4.12) of the lemma is satisfied, so that we now understand why the lower k -branch depicted in figure 3.12, denoted as k_1 , approaches for $Re \rightarrow \infty$ the very same k -value that also characterizes the energy stability limit Re_{ES} : since the laminar profile serves as a shape function in the limit of high Reynolds numbers,

so that the ensuing high- Re -minima pertaining to k_1 are replicas of the minima at the energy stability limit, we have the exact identity

$$\lim_{Re \rightarrow \infty} \frac{k_1}{2\pi} = \lim_{\delta \rightarrow 0} \frac{k_1}{2\pi} = \frac{k_c \{\psi_{int}(z) = z\}}{2\pi} = \frac{k_{ES}}{2\pi} = 0.6026776(1). \quad (4.24)$$

4.2.2 The upper branch

In order to carry through an analogous discussion also for the upper k -branch appearing in the bifurcation plot, we now consider values of k that vary proportionally to δ^{-1} , and rewrite the boundary value problem (4.1)–(4.8) by introducing the new rescaled quantities

$$\kappa \equiv 2\delta k \quad \text{and} \quad \rho \equiv 2\delta R, \quad (4.25)$$

together with the rescaled independent variable

$$\xi \equiv z/(2\delta). \quad (4.26)$$

Then the rescaled wavenumber κ becomes independent of δ , i.e. $\kappa = \text{const.}$ or

$$\kappa = O(\delta^0) \quad \text{and} \quad \kappa^{-1} = O(\delta^0). \quad (4.27)$$

Defining

$$\tilde{\mathbf{y}}(\xi) \equiv \mathbf{y}(z) \quad \text{and} \quad \tilde{\phi}(\xi) \equiv \phi(z), \quad (4.28)$$

the boundary value problem can be expressed in terms of the new quantities:

$$\tilde{y}'_1 = 2\kappa [-\tilde{y}_1 + \tilde{y}_2], \quad (4.29)$$

$$\tilde{y}'_2 = 2\kappa \left[\frac{1}{2}\tilde{y}_1 - \tilde{y}_2 + \frac{1}{2}\tilde{y}_4 \right], \quad (4.30)$$

$$\tilde{y}'_3 = -2\kappa\tilde{y}_3 - \frac{\rho}{\kappa} \tilde{\phi}'\tilde{y}_1, \quad (4.31)$$

$$\tilde{y}'_4 = 2\kappa [-\tilde{y}_4 + \tilde{y}_5], \quad (4.32)$$

$$\tilde{y}'_5 = 2\kappa \left[\frac{1}{4}\tilde{y}_1 + \frac{1}{2}\tilde{y}_4 - \tilde{y}_5 + \frac{1}{4}\tilde{y}_6 \right], \quad (4.33)$$

$$\tilde{y}'_6 = 2\kappa [\tilde{y}_2 - \tilde{y}_6] + \frac{\rho}{2\kappa} \tilde{\phi}'\tilde{y}_3; \quad (4.34)$$

the initial condition is

$$\tilde{\mathbf{y}}(0) = (0, 0, 0, 0, 0, 1)^T, \quad (4.35)$$

and the boundary condition reads

$$\tilde{y}_1(1/(2\delta)) = 0. \quad (4.36)$$

Obviously, the form of the system of differential equations (4.1)–(4.6) remains invariant under this transformation. Note, however, that the thickness of the boundary layers, originally characterized by δ , acquires the constant value $\frac{1}{2}$, so that now we have to distinguish the three regimes $0 \leq \xi \leq \frac{1}{2}$ (left boundary layer), $\frac{1}{2} \leq \xi \leq 1/(2\delta) - \frac{1}{2}$ (interior) and $1/(2\delta) - \frac{1}{2} \leq \xi \leq 1/(2\delta)$ (right boundary layer).

Again we formulate a lemma which later on will relate profiles to shape functions:

Lemma 4.2.2 *Let $\psi(\xi)$ be some continuously differentiable function which is defined piecewise in the interval $[0, 1/(2\delta)]$ (with $0 < \delta < \frac{1}{2}$),*

$$\psi(\xi) = \begin{cases} \psi_{bl1}(\xi) & \text{for } 0 \leq \xi \leq \frac{1}{2} \\ C & \text{for } \frac{1}{2} < \xi < 1/(2\delta) - \frac{1}{2} \\ \psi_{bl2}(\xi) & \text{for } 1/(2\delta) - \frac{1}{2} \leq \xi \leq 1/(2\delta) \end{cases}, \quad (4.37)$$

where C is a constant, and let ρ_ψ be a positive constant. In addition, let $\tilde{\phi}_\delta(\xi)$ be a family of continuously differentiable functions defined in $[0, 1/(2\delta)]$, equipped with the following properties:

- i.) $\tilde{\phi}_\delta$ depends continuously on the parameter δ ;
- ii.) for each δ the shape of the boundary segments of the functions $\tilde{\phi}_\delta$ is determined by the boundary segments ψ_{bl1} and ψ_{bl2} of ψ ,

$$\tilde{\phi}'_\delta(\xi) = \begin{cases} \psi'_{bl1}(\xi) + O(\delta) & \text{for } 0 \leq \xi \leq \frac{1}{2} \\ O(\delta^2) & \text{for } \frac{1}{2} < \xi < 1/(2\delta) - \frac{1}{2} \\ \psi'_{bl2}(\xi) + O(\delta) & \text{for } 1/(2\delta) - \frac{1}{2} \leq \xi \leq 1/(2\delta) \end{cases}. \quad (4.38)$$

Then it follows that each component of the solution vector $\tilde{\mathbf{y}}_\psi$ originating from the initial value problem (4.29)–(4.35) with input quantities κ , $\rho = \rho_\psi$, and $\tilde{\phi}(\xi) = \psi(\xi)$ differs from the corresponding component of the solution vector $\tilde{\mathbf{y}}_\delta$ resulting from the input κ , ρ_ψ , and $\tilde{\phi}(\xi) = \tilde{\phi}_\delta(\xi)$ in the entire interval $[0, 1/(2\delta)]$ at most by an amount of order $O(\delta)$,

$$\tilde{\mathbf{y}}_\delta(\xi) = \tilde{\mathbf{y}}_\psi(\xi) + O(\delta). \quad (4.39)$$

Proof. Within the boundary layers $0 \leq \xi \leq \frac{1}{2}$ and $1/(2\delta) - \frac{1}{2} \leq \xi \leq 1/(2\delta)$ we can carry through the proof in a manner analogous to the proof of lemma 4.2.1. But in the interior regime

$\frac{1}{2} \leq \xi \leq 1/(2\delta) - \frac{1}{2}$ this line of reasoning does not work: inserting the ansatz

$$\tilde{\mathbf{y}}_\delta(\xi) = \tilde{\mathbf{y}}_\psi(\xi) + O(\delta) \quad \text{for } \frac{1}{2} \leq \xi \leq 1/(2\delta) - \frac{1}{2}$$

with initial condition

$$\tilde{\mathbf{y}}_\delta\left(\frac{1}{2}\right) = \tilde{\mathbf{y}}_\psi\left(\frac{1}{2}\right) + O(\delta) \tag{4.40}$$

into the integral equation

$$\tilde{\mathbf{y}}_\delta(\xi) = \tilde{\mathbf{y}}_\delta\left(\frac{1}{2}\right) + \int_{1/2}^{\xi} dt A_\delta(t) \tilde{\mathbf{y}}_\delta(t),$$

where

$$A_\delta(\xi) \equiv \begin{pmatrix} -2\kappa & 2\kappa & 0 & 0 & 0 & 0 \\ \kappa & -2\kappa & 0 & \kappa & 0 & 0 \\ -(\rho_\psi/\kappa)\tilde{\phi}'_\delta(\xi) & 0 & -2\kappa & 0 & 0 & 0 \\ 0 & 0 & 0 & -2\kappa & 2\kappa & 0 \\ \frac{1}{2}\kappa & 0 & 0 & \kappa & -2\kappa & \frac{1}{2}\kappa \\ 0 & 2\kappa & \frac{1}{2}(\rho_\psi/\kappa)\tilde{\phi}'_\delta(\xi) & 0 & 0 & -2\kappa \end{pmatrix},$$

— this integral equation is equivalent to the initial value problem (4.29)–(4.34) with initial condition (4.40) — one obtains merely the useless equation

$$\tilde{\mathbf{y}}_\psi(\xi) + O(\delta) = \tilde{\mathbf{y}}_\psi(\xi) + O(\delta^0).$$

We thus need a sharper argument, which will be elaborated in the following.

Introducing an auxiliary perturbation parameter ϵ , we write

$$\tilde{\mathbf{y}}'_\delta(\xi) = \left[2\kappa A_0 + \epsilon \frac{\rho_\psi}{\kappa} \tilde{\phi}'_\delta(\xi) A_1 \right] \tilde{\mathbf{y}}_\delta(\xi) \quad \text{for } \frac{1}{2} \leq \xi \leq 1/(2\delta) - \frac{1}{2}$$

with initial condition (4.40), where A_0 and A_1 are matrices with constant coefficients defined by

$$A_0 \equiv \begin{pmatrix} -1 & 1 & 0 & 0 & 0 & 0 \\ \frac{1}{2} & -1 & 0 & \frac{1}{2} & 0 & 0 \\ 0 & 0 & -1 & 0 & 0 & 0 \\ 0 & 0 & 0 & -1 & 1 & 0 \\ \frac{1}{4} & 0 & 0 & \frac{1}{2} & -1 & \frac{1}{4} \\ 0 & 1 & 0 & 0 & 0 & -1 \end{pmatrix} \quad (4.41)$$

and

$$A_1 \equiv \begin{pmatrix} 0 & 0 & 0 & 0 & 0 & 0 \\ 0 & 0 & 0 & 0 & 0 & 0 \\ -1 & 0 & 0 & 0 & 0 & 0 \\ 0 & 0 & 0 & 0 & 0 & 0 \\ 0 & 0 & 0 & 0 & 0 & 0 \\ 0 & 0 & \frac{1}{2} & 0 & 0 & 0 \end{pmatrix},$$

respectively. For $\epsilon = 1$ this initial value problem is the one to be studied, (4.29)–(4.34) with (4.40). Using the ansatz

$$\tilde{\mathbf{y}}_\delta(\xi) = \sum_{n=0}^{\infty} \epsilon^n \tilde{\mathbf{y}}_{\delta,n}(\xi); \quad \tilde{\mathbf{y}}_{\delta,0}\left(\frac{1}{2}\right) = \tilde{\mathbf{y}}_\delta\left(\frac{1}{2}\right), \quad \tilde{\mathbf{y}}_{\delta,n}\left(\frac{1}{2}\right) = 0 \quad \text{for } n \geq 1,$$

we solve this problem order by order in the perturbation parameter ϵ . The order $O(\epsilon^0)$ produces the problem

$$\tilde{\mathbf{y}}'_{\delta,0}(\xi) = 2\kappa A_0 \tilde{\mathbf{y}}_{\delta,0}(\xi), \quad \tilde{\mathbf{y}}_{\delta,0}\left(\frac{1}{2}\right) = \tilde{\mathbf{y}}_\delta\left(\frac{1}{2}\right),$$

the solution of which is given by

$$\begin{aligned} \tilde{\mathbf{y}}_{\delta,0}(\xi) &= e^{2\kappa A_0(\xi - \frac{1}{2})} \tilde{\mathbf{y}}_\delta\left(\frac{1}{2}\right) = e^{2\kappa A_0(\xi - \frac{1}{2})} \left[\tilde{\mathbf{y}}_\psi\left(\frac{1}{2}\right) + O(\delta) \right] \\ &= \tilde{\mathbf{y}}_\psi(\xi) + e^{2\kappa A_0(\xi - \frac{1}{2})} \times O(\delta). \end{aligned}$$

Because the largest eigenvalue of A_0 is zero, cf. appendix A.1, we have for $\xi \geq \frac{1}{2}$

$$e^{2\kappa A_0(\xi - \frac{1}{2})} = O(\delta^0),$$

and we find

$$\tilde{\mathbf{y}}_{\delta,0}(\xi) = \tilde{\mathbf{y}}_{\psi}(\xi) + O(\delta) \quad \text{for} \quad \frac{1}{2} \leq \xi \leq 1/(2\delta) - \frac{1}{2}. \quad (4.42)$$

For $n \geq 1$ the ϵ -expansion yields

$$\tilde{\mathbf{y}}'_{\delta,n}(\xi) = 2\kappa A_0 \tilde{\mathbf{y}}_{\delta,n}(\xi) + \frac{\rho_{\psi}}{\kappa} \tilde{\phi}'_{\delta}(\xi) A_1 \tilde{\mathbf{y}}_{\delta,n-1}(\xi), \quad \tilde{\mathbf{y}}_{\delta,n}\left(\frac{1}{2}\right) = 0.$$

With the help of the solution

$$\tilde{\mathbf{y}}_{\delta,n}(\xi) = \frac{\rho_{\psi}}{\kappa} \int_{1/2}^{\xi} dt e^{2\kappa A_0(\xi-t)} \tilde{\phi}'_{\delta}(t) A_1 \tilde{\mathbf{y}}_{\delta,n-1}(t)$$

we conclude via complete induction

$$\tilde{\mathbf{y}}_{\delta,n}(\xi) = O(\delta^n) \quad \text{for} \quad \frac{1}{2} \leq \xi \leq 1/(2\delta) - \frac{1}{2}. \quad (4.43)$$

Thus, for $\epsilon = 1$ one obtains from (4.42) and (4.43)

$$\tilde{\mathbf{y}}_{\delta}(\xi) = \tilde{\mathbf{y}}_{\psi}(\xi) + O(\delta) + \sum_{n=1}^{\infty} O(\delta^n) = \tilde{\mathbf{y}}_{\psi}(\xi) + O(\delta) \quad \text{for} \quad \frac{1}{2} \leq \xi \leq 1/(2\delta) - \frac{1}{2}.$$

□

In order to exploit this lemma 4.2.2 for the high- Re -analysis of the eigenvalue problem (4.1)–(4.8), we now introduce in analogy to the previous shape functions $\psi_{int}(z)$ for the interior the *shape functions for the boundary layers* $\psi_{bl}(\xi)$ as continuously differentiable functions defined in the interval $[0, 1]$ that satisfy the boundary and symmetry conditions

$$\psi_{bl}(0) = 0, \quad \psi_{bl}(1) = 1 \quad \text{and} \quad \psi_{bl}(\xi) = 1 - \psi_{bl}(1 - \xi), \quad (4.44)$$

and have vanishing slope at $\xi = \frac{1}{2}$,

$$\psi'_{bl}\left(\frac{1}{2}\right) = 0. \quad (4.45)$$

In addition, we consider for each given ψ_{bl} the function

$$\psi(\xi) \equiv \begin{cases} \psi_{bl}(\xi) & \text{for } 0 \leq \xi \leq \frac{1}{2} \\ \frac{1}{2} & \text{for } \frac{1}{2} < \xi < 1/(2\delta) - \frac{1}{2} \\ \psi_{bl}(\xi - (1/(2\delta) - 1)) & \text{for } 1/(2\delta) - \frac{1}{2} \leq \xi \leq 1/(2\delta) \end{cases}. \quad (4.46)$$

This ψ is a (symmetric) example of the function appearing in lemma 4.2.2, see (4.37). If one cuts out the interior part where ψ is constant and connects the two remaining boundary segments, one recovers the shape functions ψ_{bl} . Note that these shape functions do not depend on the parameter δ , just as the previous shape functions ψ_{int} do not depend on the parameter p_δ .

As in the application of lemma 4.2.1, we consider families of functions $\phi_\delta(z)$ which satisfy (4.17), so that each ϕ_δ is a candidate profile for the variational principle, but now we require that each member of the family inherits its shape within the boundary layers from ψ_{bl} :

$$\phi'_\delta(z) = \begin{cases} \psi'_{bl}(z/(2\delta))/(2\delta) + O(\delta^0) & \text{for } 0 \leq z \leq \delta \\ O(\delta) & \text{for } \delta < z \leq \frac{1}{2} \end{cases}. \quad (4.47)$$

For preassigned rescaled wavenumber κ , we set for each δ the parameter ρ_ψ required in lemma 4.2.2 to the smallest positive ρ -value for which the boundary value problem (4.29)–(4.36) with $\tilde{\phi}(\xi) = \psi(\xi)$ as input can be solved. In accordance with our previous notation, we denote this value as $\rho_0\{\psi\}(\kappa)$. Then (4.39) yields the assertion

$$\lim_{\delta \rightarrow 0} 2\delta R_0\{\phi_\delta\}(\kappa/(2\delta)) = \lim_{\delta \rightarrow 0} \rho_0\{\psi\}(\kappa), \quad (4.48)$$

so that we can relate the critical rescaled Reynolds numbers pertaining to the actual profiles to a functional which contains information about the profiles in the boundary layers only. Comparing (4.48) to (4.18), a major technical difference between these two equations becomes obvious: in contrast to (4.18), *both* sides of (4.48) explicitly require that a limit $\delta \rightarrow 0$ be taken. As shown in detail in appendix A.1, the right hand side of (4.48) can be evaluated by recasting the boundary value problem (4.29)–(4.36) for input profiles ψ in the limit of an infinitely extended (rescaled) interior regime into the form of a simpler boundary value problem, which refers only to the right boundary segment of the shape function ψ_{bl} . (Equivalently, one may choose a formulation that refers only to the left boundary segment of ψ_{bl} .)

This reduced boundary value problem consists of the system (4.29)–(4.34), considered in the interval $[\frac{1}{2}, 1]$, with initial condition

$$\tilde{\mathbf{y}}\left(\frac{1}{2}\right) = (1, 1, 0, 1, 1, 1)^T \quad (4.49)$$

and boundary condition

$$\tilde{y}_1(1) = 0. \quad (4.50)$$

Denoting the smallest positive ρ -value for which this boundary value problem is solved with κ and ψ_{bl} as input as $\sigma_0\{\psi_{bl}\}(\kappa)$, the main result obtained in appendix A.1, see (A.18), can be expressed in the form

$$\lim_{\delta \rightarrow 0} \rho_0\{\psi\}(\kappa) = \sigma_0\{\psi_{bl}\}(\kappa).$$

The possibility of reducing the boundary value problem in this manner hinges mainly on two points. The first point is that if we have a function ψ , which is constant in the interior, as an input for the system (4.29)–(4.34), then these equations can be integrated analytically in the interior. If one approaches the limit $\delta \rightarrow 0$, the interior range becomes so long that it is only the eigenvector corresponding to the largest (non-degenerate) eigenvalue of the coefficient matrix that determines the solution at the connection point to the right boundary layer. Consequently, the initial conditions (4.49) have been chosen proportional to this eigenvector. Now a further important detail can be clarified: the original system of differential equations (3.43)–(3.48) derived directly from the restricted Couette problem had been transformed in §5 of chapter 3 with a common exponential factor e^{-2kz} , resulting in the system (4.1)–(4.6) considered here. *The guiding principle behind this transformation was to ensure that the largest eigenvalue of the coefficient matrix that emerges when the profile function is replaced by a constant is equal to zero.* Each damping constant not equal to $2k$ would have produced a non-vanishing largest eigenvalue and, in turn, would have made the numerical analysis for high Reynolds numbers exceedingly difficult, if not impossible. This is the reason why our numerical high- Re -analysis based on the system (3.56)–(3.61) worked out so well.

The second point that allows the reduction of the boundary value problem is the symmetry of the physical problem: because the input functions ψ are adapted to this symmetry it is not necessary to investigate the behaviour of the \tilde{y}_1 -component of the solution vector within the interior and the left boundary layer, see appendix A.1.

Our assertion (4.48) therefore now becomes a statement for $R_0\{\phi_\delta\}$ that acquires the form of (4.18),

$$\lim_{\delta \rightarrow 0} 2\delta R_0\{\phi_\delta\}(\kappa/(2\delta)) = \sigma_0\{\psi_{bl}\}(\kappa), \quad (4.51)$$

and we can proceed in close analogy to the previous case. When considering $\sigma_0\{\psi_{bl}\}(\kappa)$ as a function of the rescaled wavenumber κ , we know that this function must have a global minimum

for some $\kappa > 0$; the minimizing κ is manifestly independent of δ and therefore of the required order $O(\delta^0)$. For sufficiently small δ , (4.51) relates this minimum to the minima corresponding to the actual profiles. Hence, for profile families ϕ_δ that merely satisfy (4.17) and (4.47) we have obtained a further far-reaching statement: *for small δ , and provided k is of the order $O(\delta^{-1})$, we can understand the k -dependencies of $R_0\{\phi_\delta\}(k)$ as being mirror images of the k -dependence of $\sigma_0\{\psi_{bl}\}(\kappa)$, where $\kappa = 2\delta k$, and the function ψ_{bl} contains the information about the profiles ϕ_δ in the boundary layers.*

Focussing on the minima of $R_0\{\phi_\delta\}(\kappa/(2\delta))$, the conclusion that parallels (4.20) reads

$$\lim_{\delta \rightarrow 0} 2\delta R_2\{\phi_\delta\} = \sigma_c\{\psi_{bl}\}, \quad (4.52)$$

where

$$R_2\{\phi_\delta\} \equiv \min_{k=O(\delta^{-1})} \{R_0\{\phi_\delta\}(k)\} \quad (4.53)$$

and

$$\sigma_c\{\psi_{bl}\} \equiv \min_{\kappa > 0} \{\sigma_0\{\psi_{bl}\}(\kappa)\}; \quad (4.54)$$

the minimizing κ will be written as $\kappa_c\{\psi_{bl}\}$.

The fruits of these efforts now consist in a first understanding of the upper k -branch appearing in the bifurcation plot, referred to as k_2 , if we take again the scaling properties (3.65) for granted. With

$$\psi_{bl}(\xi) = \begin{cases} 2\xi(1-\xi) & \text{for } 0 \leq \xi \leq \frac{1}{2} \\ 1 - 2\xi(1-\xi) & \text{for } \frac{1}{2} < \xi \leq 1 \end{cases}, \quad (4.55)$$

as boundary layer shape function for the profiles (3.52), we obtain for $0 \leq z \leq \delta$

$$\phi'_\delta(z) = \frac{\psi'_{bl}(z/(2\delta))}{2\delta} + O(\delta^0),$$

whereas for $\delta < z \leq \frac{1}{2}$ we have

$$\phi'_\delta(z) = O(\delta).$$

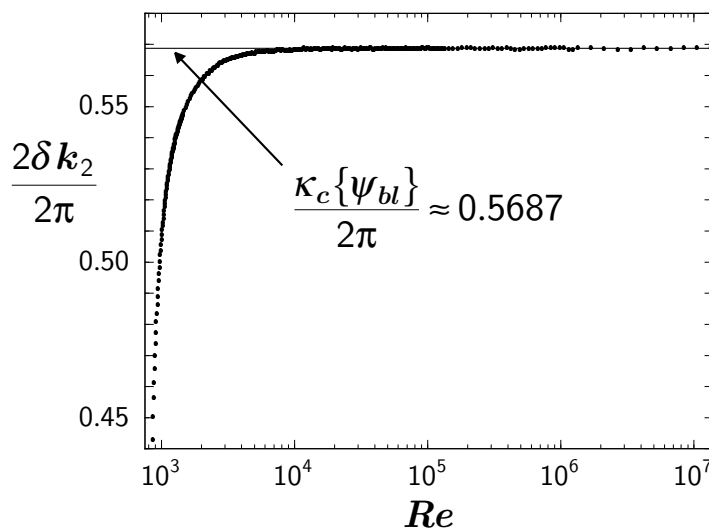


Figure 4.1: Comparison of $2\delta k_2/2\pi$, calculated numerically for the profile class (3.52) as described in §6 of chapter 3 (points), to the constant value (4.58) (solid line, indicated by the arrow). Even though the numerical data result from an intricate minimum search, their scatter is fairly small.

Thus, the condition (4.47) required to deduce (4.52) is satisfied, and we obtain a minimizing k -branch with the asymptotic behaviour

$$\lim_{\delta \rightarrow 0} 2\delta \frac{k}{2\pi} = \frac{\kappa_c\{\psi_{bl}\}}{2\pi}. \quad (4.56)$$

Numerical computations performed with the boundary layer shape function (4.55) yield the values

$$\sigma_c\{\psi_{bl}\} = 400.46929581441(1), \quad (4.57)$$

$$\frac{\kappa_c\{\psi_{bl}\}}{2\pi} = 0.56871956(2). \quad (4.58)$$

(As before, the number in the brackets denotes the uncertainty of the last digit.) In figure 4.1 we compare $2\delta k_2/2\pi$, calculated as a function of the Reynolds number Re from the numerical data reported in §6 of chapter 3, to the constant value (4.58). We see that (4.56) describes the behaviour of k_2 , as resulting from the numerical solution to the variational principle for the profiles (3.52), very well for $Re > 10^4$.

4.3 Scaling solutions to the variational principle

In the preceding section we have studied the equations which embody the spectral constraint (3.13). As a result, we have obtained a very satisfactory understanding of the main consequence that this constraint has for the functions $R_0\{\phi\}(k)$: if the profiles $\phi(z)$ are characterized by two shape functions $\psi_{int}(z)$ and $\psi_{bl}(\xi)$ which fix the profiles for all δ in the interior and in the boundary layers, respectively, and if the Reynolds numbers become large, then $R_0\{\phi\}(k)$ exhibits two distinct minima. But yet we do not understand two further key observations made in the numerical analysis: first, the optimal upper bound on the energy dissipation rate is not determined by an individual minimum, but after optimization both values R_0 , (4.19) and (4.53), turn out to be equal. Second, the numerically found optimal profile parameters δ and p exhibit a pronounced scaling behaviour with Re . In order to understand these findings, we now have to analyse the variational principle itself. In this section we will show that, apart from the characterization of the profiles by two shape functions, only a certain monotony property concerning the dependence of the profiles on the parameters δ and p_δ is needed to prove the scaling (3.65). In addition, it will become clear that the scaling behaviour is intimately connected to the locking of both minima of $R_0\{\phi\}(k)$ to the same value.

Given a shape function $\psi_{int}(z)$ with the properties (4.14) and (4.15), and a shape function $\psi_{bl}(\xi)$ with properties (4.44) and (4.45), we now specify a profile family whose members $\phi_{\delta,p}(z)$ are continuously differentiable with respect to z , and depend continuously on the parameters δ and p , by two requirements:

- i.) each $\phi_{\delta,p}$ obey the boundary conditions and the symmetry condition (4.17), so that each $\phi_{\delta,p}$ is a candidate profile for the variational principle;
- ii.) for each δ and p the derivative of $\phi_{\delta,p}$ be determined by the derivatives of the shape functions ψ_{int} and ψ_{bl} according to

$$\phi'_{\delta,p}(z) = \begin{cases} \psi'_{bl}(z/(2\delta))/(2\delta) + p \times O(\delta^{-1}) & \text{for } 0 \leq z \leq \delta \\ p \psi'_{int}(z) & \text{for } \delta < z < 1 - \delta \\ \psi'_{bl}(1 - (1 - z)/(2\delta))/(2\delta) + p \times O(\delta^{-1}) & \text{for } 1 - \delta \leq z \leq 1 \end{cases} \quad (4.59)$$

In contrast to the preceding section, δ and p are now regarded as independent parameters; the values of p range from zero to an upper bound that may depend on δ .

It can easily be verified that the profiles (3.52) constitute such a family: the corresponding shape functions are given by (4.22) and (4.55). It needs to be stressed that the above specification of the profile family does, by itself, *not* imply any type of relation between the parameters δ and p . The profiles $\phi_{\delta,p}$ have been chosen such that the previous lemmas 4.2.1 and 4.2.2 can be applied, *provided* the propositions (4.12) and (4.47) can be fulfilled, which is *not* guaranteed by the above two requirements i.) and ii.).

We will now determine, within this profile family $\phi_{\delta,p}$, the optimal upper bound on c_ε for given asymptotically large rescaled Reynolds number R . In that case the profile functional

$$D\{\phi_{\delta,p}\} = \int_0^1 dz \left[\phi'_{\delta,p}(z) \right]^2 - 1 \quad (4.60)$$

already encountered in (3.11) takes on large values, as a consequence of the spectral constraint (3.13). Hence, when seeking solutions to the variational principle (3.12) with this constraint, we can expand both the required root of the cubic polynomial (3.21) that yields the corresponding Reynolds number via (3.20), and the right hand side of (3.12), in powers of $D\{\phi_{\delta,p}\}^{-1}$:

$$Re = \frac{2}{3} R \left[1 + \frac{4}{27} D\{\phi_{\delta,p}\}^{-1} + O\left(D\{\phi_{\delta,p}\}^{-2}\right) \right], \quad (4.61)$$

$$\overline{c_\varepsilon} = \frac{27}{16} \frac{D\{\phi_{\delta,p}\}}{R} \left[1 + \frac{8}{9} D\{\phi_{\delta,p}\}^{-1} + O\left(D\{\phi_{\delta,p}\}^{-2}\right) \right], \quad (4.62)$$

where $\overline{c_\varepsilon}$ denotes the upper bound on c_ε given by the expression in curly brackets on the right hand side of (3.12). We conclude: if, for sufficiently large R , the profile function $\phi_{\delta,p}$ that minimizes the profile functional (4.60) has been found, then this same function yields the lowest possible upper bound on the energy dissipation rate at a Reynolds number slightly above the asymptotic value $\frac{2}{3}R$. Whereas $D\{\phi_{\delta,p}\}$ gives only a small correction to $Re = \frac{2}{3}R$, the leading term of the expansion of $\overline{c_\varepsilon}$ is directly proportional to $D\{\phi_{\delta,p}\}$. Thus, *if R is asymptotically large, minimizing the upper bound $\overline{c_\varepsilon}$ is tantamount to minimizing the profile functional $D\{\phi_{\delta,p}\}$ under the spectral constraint.*

The profile functional (4.60) measures the deviation of its argument from the laminar profile; it takes on values ranging from zero (if the argument is equal to the laminar profile) to infinity. We now demand that the deviation of our variational profiles $\phi_{\delta,p}$ from the laminar profile, as measured by $D\{\phi_{\delta,p}\}$, be monotonous in both δ and p . That is, besides by the properties i.) and ii.) listed above, we specify the family $\phi_{\delta,p}$ by a third requirement:

iii.) the dependence of the profiles on δ and p be such that

$$\frac{\partial D\{\phi_{\delta,p}\}}{\partial p} < 0 \quad (\text{for fixed } \delta) \quad (4.63)$$

and

$$\frac{\partial D\{\phi_{\delta,p}\}}{\partial \delta} < 0 \quad (\text{for fixed } p). \quad (4.64)$$

This third specification, which restricts the possible functions ψ_{int} and ψ_{bl} , makes sure that the measure for the deviation from the laminar profile increases if the slope p decreases, or if the extension of the boundary layer decreases. The previous family (3.52) obviously obeys these

monotony conditions, since according to (3.54) the profile functional adopts the form

$$D\{\phi_{\delta,p}\} = \left(\frac{2}{3\delta} - 1\right) (1-p)^2,$$

and we have $0 < \delta \leq \frac{1}{2}$, together with $0 \leq p < 1$.

Since we already know that minimizing the upper bound on c_ε for a given large R means minimizing $D\{\phi_{\delta,p}\}$, the requirements (4.63) and (4.64) imply that the minimal upper bound is attained if both parameters δ and p take on, independently from each other, the largest values that are permitted by the spectral constraint. We denote these values as

$$\delta_R \quad \text{and} \quad p_R.$$

Now we can exploit our knowledge about how the spectral constraint works in the regime of asymptotically large R , i.e. we can utilize the relations (4.20) and (4.52). It must be kept in mind, however, that these relations hold only if the conditions (4.12) and (4.47) are satisfied. We will therefore first *assume* that this is the case, and deduce the ensuing scaling properties of δ_R and p_R . In a second step we will *show* that these scaling properties actually suffice to guarantee that the conditions are fulfilled, so that the argument is self-consistent, and logically sound. This somewhat indirect strategy is the price we have to pay for the detailed statements that we will obtain about the highly nonlinear variational principle.

Assuming that the conditions are satisfied, then (4.20) and (4.52) hold. Since the variational principle forces δ and p to their largest possible values δ_R and p_R , respectively, $R_1\{\phi_{\delta,p}\}$ and $R_2\{\phi_{\delta,p}\}$ take on, independently from each other, the smallest possible values compatible with the spectral constraint. By the very definition of the spectral constraint, the infimum of both $R_1\{\phi_{\delta,p}\}$ and $R_2\{\phi_{\delta,p}\}$ is R itself:

$$R_1\{\phi_{\delta_R,p_R}\} = R_2\{\phi_{\delta_R,p_R}\} = R. \quad (4.65)$$

This is the mechanism that locks the two minima to the same value. Hence, we obtain from (4.20) and (4.52) the asymptotic behaviour of the optimal parameters δ_R and p_R :

$$\delta_R \sim \frac{\sigma_c\{\psi_{bl}\}}{2R}, \quad p_R \sim \frac{R_c\{\psi_{int}\}}{R}. \quad (4.66)$$

To check the consistency of this reasoning we have to insert (4.66) into the profiles (4.59). Since

$$p_R \sim \frac{2R_c\{\psi_{int}\}}{\sigma_c\{\psi_{bl}\}} \delta_R,$$

i.e. $p_R = O(\delta_R)$, we find for $0 \leq z \leq \delta_R$ the estimate

$$\phi'_{\delta_R, p_R}(z) = \frac{\psi'_{bl}(z/(2\delta_R))}{2\delta_R} + p_R \times O(\delta_R^{-1}) = \frac{\psi'_{bl}(z/(2\delta_R))}{2\delta_R} + O(\delta_R^0) = O(\delta_R^{-1});$$

analogously, it is $\phi'_{\delta_R, p_R}(z) = O(\delta_R^{-1})$ for $1 - \delta_R \leq z \leq 1$. On the other hand, for $\delta_R < z < 1 - \delta_R$ we have

$$\phi'_{\delta_R, p_R}(z) = O(\delta_R).$$

Thus, the conditions (4.12) and (4.47) required to guarantee the validity of (4.20) and (4.52) are satisfied.

From now on we write δ and p for the optimized parameters, omitting the subscript R . By virtue of (4.61) the limit $R \rightarrow \infty$ is equivalent to the limit $Re \rightarrow \infty$. Hence, *we have proven a generalization of the numerically found scaling law (3.65):*

$$\delta \sim \alpha Re^{-1}, \quad p \sim \beta Re^{-1};$$

the scaling constants are identified as $\alpha = \frac{1}{3}\sigma_c\{\psi_{bl}\}$ and $\beta = \frac{2}{3}R_c\{\psi_{int}\}$. This type of scaling holds for all profile families that stem from two shape functions and obey the specifications i.), ii.), and iii.), as introduced above. In the limit of large R the constant factor between δ and $1/R$ is determined by the quantity $\sigma_c\{\psi_{bl}\}$, which only depends on the shape function for the boundary layers. In contrast, the constant of proportionality between p and $1/R$ is given by $R_c\{\psi_{int}\}$, depending only on the shape function for the interior. It has to be emphasized that the practical calculation of $R_c\{\psi_{int}\}$ and $\sigma_c\{\psi_{bl}\}$ from their respective eigenvalue problems, followed by a minimization over the (rescaled) wavenumber, is much simpler than solving the full problem for the corresponding high- R -profiles. Moreover, the scaling properties reduce the treatment of the entire asymptotic regime to the solution of the two reduced problems.

To demonstrate the accuracy of our arguments, we resort once again to the profile family (3.52) and compare the analytically derived scaling behaviour (4.66) to the corresponding data obtained in the numerical solution of the variational problem. With $R_c\{\psi_{int}(z) = z\} = Re_{ES}$, see (3.62), and $\sigma_c\{\psi_{bl}\}$ from (4.57) we obtain δ and p as functions of R . In figures 4.2 and 4.3 we show that there is excellent agreement between the numerical data and the asymptotic laws for $R > 2000$. We then can utilize these power laws to derive asymptotic expressions for the optimized profile functional $D\{\phi_{\delta, p}\}$, the Reynolds number Re , and the optimal bound \bar{c}_ε as functions of R , see (4.60)–(4.62). In figure 4.4 we depict this asymptotic bound as a function of Re in comparison with the numerical data, taken from figure 3.8. The asymptotic bound yields a rather good description of the numerical data in the high- Re -regime. Most remarkably, the asymptotic

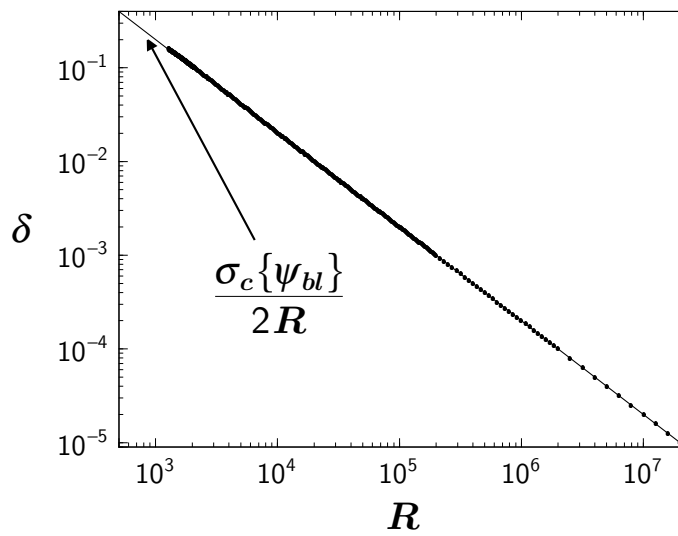


Figure 4.2: Comparison of the optimized parameter δ , as obtained in the numerical solution of the variational principle with the profile family (3.52) for $Re \geq Re_B$ (points; cf. figure 3.10), to the scaling solution (4.66) (solid line, indicated by the arrow).

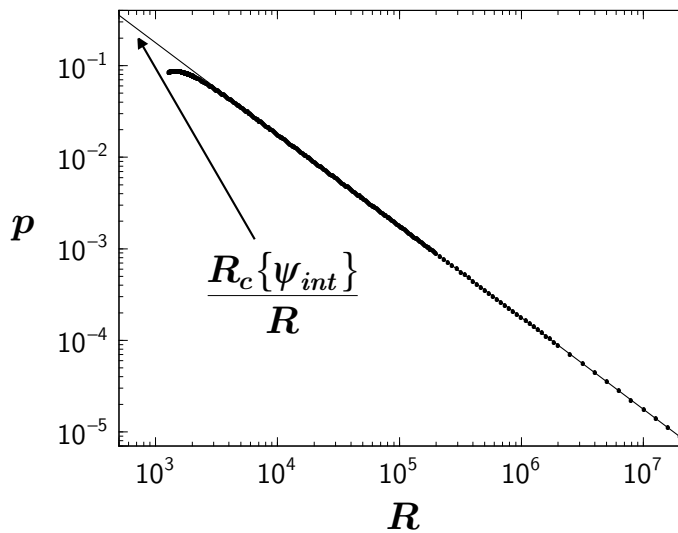


Figure 4.3: Comparison of the optimized parameter p , as obtained in the numerical solution of the variational principle with the profile family (3.52) for $Re \geq Re_B$ (points; cf. figure 3.11), to the scaling solution (4.66) (solid line, indicated by the arrow).

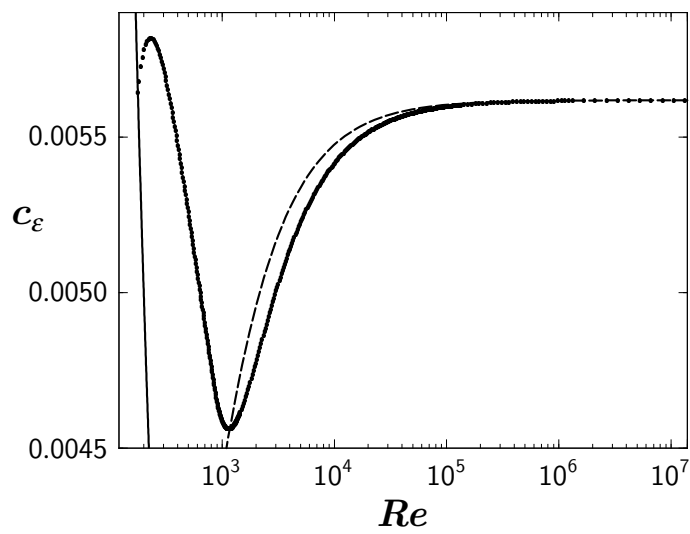


Figure 4.4: Comparison of the asymptotic upper bound on c_ε , as obtained numerically with the profile family (3.52) (points, cf. figure 3.8), to the asymptotic bound resulting from the scaling solution (4.66) (long-dashed line). The solid line at the left shows the lower bound $\underline{c}_\varepsilon(Re) = Re^{-1}$.

bound captures even the ascent of the numerical data from the minimum point to the high- Re -limit, which indicates that *this ascent is part of the asymptotics*.

4.4 Variational principle for the asymptotic boundary layer shape function

In this section we try to obtain the best bound on the energy dissipation rate that the variational principle can provide for infinitely large Reynolds numbers. With the help of lemma 4.2.2 and the statements derived therefrom, we can cast the problem of computing the best asymptotic upper bound on c_ε into the form of a variational principle which refers only to the shape function ψ_{bl} for the boundary layers. Interestingly, we will find that the best possible asymptotic boundary layer shape functions themselves develop new internal boundary layers within their boundary layers.

We start from a profile family $\phi_{\delta,p}(z)$ that obeys the specifications i.), ii.), and iii.) formulated in the preceding section. Applied to this family, the variational principle (3.12, 3.13) yields the scaling solutions (4.66) for the parameters δ and p . Since now we are only interested in the asymptotic value

$$\lim_{Re \rightarrow \infty} \overline{c_\varepsilon}(Re) \equiv \overline{c_\varepsilon^\infty}$$

of the upper bound $\overline{c_\varepsilon}$ on c_ε , we conclude from §2.2 that we may take the limit $p \xrightarrow{Re \rightarrow \infty} 0$ first, and then $\delta \xrightarrow{Re \rightarrow \infty} 0$. That is, we will obtain the correct value of $\overline{c_\varepsilon^\infty}$ if we set

$$p = 0 \tag{4.67}$$

right from the outset, and then take the limit $\delta \rightarrow 0$.

Inserting (4.67) into (4.59) and utilizing (4.44) and (4.17), we arrive at the one-parameter profile family

$$\phi_{\delta,0}(z) = \begin{cases} \psi_{bl}(z/(2\delta)) & \text{for } 0 \leq z \leq \delta \\ \frac{1}{2} & \text{for } \delta < z < 1 - \delta \\ \psi_{bl}(1 - (1 - z)/(2\delta)) & \text{for } 1 - \delta \leq z \leq 1 \end{cases} . \tag{4.68}$$

With $\xi = z/(2\delta)$, as in (4.26), the right hand side of (4.68) equals the function $\psi(\xi)$ defined in (4.46). In order to compute $\overline{c_\varepsilon^\infty}$, we first evaluate the profile functional $D\{\phi_{\delta,0}\}$. Since we have

$\delta = \sigma_c\{\psi_{bl}\}/(2R)$ from (4.66), we find

$$D\{\phi_{\delta,0}\} = \frac{R}{\sigma_c\{\psi_{bl}\}} \int_0^1 d\xi [\psi'_{bl}(\xi)]^2 - 1. \quad (4.69)$$

Then (4.61) and (4.62) yield

$$\overline{c_\varepsilon^\infty} = \frac{27}{16} \frac{I\{\psi_{bl}\}}{\sigma_c\{\psi_{bl}\}}, \quad (4.70)$$

where we have introduced the new functional

$$I\{\psi_{bl}\} \equiv \int_0^1 d\xi [\psi'_{bl}(\xi)]^2. \quad (4.71)$$

Clearly, the asymptotic bound $\overline{c_\varepsilon^\infty}$ depends on the shape of the boundary layers only, as determined by the shape function ψ_{bl} .

In this way we have obtained a rigorous asymptotic upper bound on c_ε for *each* ψ_{bl} that is of the required form. Hence, *the best possible asymptotic upper bound within all families $\phi_{\delta,p}$ is determined by a new variational principle:*

$$\lim_{Re \rightarrow \infty} c_c(Re) \leq \inf_{\psi_{bl}} \left\{ \frac{27}{16} \frac{I\{\psi_{bl}\}}{\sigma_c\{\psi_{bl}\}} \right\}, \quad (4.72)$$

where ψ_{bl} is an arbitrary continuously differentiable function defined on the interval $[0, 1]$ with the properties (4.44) and (4.45), the functional $I\{\psi_{bl}\}$ is given by (4.71), and $\sigma_c\{\psi_{bl}\}$ is defined in (4.54), i.e.

$$\sigma_c\{\psi_{bl}\} = \min_{\kappa > 0} \{\sigma_0\{\psi_{bl}\}(\kappa)\}; \quad (4.73)$$

the eigenvalue $\sigma_0\{\psi_{bl}\}(\kappa)$ has to be determined as the smallest positive ρ -value solving the boundary value problem (4.29)–(4.34), (4.49) and (4.50) with κ and ψ_{bl} as input.

This variational principle is quite similar to the one that results from the original principle (3.12, 3.13) giving the upper bound for arbitrary Reynolds numbers, *after* the optimization of a , which yields (3.18), and the reformulation of the spectral constraint as discussed in §3 of chapter 3 have been taken into account. The main difference is that now the Reynolds number is fixed at infinity, which implies that the degrees of freedom of the admissible profiles are reduced to those of the boundary segments.

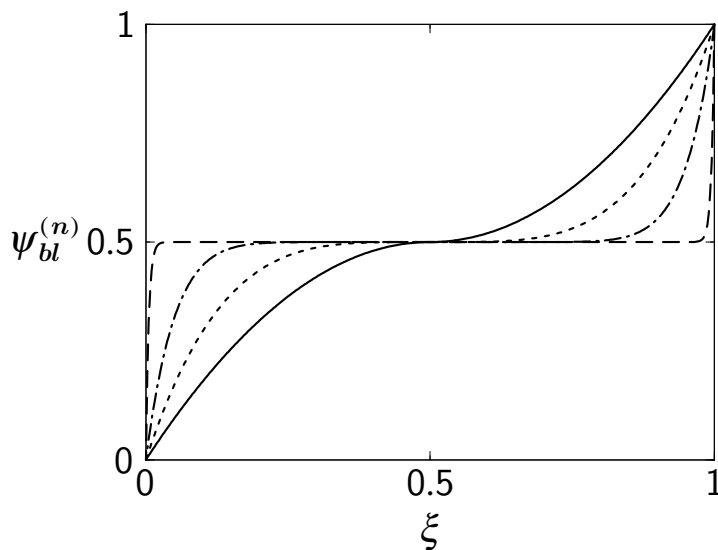


Figure 4.5: Graphs of $\psi_{bl}^{(n)}$ for $n = 2$ (solid line), $n = 4$ (short dashes), $n = 10$ (dash-dotted), and $n = 100$ (long dashes).

The key point is that this new principle (4.72) is *much* simpler than the original principle (3.12, 3.13), evaluated at asymptotically high Re . The new principle can therefore be solved employing profiles with rather complicated boundary segments (described by the boundary layer shape functions ψ_{bl}), even non-analytical ones, which is practically impossible on the level of the original principle. By such an extensive numerical investigation of (4.72), we found that at least a rather good approximation to this principle's solution can be obtained within the following *one-parameter* class of shape functions:

$$\psi_{bl}^{(n)}(\xi) \equiv \begin{cases} \frac{1}{2} - 2^{n-1} \left(\frac{1}{2} - \xi\right)^n & \text{for } 0 \leq \xi \leq \frac{1}{2} \\ \frac{1}{2} + 2^{n-1} \left(\xi - \frac{1}{2}\right)^n & \text{for } \frac{1}{2} < \xi \leq 1 \end{cases}, \quad n \geq 2. \quad (4.74)$$

For each function $\psi_{bl}^{(n)}$, the boundary segments (i.e. the parts of $\psi_{bl}^{(n)}$ defined in $0 \leq \xi \leq \frac{1}{2}$ and $\frac{1}{2} < \xi \leq 1$, respectively) are modeled by polynomials of order n which have the property that the first $n - 1$ derivatives vanish at the matching point $\xi = \frac{1}{2}$. For $n = 2$, in particular, the function $\psi_{bl}^{(2)}$ is identical with the boundary layer shape function (4.55) for the profile family (3.52). In figure 4.5 we show the graphs of $\psi_{bl}^{(n)}$ for some values of n between 2 and 100.

Unexpectedly, the best possible asymptotic upper bound on c_ε within the class (4.74) is given by the limiting shape function $\lim_{n \rightarrow \infty} \psi_{bl}^{(n)}(\xi)$. With increasing n the functions $\psi_{bl}^{(n)}$ develop

n	$\sigma_c \left\{ \psi_{bl}^{(n)} \right\}$	$\overline{c_\epsilon^\infty}^{(n)}$
2	400.46929581441(1)	$0.56184082612983(1) \times 10^{-2}$
3	570.26826714776(1)	$0.53264405105202(1) \times 10^{-2}$
4	740.09950462354(2)	$0.52116544235560(2) \times 10^{-2}$
10	1757.8719829105(2)	$0.5052460607890(1) \times 10^{-2}$
100	17007.03473085(3)	$0.498611288310(1) \times 10^{-2}$
1000	169488.035203(1)	$0.498071787211(2) \times 10^{-2}$
10000	1694296.84184(2)	$0.498019100769(6) \times 10^{-2}$
100000	16942384.78(1)	$0.4980138450(3) \times 10^{-2}$
1000000	169423262(2)	$0.498013326(6) \times 10^{-2}$

Table 4.1: Asymptotic upper bounds on c_ϵ provided by shape functions (4.74) for increasing values of n .

distinct *internal boundary layers within the previous boundary layers*. The widths of these new internal layers can be characterized by the shape functions' inverse slopes at the origin $\xi = 0$,

$$\left[\psi_{bl}^{(n)'}(0) \right]^{-1} = \frac{1}{n}.$$

It needs to be emphasized that it is, nonetheless, the shape of the functions $\psi_{bl}^{(n)}$ in the entire intervals $0 \leq \xi \leq \frac{1}{2}$ and $\frac{1}{2} < \xi \leq 1$ that determines the bound on c_ϵ . If one replaced, for some large n , the internal boundary layers of thickness $1/n$ by the corresponding segments from $\psi_{bl}^{(2)}$, shortened to $1/n$, and then linked these two quadratic segments with a constant piece $\psi(\xi) = \frac{1}{2}$ for $1/n < \xi < 1 - 1/n$, one would merely obtain the same value for the upper bound as $\psi_{bl}^{(2)}$ would have produced itself, *not* the better bound resulting from $\psi_{bl}^{(n)}$.

In table 4.1 we present the numerical values for $\sigma_c \left\{ \psi_{bl}^{(n)} \right\}$ and the resulting asymptotic upper bounds on c_ϵ , denoted as $\overline{c_\epsilon^\infty}^{(n)}$, for increasing values of n . In particular, $\overline{c_\epsilon^\infty}^{(2)}$ equals the previously obtained bound (3.64). Obviously, the data allow us to extract the limit $n \rightarrow \infty$ with considerable accuracy:

$$\lim_{n \rightarrow \infty} \overline{c_\epsilon^\infty}^{(n)} = 0.4980133(1) \times 10^{-2}. \quad (4.75)$$

Thus, the improvement that results from the optimization of the shape of the boundary segments amounts to about 11%.

4.5 Incorporating a variational parameter for the shape of the boundary segments

In this section we will exploit the knowledge gained from the asymptotic analysis in order to improve the numerical results obtained in the preceding chapter of this thesis. Therefore, we now come back to the variational principle (3.12, 3.13), and to the solution technique developed in §§ 3 and 4 of chapter 3. The previous test profiles (3.52), chosen on the grounds of a simple guess, had been characterized merely by the thickness δ of the profiles' boundary segments and by their slope p in the interior. However, the analysis carried through in the preceding section has revealed that in order to find the best high- Re -bound on c_ε that is obtainable from the background flow method one has to resort to test profiles $\phi(z)$ that contain at least one *variational parameter governing the shape of the boundary segments*.

Based on this insight, we now consider an extended class of test profiles:

$$\phi(z) = \begin{cases} \frac{1}{2}(1-p) + pz - \frac{1}{2}(1-p)(1-z/\delta)^n & \text{for } 0 \leq z \leq \delta \\ \frac{1}{2}(1-p) + pz & \text{for } \delta < z < 1 - \delta \\ \frac{1}{2}(1-p) + pz + \frac{1}{2}(1-p)(1 - (1-z)/\delta)^n & \text{for } 1 - \delta \leq z \leq 1 \end{cases} \quad (4.76)$$

This class contains three independent parameters:

- i.) the thickness δ of the boundary segments ($0 < \delta \leq \frac{1}{2}$);
- ii.) the profile slope p in the interior ($0 \leq p \leq 1$);
- iii.) the polynomial order n of the boundary segments ($n = 2, 3, \dots$).

At the matching points, these profiles are $n - 1$ times continuously differentiable. In particular, fixing $n = 2$ leads us back to the previous test profiles (3.52).

The profile functional (3.11), evaluated within the class (4.76), adopts the form

$$D\{\phi\} = \left[\frac{1}{2} \frac{n^2}{(2n-1)\delta} - 1 \right] (1-p)^2.$$

For each individual n the functions $\psi_{int}(z) = z$ and $\psi_{bl}(\xi) = \psi_{bl}^{(n)}(\xi)$ as defined in (4.74) provide shape functions for the test profiles (4.76). Hence, it can easily be seen that for each fixed n these profiles constitute a profile family $\phi_{\delta,p}$ that obeys for $0 \leq p < 1$ the specifications i.), ii.), and iii.) formulated in § 3. For each fixed n we therefore have scaling solutions (4.66); some values of the ensuing asymptotic upper bounds $\overline{c_\varepsilon^\infty}$ have been listed in table 4.1.

In a first step, we now restrict the numerical investigations to families (4.76) with a constant value of the parameter n . For each n we get a variational bound on the energy dissipation

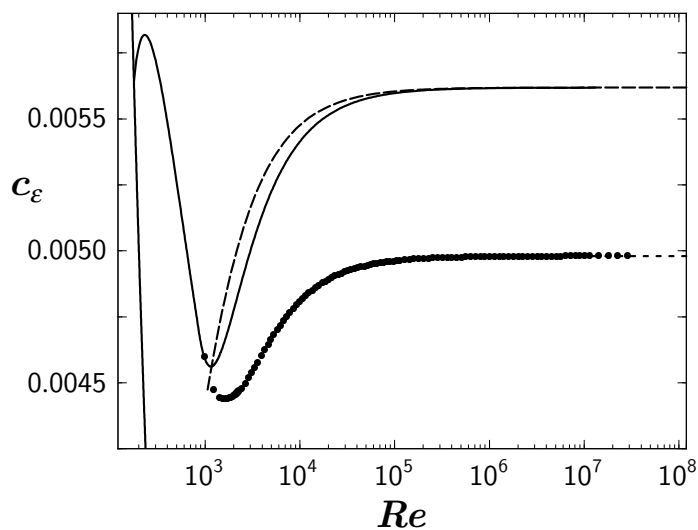


Figure 4.6: Variational bounds on $c_\varepsilon(Re)$. Solid line on the left: lower bound $\underline{c}_\varepsilon(Re) = Re^{-1}$; solid upper line: optimal upper bound provided by the test profiles (3.52), cf. figure 3.8; points: improved upper bound obtained numerically with the help of the new parameter n that determines the shape of the profiles' boundary segments. The long-dashed line is the bound derived from the scaling solutions (4.66) for $n = 2$; the short-dashed line continuing the points indicates the limit (4.75).

rate with the help of the envelope technique described in §4 of chapter 3. It turns out that for each $n > 2$ the graph of the corresponding optimized upper bound on c_ε , referred to as a n -graph in the following, has the same characteristic shape as in the already familiar case $n = 2$, see figure 3.8. With increasing n the global minima of these n -graphs are shifted to higher Re , degenerating to a kink for $n \geq 20$. Moreover, the maximum between the energy stability limit Re_{ES} and the minimum point becomes higher, while the ascend from the minimum to the asymptotic value becomes less pronounced when n is increased. In the limit $n \rightarrow \infty$ the value at the minimum coincides with the asymptotic value.

In a second step we then utilize an envelope technique for selecting from the individual n -graphs the point that each of these graphs contributes to the overall optimal bound obtainable from the variation of all three parameters, δ , p , and n . The result is drawn in figure 4.6. We also have included the upper bound on c_ε computed previously from the profiles (3.52), together with the upper bound derived from the scaling solutions (4.66) for $n = 2$, and the asymptotic bound (4.75) pertaining to the limit $n \rightarrow \infty$.

Although the improvement of the upper bound brought about by the additional variational degree of freedom is not overwhelming — the absolute minimum is shifted to slightly higher values of Re , and the asymptotic value of the bound is lowered by about 11% — it is of considerable mathematical and physical interest to investigate the new scaling behaviour of the optimal profile parameters. We can clearly distinguish three different regimes:

- a.) For Reynolds numbers less than ≈ 975 , the overall optimal upper bound is produced by the previous profile class (3.52), so that in this regime the parameter n remains tied to its smallest value, $n = 2$. Consequently, the bifurcation of the wavenumbers minimizing $R_0\{\phi\}(k)$, which occurs at $Re = Re_B \approx 860$, remains unchanged. The boundary segment thickness δ decreases monotonously with increasing Re from 0.5 to its minimal value ≈ 0.14 .
- b.) In the following regime, for $975 \lesssim Re \lesssim 2280$, we encounter a dramatic change of the shape of the boundary segments: the parameter n increases from 2 to 19, so that the internal boundary segments become steeper, while δ increases back to its maximal possible value 0.5, so that the entire boundary segments reach deeper and deeper into the bulk and finally join together. The steepening within the original boundary layers seems to indicate that the role of these original boundary layers is now taken over by the internal layers. But we reemphasize that the numerical values of the dissipation bound are determined by the shape of the entire boundary segments, not merely by the internal. The bound on c_ε passes in this Re -regime through its minimal value

$$\overline{c_\varepsilon}^{min} \approx 0.44388 \times 10^{-2}.$$

It appears quite remarkable that this regime, where the shift from the original δ -sized layer to the internal boundary layer takes place and the bound passes through a pronounced minimum, coincides with the regime where typical laboratory shear flows become turbulent.

- c.) For Re above ≈ 2280 , we finally obtain simple scaling laws for the profile parameters: δ remains locked to the value 0.5, while n and p scale according to

$$n \sim aRe, \quad p \sim bRe^{-1}$$

in the limit of large Re , with constants a and b . This corresponds to a power-law change of the profile shape: the slope at the boundary $z = 0$ is given by

$$\phi'(0) = p + \frac{n}{2\delta} (1 - p) \sim n \sim aRe,$$

whereas the slope in the middle $z = \frac{1}{2}$ becomes

$$\phi'\left(\frac{1}{2}\right) = p \sim bRe^{-1}.$$

It is tempting to speculate that this power-law change of the shape might be related to fully developed turbulence.

The bound thus derived from the profiles (4.76) had already been included in the overview given in figure 3.14. We now have closed the circle: the numerical investigation of the variational principle performed in chapter 3 had provided the clues for the analysis carried through in the present chapter, which, in turn, has led to the identification of that set of test functions which correctly captures the asymptotics.

4.6 Conclusions: the principles behind the principle

Let us summarize the main results obtained in the preceding chapter 3 and in the present chapter of this thesis. Despite substantial numerical and analytical effort, it has not been possible to lower the value (3.8) of the asymptotic upper bound that the Optimum Theory provides for the rate of energy dissipation in plane Couette flow (Busse 1970, 1978, 1996); Busse's early calculation (Busse 1970) stands out as a singular achievement. In agreement with the results obtained by Kerswell (1997), the asymptotic bound (3.71) derived from the extended Doering–Constantin principle coincides with Busse's number, within the uncertainty of that number.

And yet, the progress made in the present work is quite considerable. Not only is our result (3.71) significant to all digits stated, but also has it been possible for the first time to derive a rigorous upper bound on the dissipation rate that (i) compares favourably in the asymptotic regime with the bound given by the Optimum Theory, (ii) is free from any assumption or uncontrolled approximation whatsoever, and (iii) spans the entire range from the energy stability limit to asymptotically high Reynolds numbers. In particular, we have identified the mechanism that determines the optimal upper bound in the cross-over regime from “low” to “high” Reynolds numbers, namely a bifurcation of the minimizing wavenumbers, and have shown that the best asymptotic bound obtainable from the principle (3.12, 3.13) is approached *from below*. The bound shows a non-trivial structure, that is, a pronounced minimum followed by a *Re*-range between 1000 and 1800 in which the bound's curvature changes its sign. Remarkably, this occurs at about those Reynolds numbers where typical shear flows start to become turbulent. At the moment, the question whether this is just a coincidence or a systematic feature of the background flow method is left to speculation.

The important technical step that has made the numerical solution of the variational principle feasible for almost arbitrary Reynolds numbers is the reformulation of its spectral constraint (3.13) as a boundary value problem, as outlined in §3 of chapter 3. Using this very technique, the extended Doering–Constantin principle can now routinely be applied to other problems of interest, such as channel flow or turbulent convection, which have been considered within the original formulation of the variational principle, and on the level of functional estimates, by Constantin & Doering (1995) and Doering & Constantin (1996).

The analytical insight gained in this chapter stems largely from the idea of the shape functions that specify the variational profiles separately in the interior of the fluid or in the boundary

layers. These shape functions have allowed us to disentangle the sensitivity of the spectral constraint to the profiles' behaviour in the interior from the sensitivity to the behaviour in the boundary layers, and to explain the occurrence of two branches of minimizing wavenumbers quantitatively. The additional observation that the monotony properties (4.63) and (4.64) suffice to guarantee the equilibration of the two minima, and thereby to bring about the numerically observed scaling behaviour of the profile parameters with the Reynolds number, even has some aesthetic appeal. The following deduction of the necessity to endow the variational profiles with a parameter that governs their shape within the boundary layers, and the emergence of new internal boundary layers within the original boundary layers, has completed the picture: with these findings, the principles behind the principle are clear now.

A key result of the analysis of the restricted, two-dimensional Couette problem is the variational principle (4.72) for the bound on the dissipation rate in the limit $Re \rightarrow \infty$. Numerical work indicates that this principle can be solved within the *one-parameter* class (4.74) of boundary layer shape functions ψ_{bl} . Hence, for all classes of variational profiles which can be described by two shape functions according to the specifications i.), ii.), and iii.) formulated in § 3, (4.75) represents the *best possible asymptotic bound* for the restricted Couette problem. This implies that, if one tries to solve the original variational principle (3.12, 3.13) within classes of two-shape-function profiles that are arbitrarily more sophisticated than (4.76), one should be able to improve the bound at finite Re , but *not* in the limit $Re \rightarrow \infty$. We stress that the set of all classes of two-shape-function profiles is fairly large. Our analysis applies to each such class, and it is indeed rather difficult to imagine an asymptotic profile which can not be obtained as the limiting case of profiles from one particular class. We conjecture that the profiles (4.76) yield the optimal asymptotic bound also for the unrestricted, three-dimensional Couette flow, and use in the following chapter this class of test profiles to compute the upper bound \overline{c}_ε (cf. figure 3.13), even though we do not have a formal proof of this conjecture.

5 Variational bound on energy dissipation in the unrestricted, three-dimensional plane Couette flow

5.1 Introduction

In this chapter, we present the full-fledged numerical analysis of the improved Doering–Constantin variational principle for the unrestricted, three-dimensional plane Couette flow. The goal here is not merely to derive the best possible bound, but we also wish to explore the working principles of the method. Even if statements concerning the existence of non-classical scaling remain out of reach at present, the potential power of the new variational principle lies in its great conceptual clarity. Once thoroughly understood, it might serve as a germ for the formulation of a still more advanced principle that could actually allow one to attack the scaling questions.

The present chapter is organized as follows: after §2 is devoted to the resolution of the most demanding technical difficulty, the implementation of the principle’s spectral constraint, we will describe our results in §3. The final §4 offers a concluding discussion. Some important technical details concerning the derivation of the system of differential equations actually used in the numerical computations can be found in appendix A.2, while appendix A.3 contains a brief, but instructive example that illustrates the key points of our method, and underlines its accuracy, without too much technical burden.

Since the numerical work is fairly involved, it would hardly have been possible to carry through the entire investigation without some analytical guidance. Our guide is the example problem of the Couette flow without spanwise degrees of freedom, referred to as the *restricted Couette problem* in the following, which has been treated in detail in the preceding chapters 3 and 4 of this thesis, and which shows several features that will reappear here in the context of the unrestricted problem.

5.2 Evaluation of the spectral constraint

Again we non-dimensionalize the problem stated in §2 of chapter 3 by choosing the gapwidth h as the unit of length. By virtue of the linearity of the equations (3.13) which embody the spectral constraint, and the homogeneous b.c. imposed on the eigenvectors \mathbf{V} , it is not necessary to specify a scale of velocity explicitly. For the sake of notational simplicity we denote all non-dimensionalized quantities by the same symbols as their dimension-carrying counterparts. For

instance, the velocity field $\mathbf{V}(\mathbf{x})$ now is regarded as a dimensionless vector function of the dimensionless coordinates x , y and z .

Utilizing the periodic b.c., we start from the ansatz

$$\mathbf{V}(\mathbf{x}) \equiv \mathbf{v}(z) e^{i(k_x x + k_y y)}, \quad P(\mathbf{x}) \equiv p(z) e^{i(k_x x + k_y y)}$$

and transform the eigenvalue equations (3.13) into the system

$$\lambda v_x = -2 \left(\partial_z^2 - k^2 \right) v_x + R \phi' v_z + i k_x p, \quad (5.1)$$

$$\lambda v_y = -2 \left(\partial_z^2 - k^2 \right) v_y + i k_y p, \quad (5.2)$$

$$\lambda v_z = -2 \left(\partial_z^2 - k^2 \right) v_z + R \phi' v_x + p', \quad (5.3)$$

$$0 = i k_x v_x + i k_y v_y + v'_z, \quad (5.4)$$

with

$$k \equiv \sqrt{k_x^2 + k_y^2}.$$

The corresponding b.c. for the function $\mathbf{v}(z)$ read

$$\mathbf{v}(0) = \mathbf{v}(1) = \mathbf{0}. \quad (5.5)$$

If $k_y = 0$ we encounter the model problem of a Couette flow without spanwise degrees of freedom. Since this restricted problem has already been studied in detail in the chapters 3 and 4 of this thesis, we only need to consider $k_y \neq 0$ here.

Defining the linear operator

$$\mathcal{L} \equiv 2 \left(\partial_z^2 - k^2 \right) + \lambda,$$

(5.1) and (5.2) together with (5.4) yield

$$p = \frac{1}{k^2} [\mathcal{L} v'_z + i k_x R \phi' v_z]. \quad (5.6)$$

Hence, (5.1) can be brought into the form

$$\mathcal{L} v_x = \frac{1}{k^2} \left[k_y^2 R \phi' v_z + i k_x \mathcal{L} v'_z \right], \quad (5.7)$$

and we finally obtain from (5.3) a rather intricate equation for $v_z(z)$:

$$\begin{aligned} \mathcal{L}^2 (\partial_z^2 - k^2) v_z - 4 \frac{\phi^{(2)}}{\phi'} \mathcal{L} (\partial_z^2 - k^2) v'_z - 2 \left[\frac{\phi^{(3)}}{\phi'} - 2 \left(\frac{\phi^{(2)}}{\phi'} \right)^2 \right] \mathcal{L} (\partial_z^2 - k^2) v_z \\ + (k_y R \phi')^2 v_z + i k_x R \phi' \left\{ 2 \mathcal{L} v'_z + \frac{\phi^{(2)}}{\phi'} \mathcal{L} v_z + 4 \left[\frac{\phi^{(3)}}{\phi'} - \left(\frac{\phi^{(2)}}{\phi'} \right)^2 \right] v'_z \right. \\ \left. + 2 \left[\frac{\phi^{(4)}}{\phi'} - 3 \frac{\phi^{(3)} \phi^{(2)}}{(\phi')^2} + 2 \left(\frac{\phi^{(2)}}{\phi'} \right)^3 \right] v_z \right\} = 0, \end{aligned} \quad (5.8)$$

where we rely on the assumption that $\phi'(z)$ does not vanish for all z in the interval $[0, 1]$. The corresponding b.c. for v_z are given by

$$v_z(z)|_{z=0,1} = 0, \quad v'_z(z)|_{z=0,1} = 0, \quad \text{and} \quad \mathcal{L} (\partial_z^2 - k^2) v_z(z)|_{z=0,1} = 0. \quad (5.9)$$

Equations (5.8) and (5.9) constitute a sixth-order Sturm–Liouville eigenvalue problem. If one succeeds in solving this problem, that is, in computing an eigenvalue λ and its eigenfunction $v_z^{(\lambda)}(z)$ for some fixed profile ϕ , wavenumbers k_x and k_y , and a rescaled Reynolds number R , then one can determine the associated components $v_x^{(\lambda)}(z)$ and $v_y^{(\lambda)}(z)$, together with $p^{(\lambda)}(z)$, from (5.7), (5.2), and (5.6), so that an eigenvalue and a corresponding eigenvector $(\mathbf{V}^{(\lambda)}(\mathbf{x}), P^{(\lambda)}(\mathbf{x}))$ of the original eigenvalue problem (3.13) have been found.

Since we cannot hope to find an analytical solution to this formidable problem for each candidate profile ϕ , we have to resort to a numerical treatment. This requires to bring the Sturm–Liouville problem into a form that can actually be dealt with on a computer. We defer the technical details of this reformulation, that rely heavily on the so-called compound matrix method (see e.g. Straughan 1992), to appendix A.2, and present only the final equations here. Although these equations may appear, on a cursory glance, even more cumbersome than the original problem posed by (5.8) and (5.9), they have actually been found well suited for computing the “critical” rescaled Reynolds numbers $R_c\{\phi\}$ for all situations of practical interest, as will be amply demonstrated in the following section.

To begin with, we define the abbreviations

$$R_x \equiv \frac{k_x R}{k^2}, \quad R_y \equiv \frac{k_y R}{k^2}, \quad (5.10)$$

and the auxiliary functions

$$\begin{aligned}
\phi_1(z) &\equiv \phi'(z), \\
\phi_2(z) &\equiv \frac{\phi^{(2)}(z)}{2k}, \\
f_1(z) &\equiv 2 \frac{\phi^{(2)}(z)}{\phi'(z)}, \\
f_2(z) &\equiv 3k + \frac{2}{k} \frac{\phi^{(3)}(z)}{\phi'(z)} - \frac{4}{k} \left(\frac{\phi^{(2)}(z)}{\phi'(z)} \right)^2, \\
g_1(z) &\equiv \phi'(z) - \frac{1}{k^2} \phi^{(3)}(z) + \frac{1}{k^2} \frac{(\phi^{(2)}(z))^2}{\phi'(z)}, \\
g_2(z) &\equiv \frac{1}{2k} \phi^{(2)}(z) - \frac{1}{2k^3} \phi^{(4)} + \frac{3}{2k^3} \frac{\phi^{(3)}(z) \phi^{(2)}(z)}{\phi'(z)} - \frac{1}{k^3} \frac{(\phi^{(2)}(z))^3}{(\phi'(z))^2}, \\
F_{R_y}(z) &= k + \frac{1}{k} \frac{\phi^{(3)}(z)}{\phi'(z)} - \frac{2}{k} \left(\frac{\phi^{(2)}(z)}{\phi'(z)} \right)^2 - \frac{1}{4k} (R_y \phi'(z))^2.
\end{aligned} \tag{5.11}$$

The compound matrix technique outlined in appendix A.2 then yields the following system of 20 ordinary, first-order complex differential equations:

$$\begin{aligned}
y'_1 &= k \left[-3y_1 + y_2 - \frac{1}{2}y_4 - \frac{1}{2}y_6 \right], \\
y'_2 &= k \left[-3y_2 + y_3 + y_5 - \frac{1}{2}y_8 \right], \\
y'_3 &= k \left[-3y_3 + y_4 + y_6 \right], \\
y'_4 &= k \left[\frac{3}{2}y_3 - 3y_4 + y_7 + \frac{1}{2}y_{10} \right] + f_1 \left[-2y_2 + y_4 \right] - f_2 y_1 \\
&\quad - i R_x \left[\phi_1 y_2 + \phi_2 \left(y_1 + \frac{1}{2}y_3 \right) \right], \\
y'_5 &= k \left[-3y_5 + y_6 + \frac{1}{2}y_9 + y_{11} \right], \\
y'_6 &= k \left[-3y_6 + y_7 + y_8 + \frac{1}{2}y_{10} + y_{12} \right], \\
y'_7 &= k \left[\frac{3}{2}y_6 - 3y_7 + y_9 + y_{13} \right] + f_1 \left[-y_1 - 2y_5 + y_7 \right] \\
&\quad - i R_x \left[\phi_1 y_5 + \frac{1}{2} \phi_2 y_6 + g_1 y_1 \right], \\
y'_8 &= k \left[-3y_8 + y_9 + y_{14} \right], \\
y'_9 &= k \left[\frac{3}{2}y_8 - 3y_9 + y_{10} + y_{15} \right] + f_1 \left[-y_2 + y_9 \right] + f_2 y_5 \\
&\quad - i R_x \left[\phi_2 \left(-y_5 + \frac{1}{2}y_8 \right) + g_1 y_2 \right], \\
y'_{10} &= k \left[-3y_{10} + y_{16} \right] + f_1 \left[-y_3 + 2y_8 + y_{10} \right] + f_2 y_6 - i R_x \left[-\phi_1 y_8 - \phi_2 y_6 + g_1 y_3 \right], \\
y'_{11} &= k \left[-3y_{11} + y_{12} + \frac{1}{2}y_{15} + \frac{1}{2}y_{17} \right],
\end{aligned}$$

$$\begin{aligned}
y'_{12} &= k \left[-3 y_{12} + y_{13} + y_{14} + \frac{1}{2} y_{16} \right], \\
y'_{13} &= k \left[\frac{3}{2} y_{12} - 3 y_{13} + y_{15} - \frac{1}{2} y_{19} \right] + f_1 [-2 y_{11} + y_{13}] + F_{R_y} y_1 \\
&\quad + i R_x \left[-\phi_1 y_{11} - \frac{1}{2} \phi_2 y_{12} + g_2 y_1 \right], \\
y'_{14} &= k [-3 y_{14} + y_{15} + y_{17}], \\
y'_{15} &= k \left[\frac{3}{2} y_{14} - 3 y_{15} + y_{16} + y_{18} - \frac{1}{2} y_{20} \right] + f_1 y_{15} + f_2 y_{11} + F_{R_y} y_2 \\
&\quad + i R_x \left[\phi_2 \left(y_{11} - \frac{1}{2} y_{14} \right) + g_2 y_2 \right], \\
y'_{16} &= k [-3 y_{16} + y_{19}] + f_1 [2 y_{14} + y_{16}] + f_2 y_{12} + F_{R_y} y_3 \\
&\quad + i R_x [\phi_1 y_{14} + \phi_2 y_{12} + g_2 y_3], \\
y'_{17} &= k \left[-3 y_{17} + y_{18} - \frac{1}{2} y_{20} \right], \\
y'_{18} &= k \left[\frac{3}{2} y_{17} - 3 y_{18} + y_{19} \right] + f_1 [y_{11} + y_{18}] + F_{R_y} y_5 \\
&\quad + i R_x \left[-\frac{1}{2} \phi_2 y_{17} + g_1 y_{11} + g_2 y_5 \right], \\
y'_{19} &= k [-3 y_{19} + y_{20}] + f_1 [y_{12} + 2 y_{17} + y_{19}] + F_{R_y} y_6 + i R_x [\phi_1 y_{17} + g_1 y_{12} + g_2 y_6], \\
y'_{20} &= -3k y_{20} + f_1 [y_{14} + y_{20}] - f_2 y_{17} + F_{R_y} y_8 + i R_x [-\phi_2 y_{17} + g_1 y_{14} + g_2 y_8].
\end{aligned} \tag{5.12}$$

These equations have to be supplemented with the initial conditions required for their numerical integration from $z = 0$ to $z = 1$:

$$y_{20}(0) = 1, \quad y_i(0) = 0 \quad \text{for } i = 1, \dots, 19. \tag{5.13}$$

In addition, we merely have to satisfy the fairly simple boundary condition

$$y_1(1) = 0. \tag{5.14}$$

What matters here is precisely the replacement of the rather troublesome, symmetric boundary conditions (5.9) accompanying the original Sturm–Liouville problem by the asymmetric boundary conditions (5.13) and (5.14), since these new boundary conditions lend themselves to a standard shooting method: just integrate the system (5.12) with the initial conditions (5.13), monitor the resulting value of $y_1(1)$, and adjust the system's parameters such that this value becomes zero.

The price to pay for this simplification is a rather complicated system of equations. But still, the spirit underlying these equations is simple. Since we are not interested in the full spectrum of the eigenvalue problem (3.13) (or, equivalently, in that of the Sturm–Liouville problem (5.8, 5.9)), but only in that value $R_c\{\phi\}$ of R where the lowest eigenvalue associated with some profile ϕ passes through zero, we were entitled to set $\lambda = 0$ in the derivation of the system (5.12). We

then keep both the profile ϕ and the wavevector \mathbf{k} fixed when solving the initial value problem (5.12, 5.13), and adjust only the parameter R . The smallest value of R where $y_1(1)$ vanishes then equals that value of R where the smallest eigenvalue λ becomes zero, for this particular ϕ and \mathbf{k} . We denote this R as

$$R_0\{\phi\}(\mathbf{k}). \quad (5.15)$$

The desired number $R_c\{\phi\}$ then is identified as the global minimum, taken over all wavevectors. Since the wavenumbers k_x and k_y effectively enter into the system (5.12) only through their squares k_x^2 and k_y^2 , we have

$$R_c\{\phi\} = \min_{k_x \geq 0, k_y > 0} \{R_0\{\phi\}(\mathbf{k})\}. \quad (5.16)$$

Thus, the evaluation of the spectral constraint, i.e. the determination of the maximal rescaled Reynolds number $R_c\{\phi\}$ up to which a given profile ϕ remains an admissible test profile for the variational principle (3.12), requires some labour. One first has to determine, for that ϕ and a representative set of wavevectors \mathbf{k} , the first zero of $y_1(1)$ that occurs when R is increased from zero to positive numbers. This yields the values (5.15). In a second step one has to locate the global minimum of all these values, which equals $R_c\{\phi\}$.

5.3 Results

Now that we are in a position to evaluate the spectral constraint (3.13) for an arbitrary profile $\phi(z)$, we have to specify a class of test profiles that is likely to exhaust the variational principle (3.12, 3.18). Based on the analysis of the restricted Couette problem, we propose the following class of variational profiles:

$$\phi(z) = \begin{cases} \frac{1}{2}(1-p) + pz - \frac{1}{2}(1-p)(1-z/\delta)^n & \text{for } 0 \leq z \leq \delta \\ \frac{1}{2}(1-p) + pz & \text{for } \delta < z < 1 - \delta \\ \frac{1}{2}(1-p) + pz + \frac{1}{2}(1-p)(1 - (1-z)/\delta)^n & \text{for } 1 - \delta \leq z \leq 1 \end{cases}. \quad (5.17)$$

These profiles contain three independent parameters:

- i.) the boundary layer thickness δ ($0 < \delta \leq \frac{1}{2}$),
- ii.) the slope p of the profile in the interior ($0 < p \leq 1$), and
- iii.) the polynomial order n ($n = 4, 5, \dots$) of the boundary layer segments.

By construction, each ϕ is $n - 1$ times continuously differentiable at the matching points $z = \delta$ and $z = 1 - \delta$. Since the right hand side of the system (5.12) of differential equations contains

derivatives of the profile up to the fourth order, the smallest value of n allowed by this system is four. In the case $n = 4$ one encounters a discontinuity of the fourth derivative. But as long as this discontinuity remains finite, it poses no problem for the numerical integration. For practical computations we restrict the parameter n to values less than or equal to 1000.

At this point it needs to be emphasized that the variational parameter n plays an important role for the numerical solution of the variational principle. If this parameter was artificially kept fixed, that is, if one considered the profiles (5.17) with a constant parameter $n = 4$, say, then one would inevitably be confronted with serious divergences which are hard to deal with numerically, and therefore would drastically reduce the maximal attainable Reynolds numbers. The formal reasons for these difficulties lie in the expressions $\phi^{(2)}(z)/\phi'(z)$ and $\phi^{(3)}(z)/\phi'(z)$, which enter into the system (5.12) through the auxiliary functions (5.11). Namely, for high Reynolds numbers the optimized profiles tend to become flat in the interior, so that one has to face small denominators.

Since the solution to this technical problem, achieved with the help of the variational parameter n , is of outstanding practical importance, we illustrate it with an example. Let us first note that the parameters δ and n are related to each other by the profile's slope at $z = 0$ (or, equivalently, at $z = 1$):

$$\phi'(0) = p + \frac{n}{2\delta}(1-p). \quad (5.18)$$

Secondly, we anticipate the high- Re -scaling behaviour of the optimized profiles: we have

$$\phi'(0) \sim \alpha Re \quad \text{and} \quad \phi'\left(\frac{1}{2}\right) = p \sim \beta Re^{-1}$$

with constants α and β , as will be shown later on (cf. (5.23) and (5.24)). This implies that the ratio $n/(2\delta)$ in (5.18) necessarily has to increase about linearly with Re when Re becomes large. We now focus on two different parameter combinations: (a) $\delta = 0.5$ and $n = 1000$, and (b) $\delta = 0.002$ and $n = 4$. In both cases the ratio $n/(2\delta)$ takes on the value 1000, and what matters now is the way the divergences of $\phi^{(2)}(z)/\phi'(z)$ and $\phi^{(3)}(z)/\phi'(z)$ manifest themselves when the profile slope p approaches zero. Case (a) is actually met in high- Re -solutions of the variational principle when the shape of the profiles' boundary segments is allowed to vary, whereas this shape is artificially kept fixed in case (b). In figures 5.1 and 5.2 we demonstrate for these two cases the response of $\phi^{(2)}(z)/\phi'(z)$ to the variation of p from 0.1 to smaller values, depicting only the relevant intervals of z . In case (a) the decrease of p merely entails a shift of the smooth ascend from the (negative) value at $z = 0$ to zero. In marked contrast, in case (b) the same decrease of p produces a rather sharp singularity in the vicinity of $z = \delta$. The expression $-\phi^{(3)}(z)/\phi'(z)$ shows, qualitatively, the same behaviour, but even more pronounced. While

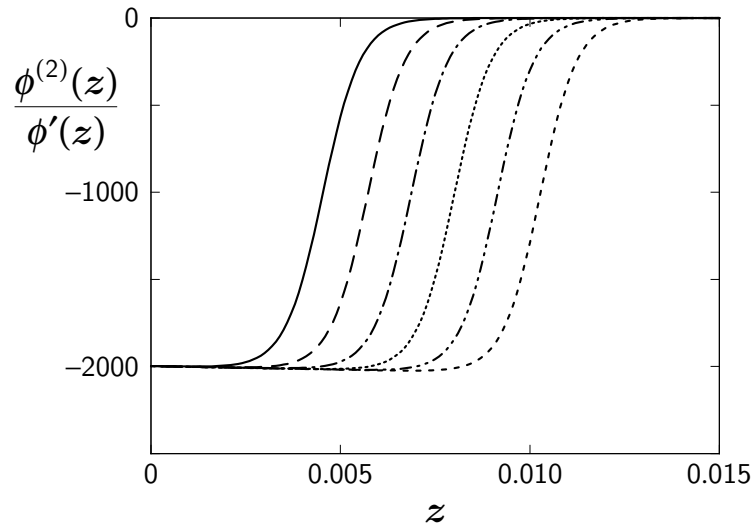


Figure 5.1: Behaviour of $\phi^{(2)}(z)/\phi'(z)$ in the interval $0 \leq z \leq 0.015$ for $\delta = 0.5$ and $n = 1000$. From left to right: graphs that result when p is successively diminished by factors of 1/10 from $p = 0.1$ to $p = 10^{-6}$.

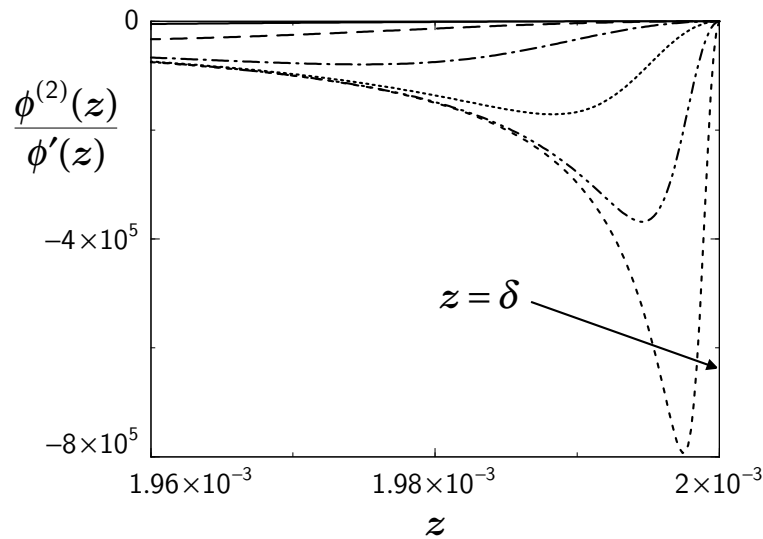


Figure 5.2: Behaviour of $\phi^{(2)}(z)/\phi'(z)$ in the vicinity of $z = \delta$ for $\delta = 0.002$ and $n = 4$. From top to bottom: graphs that result when p is successively diminished by factors of 1/10 from $p = 0.1$ to $p = 10^{-6}$, cf. figure 5.1.

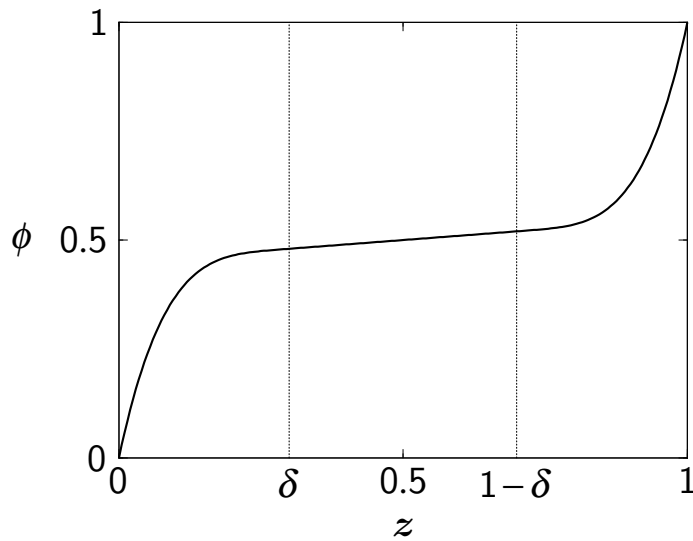


Figure 5.3: Test profile $\phi(z)$ as given by (5.17), for a generic parameter set ($n = 4$, $\delta = 0.3$, $p = 0.1$).

the functions shown in figure 5.1 are easy to handle, a singularity like the one that develops in figure 5.2 would soon limit the accessible values of p , and thus prevent us from reaching asymptotically high Reynolds numbers.

At this point, an important difference between the full three-dimensional plane Couette problem and the restricted, two-dimensional problem without spanwise degrees of freedom shows up. The cumbersome denominator ϕ' , which does *not* appear in the restricted case, emerges when one eliminates $v_x(z)$ from (5.3) in order to derive the Sturm–Liouville equation (5.8). In this way one arrives at (5.7), whereas in the restricted case ($k_y = 0$) the condition (5.4) of divergence-freeness yields an immediate connection between v_x and v'_z . Here lies the reason why an asymptotic theory of upper bounds for the full Couette problem, paralleling the one developed for the restricted case in chapter 4, seems to be out of reach. Nevertheless, the model problem has led to the identification of the test profiles (5.17) as profiles which will provide the best possible bounds on c_ε in the limit of large Reynolds numbers.

In figure 5.3 we visualize a generic representative of the profile family (5.17). The profile functional (3.11), which becomes a function of δ , p , and n when applied to the class (5.17), now reads

$$D\{\phi\} = \left[\frac{1}{2} \frac{n^2}{(2n-1)\delta} - 1 \right] (1-p)^2 \equiv \mathcal{D}(\delta, p, n).$$

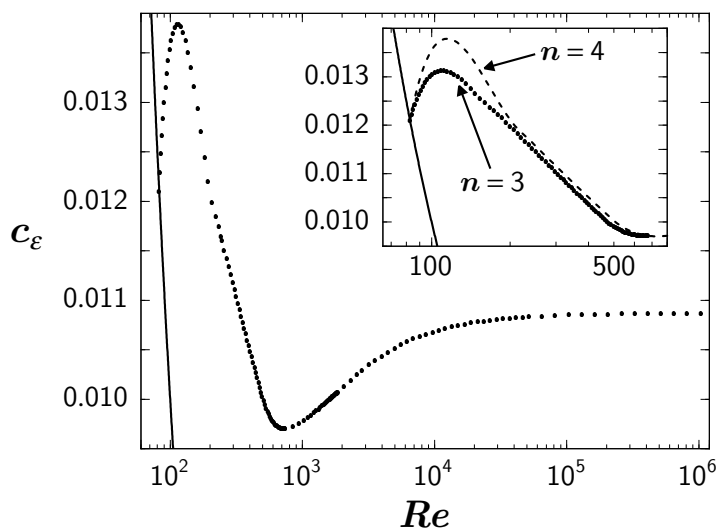


Figure 5.4: Bounds on c_ε for the plane Couette flow. Points denote the variational upper bound $\overline{c_\varepsilon}(Re)$ computed numerically with the test profiles (5.17); the solid line on the left is the lower bound $\underline{c_\varepsilon}(Re) = Re^{-1}$. The asymptotic value of the upper bound, $\lim_{Re \rightarrow \infty} \overline{c_\varepsilon}(Re) = 0.01087(1)$, lies slightly above, but within the uncertainty span of Busse's asymptotic result (3.8). — The inset depicts the improvement obtained by preassuming that the wavevector minimizing $R_0\{\phi\}(\mathbf{k})$ has a vanishing component in streamwise direction. Solid line: lower bound $\underline{c_\varepsilon}(Re)$; dashed line: same upper bound as in the main figure; points: improvement of the bound obtained by admitting the parameter value $n = 3$.

By constructing the lower envelope of all graphs of the type shown in figure 3.1 (chapter 3), that are produced in the (Re, c_ε) -plane by the individual test profiles, we are able to compute the optimal upper bound on c_ε obtainable from the profiles (5.17) for Reynolds numbers up to $Re \approx 10^6$. Moreover, from the optimized profiles we can extract the asymptotic scaling of the profile parameters.

In figure 5.4 we report our findings for the optimized upper bound $\overline{c_\varepsilon}(Re)$ on $c_\varepsilon(Re)$. Remarkably, this variational bound separates *with a sharp kink* from the lower bound $\underline{c_\varepsilon}(Re) = Re^{-1}$ at the energy stability limit, which is located at

$$Re_{ES} = 82.65014887(1), \quad c_\varepsilon(Re_{ES}) = Re_{ES}^{-1} = 0.012099191758(2). \quad (5.19)$$

(The numbers in brackets denote the uncertainty of the last digit.) Up to Re_{ES} both bounds coincide, see (3.7). The kink of the upper bound at Re_{ES} is no artifact caused by our particular

choice of test profiles (5.17): even though some numerical improvement of the upper bound \overline{c}_ε is possible in the regime of intermediate Re (see below), one will still obtain a bound that *increases* for Reynolds numbers slightly above Re_{ES} . This behaviour is related to the singularity of the balance parameter a at Re_{ES} (see chapter 2 and 3), and finds its explanation in a change of the role of the optimal background flow. Below Re_{ES} the optimal background flow coincides with the laminar flow, that is, with a stationary solution to the Navier–Stokes equations, but above Re_{ES} this is no longer the case. Therefore, the deviations $\mathbf{v}(\mathbf{x}, t)$ from the background flow below and above Re_{ES} have a different character. For $Re < Re_{ES}$ these deviations are fluctuations around the physically realized laminar flow. Since they will decay at least exponentially in time (Joseph 1976; Drazin & Reid 1981), they yield no contribution to ε . For $Re > Re_{ES}$ the deviations can no longer be regarded as “fluctuations” in the usual sense, and do contribute to ε .

The apparent slight non-smoothness of our bound \overline{c}_ε at $Re \approx 200$, on the other hand, indeed is an artifact; it is caused by the restriction of n to values no less than four. We have found empirically that the component k_x of the wavevector minimizing $R_0\{\phi\}(\mathbf{k})$ always vanishes. With this knowledge, the system (5.12) can be simplified: the 20-component complex system is converted into a 20-component real one. As a consequence, the parameter value $n = 3$ becomes admissible, which results in a noticeable improvement of the upper bound in the intermediate range $Re_{ES} < Re < 700$, as shown in the inset of figure 5.4.

For Reynolds numbers around 740 the upper bound exhibits a pronounced minimum, and then ascends to the asymptotic value

$$\lim_{Re \rightarrow \infty} \overline{c}_\varepsilon(Re) = 0.01087(1). \quad (5.20)$$

This value lies slightly above — but within the uncertainty span of — Busse’s asymptotic result (3.8). Thus, our variational bound possesses the same asymptotic Re^0 -scaling as the bound provided by the Optimum Theory. In appendix A.3 we treat the variational principle *without* taking into account the condition $\nabla \cdot \mathbf{V} = 0$ in (3.13). This toy problem provides an illustrative example for our methods, and allows a direct comparison of variational results obtained numerically with the help of the profiles (5.17) to the corresponding results derived by Howard (1972) (see also Busse 1996) in the framework of the Howard–Busse theory. Our numerical value for the asymptotic bound pertaining to this simplified case, $\lim_{Re \rightarrow \infty} \overline{c}_\varepsilon(Re) \approx 0.07071$, differs from Howard’s analytical value $9/128 \approx 0.07031$ by merely 0.6%, even though our variational profiles are specifically adapted to the full problem, and *not* to this simplified case.

A key for understanding the overall behaviour of the variational upper bound lies in the expressions $R_0\{\phi\}(\mathbf{k})$, considered for fixed profile ϕ as functions of the two-dimensional wavevector \mathbf{k} . We have already mentioned the observation that for each considered test profile the absolute

minimum of $R_0\{\phi\}(\mathbf{k})$ was attained for $k_x = 0$. This finding may seem surprising on the first glance, but becomes at least plausible with the help of the following argument: if one neglects the condition $\nabla \cdot \mathbf{V} = 0$ in (3.13), the minimizing \mathbf{k} -vector is the zero-vector, as shown in appendix A.3. Taking into account $\nabla \cdot \mathbf{V} = 0$ then enforces that the minimizing \mathbf{k} becomes non-zero. But since there is no characteristic length-scale in streamwise direction, the minimizing k_x remains zero.

There is a further feature that strongly influences the Re -dependence of the optimized profile parameters, and the scaling behaviour of the resulting upper bound $\overline{c}_\varepsilon(Re)$: the single minimizing wavenumber k_y that characterizes the variational solution at comparatively low Re bifurcates to a pair of minimizing wavenumbers, $k_{y,1}$ and $k_{y,2}$, at the Reynolds number

$$Re_B \approx 460. \quad (5.21)$$

The variational principle possesses the intriguing property that above Re_B both corresponding minimal values of $R_0\{\phi\}(\mathbf{k})$, R_1 and R_2 , are locked to exactly the same value, i.e. *two eigenvalues of the eigenvalue problem (3.13) pass through zero simultaneously*. This degeneracy reflects the fact that, physically speaking, the sensitivity of the variational problem to the behaviour of the profiles in the boundary layers separates from the sensitivity to the profiles in the interior. A fairly precise mathematical formulation of this statement is given for the Couette problem without spanwise degrees of freedom in the preceding chapter of this thesis.

The consequences of this bifurcation for the upper bound on c_ε are dramatic: *its approximate $Re^{-1/4}$ -dependence that prevails for $Re \leq Re_B$ changes to the asymptotic Re^0 -behaviour*, while the bound passes through its global minimum

$$\overline{c}_{\varepsilon min} \approx 0.00970 \quad \text{at} \quad Re_{min} \approx 740. \quad (5.22)$$

In order to convey some feeling for the way the variational principle works, we draw $R_0\{\phi\}(\mathbf{k})$ as function of both components of \mathbf{k} , for the optimized profiles corresponding to the Reynolds numbers Re_{ES} (figure 5.5; cf. (5.19)) and Re_{min} (figure 5.6; cf. (5.22)), respectively. Figure 5.7 depicts the minimizing values of k_y that belong to the variational bound displayed in figure 5.4. Whereas the upper k_y -branch scales proportionally to Re in the limit of large Re , the lower branch approaches a constant value. This value is *precisely* the one that also corresponds to the energy stability limit:

$$\lim_{Re \rightarrow \infty} \frac{k_{y,1}}{2\pi} = \frac{k_{ES}}{2\pi} \approx 0.4960.$$

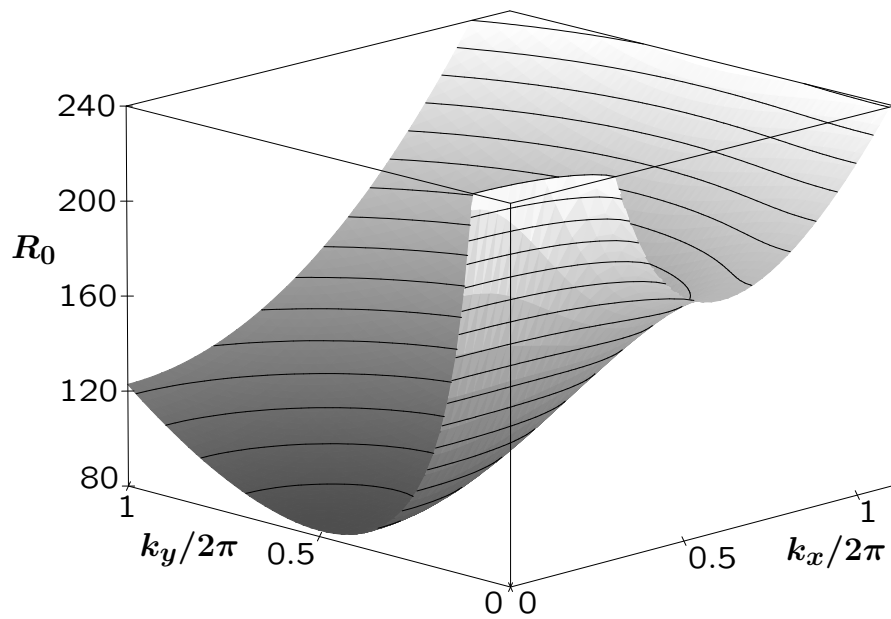


Figure 5.5: Three-dimensional surface plot visualizing the \mathbf{k} -dependence of $R_0\{\phi\}(\mathbf{k})$ for the laminar profile, which is the optimized profile for Reynolds numbers up to the energy stability limit Re_{ES} .

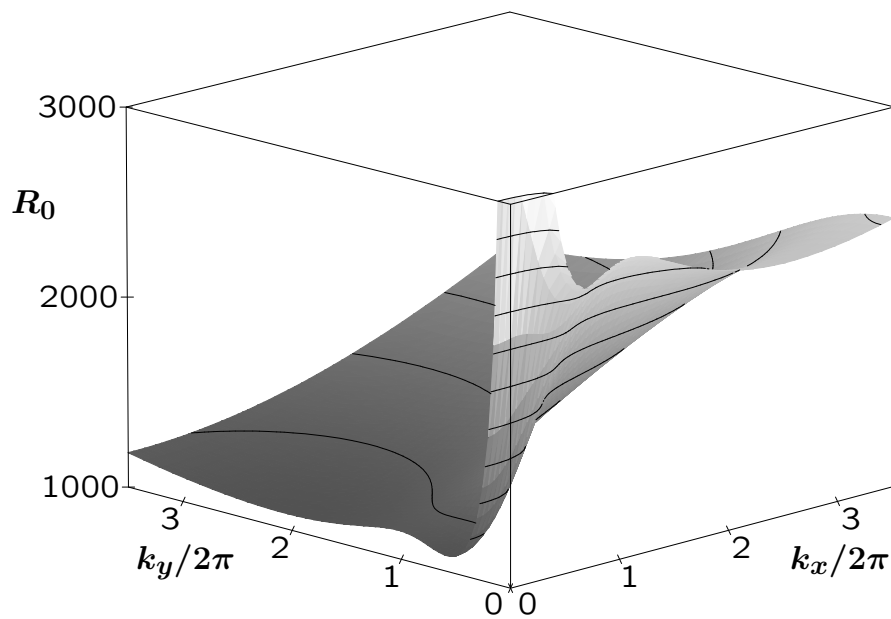


Figure 5.6: Three-dimensional surface plot visualizing the \mathbf{k} -dependence of $R_0\{\phi\}(\mathbf{k})$ for the optimized profile belonging to the absolute minimum of the upper bound on c_ε at $Re = Re_{min} \approx 740$. Note the appearance of two distinct minima on the k_y -axis. Since the profile results from the variational principle, both minima have the same value.

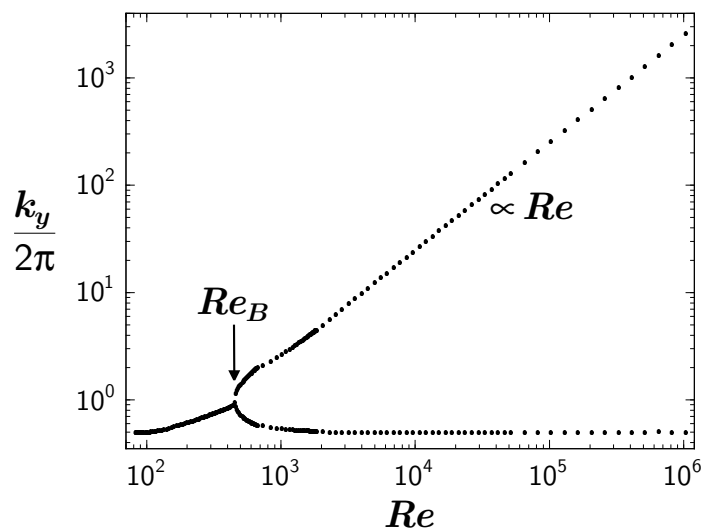


Figure 5.7: Minimizing wavenumber(s) k_y corresponding to the upper bound on c_ε displayed in figure 5.4.

This finding is rather unexpected, since we have the simple laminar profile at the energy stability limit, and seemingly entirely different, nonlinear profiles with an almost flat interior part in the asymptotic regime. However, the restricted model problem has shown that this interior part of the asymptotic profiles can be related to the laminar profile, so that the asymptotic identity of $k_{y,1}$ and k_{ES} can be proven analytically by mapping the corresponding eigenvalue problems to each other (chapter 4).

It is now of considerable mathematical and physical interest to investigate the Re -dependence of the optimized profile parameters. We have to keep in mind that the background flow $\mathbf{U}(\mathbf{x}) = U\phi(z)\hat{\mathbf{x}}$ is, by construction, *not* a horizontally-averaged mean flow. On the other hand, the optimal profiles ϕ invite comparison with physically realized flow profiles (Kerswell 1997), even though such a comparison remains speculative. Figure 5.8 shows the metamorphosis of the optimal profiles with increasing Reynolds number. By a close inspection of the data underlying this figure, we can clearly distinguish four different regimes:

- i.) For $Re_{ES} \leq Re \leq Re_1 \approx 160$, a *deformation of the laminar profile* takes place. Whereas the thickness δ of the boundary layers remains fixed at 0.5, and the polynomial order n of the boundary segments remains at the smallest possible value 3, the profile's slope p in the interior decreases from 1 to almost the limiting value 0. In this regime the upper bound \bar{c}_ε reaches its maximum and starts to descend.

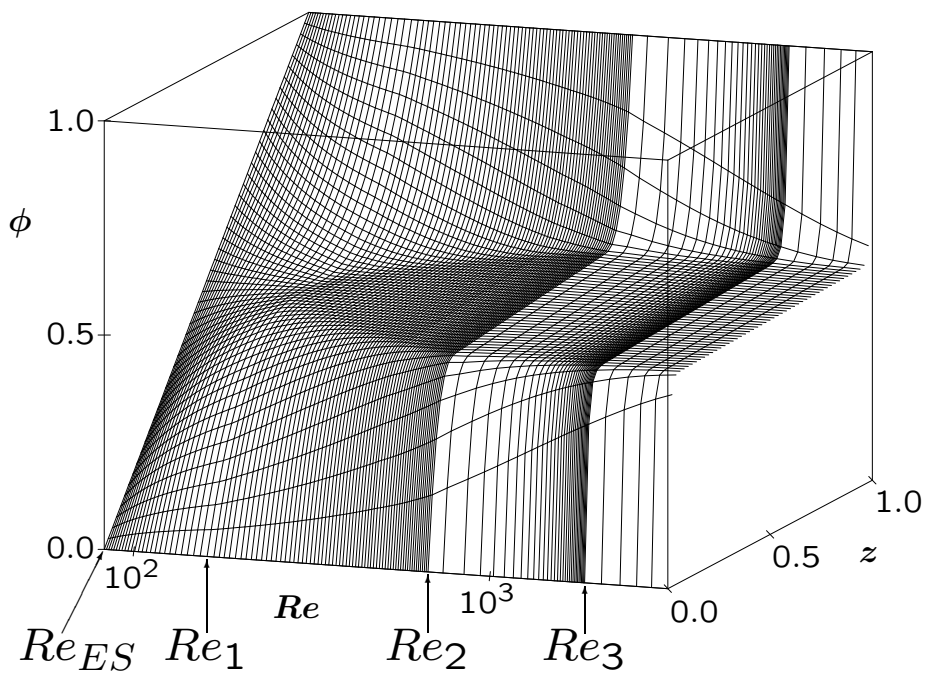


Figure 5.8: Three-dimensional plot visualizing the metamorphosis of the optimized variational profiles with the increase of the Reynolds number. We have depicted the most important Re -interval on a logarithmic scale, beginning with the energy stability limit Re_{ES} and ending in the scaling regime $Re > Re_3$.

- ii.) The following regime, $Re_1 \leq Re \leq Re_2 \approx 670$, is characterized by the *development of boundary layers*. The parameter δ decreases to its minimal value of about 0.14, with n remaining fixed at 3, while the slope p increases again. In this regime the bifurcation of the minimizing k_y occurs, which alters the previous approximate $Re^{-1/4}$ -behaviour of the upper bound.
- iii.) In the next regime, $Re_2 \leq Re \leq Re_3 \approx 1845$, we observe a dramatic change of the shape of the optimized profile's boundary segments. The parameter n — characterizing the shape of these segments by means of their polynomial order — increases from the smallest possible value $n = 3$ to $n = 34$, thus steepening the profiles in the immediate vicinity of each boundary, thereby effectively generating new internal boundary layers within the original boundary layers. As a consequence of this *structural reorganization of the boundary layers*, the entire boundary segments, the extensions of which are quantified by δ , start to reach deeper and deeper into the bulk and finally join again, δ taking on its maximal value 0.5. In this regime, the upper bound passes through its minimum, see (5.22), and then changes the sign of its curvature.
- iv.) For Re above Re_3 , we find simple scaling laws for the optimal profile parameters. These scaling laws give rise to a *power-law change of the profile* with increasing Re : the slope at the boundary $z = 0$ (or at $z = 1$) is given by

$$\phi'(0) \sim \frac{n}{2\delta} \sim \alpha Re, \quad (5.23)$$

while the slope at the midpoint $z = \frac{1}{2}$ becomes

$$\phi'\left(\frac{1}{2}\right) = p \sim \beta Re^{-1}, \quad (5.24)$$

with constants α and β . Parallel to this power-law change of the profile, the upper bound on c_ε ascends smoothly to its asymptotic value.

If we had not been forced by practical numerical reasons to constrain the shape parameter n to values less than or equal to 1000, we would have preserved the asymptotic Re^1 -scaling of n , while the parameter δ would have remained fixed at 0.5. In our numerics the optimal n becomes 1000 at $Re \approx 51880$, and keeping n fixed at $n = 1000$ for even higher Re instead of allowing it to increase further then forces δ to decrease, as follows from (5.23). The ensuing increase of the asymptotic value of the upper bound \bar{c}_ε (compared to the value that would be obtainable if one allowed arbitrarily large n) is quite small, as can be seen from the fact that $\bar{c}_\varepsilon(51880) = 0.010832(1)$ differs merely by about 0.3% from the asymptotic value (5.20).

5.4 Conclusions

Figure 5.9 gives a synopsis of rigorous upper bounds on the dimensionless rate of energy dissipation (3.6) in plane Couette flow that have been found so far (see also figure 3.14). The topmost

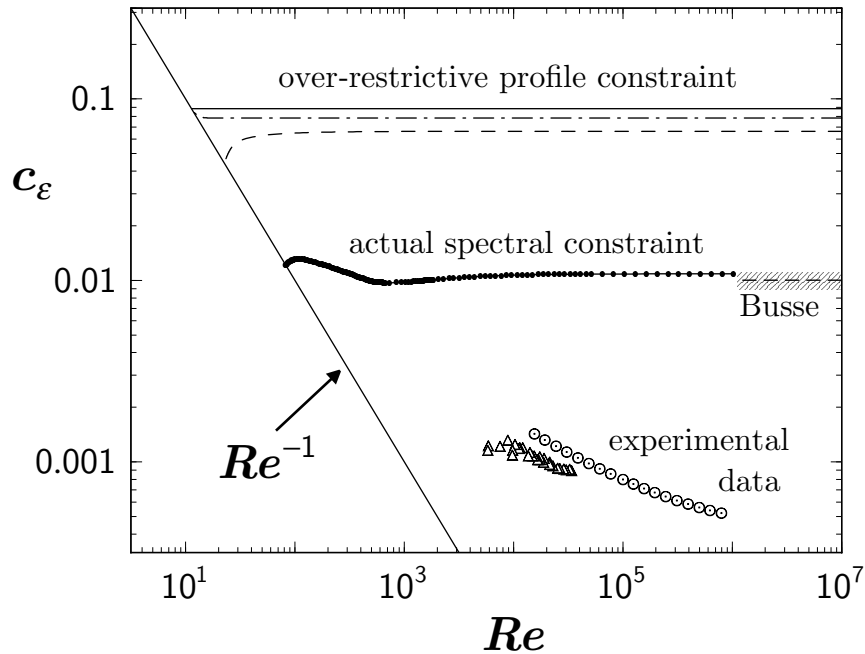


Figure 5.9: Comparison of bounds on $c_\varepsilon(Re)$ for the plane Couette flow. — Solid slanted straight line: lower bound $\underline{c}_\varepsilon(Re) = Re^{-1}$. — Topmost horizontal solid line: upper bound obtained by Doering & Constantin (1992, 1994) with the help of an over-restrictive profile constraint and piecewise linear profiles; $\overline{c}_\varepsilon(Re) \approx 0.088$ for $Re > 11.32$. — Dashed-dotted line: improved bound on $c_\varepsilon(Re)$ derived by Gebhardt *et al.* (1995) from the analytical solution of the Doering–Constantin principle with the over-restrictive constraint; $\overline{c}_\varepsilon(Re) \approx 0.079$ for $Re > 16.98$. — Long-dashed line: further improvement due to the introduction of the balance parameter, see chapter 2; $\overline{c}_\varepsilon(Re) \rightarrow 0.066$. This bound is still calculated analytically utilizing the over-restrictive profile constraint. — Heavy dots: upper bound for the plane Couette flow obtained in this chapter from the variational principle (3.12) with the actual spectral constraint (3.13), cf. figure 5.4; $\overline{c}_\varepsilon(Re) \rightarrow 0.01087(1)$. The variational profiles are given by (5.17), including $n = 3$ as an admissible parameter. — Joining dashed line: asymptotic upper bound (3.8) derived by Busse (1970, 1978); $\overline{c}_\varepsilon(Re) \rightarrow 0.010(1)$. The shaded area denotes the estimated uncertainty of this bound. — Triangles: experimental dissipation rates for the plane Couette flow measured by Reichardt (1959). — Circles: experimental dissipation rates for the Taylor–Couette system with small gap as measured by Lathrop, Fineberg & Swinney (1992).

three lines indicate results derived with the help of an over-restrictive profile constraint (Doering & Constantin 1992, 1994; Gebhardt *et al.* 1995; chapter 2 of this thesis) stemming from functional estimates. This sharpened constraint over-satisfies the actual spectral constraint (3.13) and thus leads to bounds exceeding the asymptotic Busse bound (3.8) by factors of 8.8, 7.9, or 6.6, respectively. Only if the spectral constraint is properly implemented and evaluated, as done in this thesis, one can obtain a rigorous bound that practically coincides with the Busse bound in the asymptotic regime, thereby confirming both Busse's pioneering work (Busse 1970, 1978) and Kerswell's recent analysis (Kerswell 1997).

However, it must be clearly recognized that much more has been achieved than the confirmation of a 25-year old difficult result. Now a variational principle is available that can not only produce asymptotic bounds of high quality, but yields rigorous bounds of the same quality in the entire range from low to asymptotically high Reynolds numbers. For the plane Couette system discussed in this thesis, the bound shows a remarkable structure, notably a pronounced minimum followed by a *Re*-range between 1000 and 1800 in which the bound's curvature changes its sign. This occurs at about those Reynolds numbers where typical laboratory shear flows start to become turbulent. It is tempting to speculate about this coincidence, but such considerations are beyond the scope of the present work.

Of considerable interest is the mechanism that determines the variational upper bound. As depicted in figure 5.7, the minimizing wavenumber k_y bifurcates at $Re_B \approx 460$, giving rise to one minimizing k_y -branch that asymptotically approaches a constant, and to another one that scales linearly with *Re*. Since both corresponding minima determine the solution to the variational principle by taking on the same value, as described in § 3, there are two characteristic lengths that enter into the solution, one scaling with Re^0 , the other with Re^{-1} . The analysis of the restricted Couette problem (chapters 3 and 4) has led to the conclusion that the first, *Re*-independent minimum reflects the response of the variational principle to the optimized profiles solely in the interior of the fluid layer, whereas the second minimum reflects the response to solely the profiles' boundary segments. Thus, the two lengths entering the variational solution can be identified as basically (i) the extension of the interior flat part of the optimized profile, and (ii) the effective width of its (internal) boundary layers. It is structural insight of this kind that will be required for the formulation of a more refined variational principle that might ultimately allow one to decide whether there are corrections to classical scaling.

For the moment being, the comparison of our variational bound with the experimental data shown in figure 5.9 demands some modesty. The bound clearly is far from being sharp; the difference between the variational bound \bar{c}_ε and the corresponding data measured by Reichardt (1959) for the plane Couette flow or by Lathrop, Fineberg & Swinney (1992) for the small-gap Taylor–Couette system still spans an order of magnitude. In short, one important step has been made, but there is still a long way to go.

Zum Abschluß dieser Arbeit möchte ich all denen aufrichtig danken, die zu ihrer Entstehung direkt oder indirekt beigetragen haben.

Allen voran gilt mein Dank meinem Doktorvater, Herrn Prof. Siegfried Großmann, für die beständige Förderung während der Promotion. Die Vielzahl inspirierender Diskussionen mit ihm, sein großes, nicht erlahmendes Interesse an meiner Arbeit, die freundschaftlichen Gespräche; die Erinnerung an all dieses erfüllt mich mit tiefem Dank und wird mir hoffentlich eine geistige Quelle weit über meine Promotionszeit hinaus werden.

Ein ganz besonderes Dankeschön geht an Herrn Priv.-Doz. Dr. Martin Holthaus für die ausgezeichnete Zusammenarbeit. Er hatte jederzeit ein offenes Ohr für alle mit meiner Arbeit verbundenen Fragen, Probleme und Lösungen. Insbesondere konnte ich bei der Formulierung der Publikationen stark von seiner sprachlichen Gewandtheit profitieren. Der en passant abgehaltene "Englisch Kursus" bleibt mir in bester Erinnerung. Auch danke ich ihm für die bereitwillige Übernahme der Zweitkorrektur.

Allen Mitgliedern der Arbeitsgruppe danke ich für das hervorragende Arbeitsklima. Ein Dankeschön speziell an Dr. Alexander Esser für die vielen Gespräche und die gründliche Durchsicht der Manuskripte, an Dipl.-Phys. Achim Reeh für die tatkräftige Unterstützung bei allen Computer- und Programmierproblemen und an Herrn Priv.-Doz. Dr. Detlef Lohse für seine ermunternden Kommentare zu meinen Arbeiten.

Meiner Mutter möchte ich dafür danken, daß sie mir, trotz abgeschlossener Berufsausbildung, ermöglicht hat, mein zweites Studium mit Stringenz durchzuführen.

Schließlich danke ich meiner Frau Heike, die alle Höhen und Tiefen dieser Arbeit in Liebe mitgetragen hat, und meinem Sohn Jonas, der mich durch sein bloßes Dasein jeden Tag aufs neue lehrt, über meine Arbeit hinauszublicken.

Diese Dissertation wurde gefördert vom Sonderforschungsbereich "Nichtlineare Dynamik", SFB 185.

Appendix A

A.1 Boundary value problem for rescaled profile functions with “infinitely” extended interior

In this appendix we evaluate the right hand side of (4.48). To this end, we consider in a first step the system of differential equations (4.29)–(4.34) for $\xi \geq 0$ with arbitrary initial conditions and a *constant* function $\tilde{\phi}(\xi)$. For notational simplicity we write $\mathbf{y}(\xi)$ and $\phi(\xi)$ instead of $\tilde{\mathbf{y}}(\xi)$ and $\tilde{\phi}(\xi)$, respectively. The initial value problem then reads

$$\mathbf{y}'(\xi) = 2\kappa A_0 \mathbf{y}(\xi), \quad \mathbf{y}(0) = \mathbf{y}_0; \quad (\text{A.1})$$

the constant matrix A_0 is defined in (4.41). With the help of the Jordan normal form of A_0 ,

$$J \equiv C^{-1} A_0 C = \begin{pmatrix} 0 & 0 & 0 & 0 & 0 & 0 \\ 0 & -2 & 0 & 0 & 0 & 0 \\ 0 & 0 & -1 & 1 & 0 & 0 \\ 0 & 0 & 0 & -1 & 1 & 0 \\ 0 & 0 & 0 & 0 & -1 & 0 \\ 0 & 0 & 0 & 0 & 0 & -1 \end{pmatrix},$$

where the transformation matrix C is given by

$$C \equiv \frac{1}{16} \begin{pmatrix} 3 & 3 & 2 & 0 & 10 & 0 \\ 3 & -3 & 0 & 2 & 0 & 0 \\ 0 & 0 & 0 & 0 & 0 & 16 \\ 3 & 3 & -2 & 0 & -6 & 0 \\ 3 & -3 & 0 & -2 & 0 & 0 \\ 3 & 3 & 2 & 0 & -6 & 0 \end{pmatrix},$$

we find the solution

$$\mathbf{y}(\xi) = Y(\xi) C^{-1} \mathbf{y}_0$$

with

$$Y(\xi) = \frac{1}{16} \begin{pmatrix} 3 & 3e^{-4\kappa\xi} & 2e^{-2\kappa\xi} & 4\kappa\xi e^{-2\kappa\xi} & [10 + 4\kappa^2\xi^2] e^{-2\kappa\xi} & 0 \\ 3 & -3e^{-4\kappa\xi} & 0 & 2e^{-2\kappa\xi} & 4\kappa\xi e^{-2\kappa\xi} & 0 \\ 0 & 0 & 0 & 0 & 0 & 16e^{-2\kappa\xi} \\ 3 & 3e^{-4\kappa\xi} & -2e^{-2\kappa\xi} & -4\kappa\xi e^{-2\kappa\xi} & -[6 + 4\kappa^2\xi^2] e^{-2\kappa\xi} & 0 \\ 3 & -3e^{-4\kappa\xi} & 0 & -2e^{-2\kappa\xi} & -4\kappa\xi e^{-2\kappa\xi} & 0 \\ 3 & 3e^{-4\kappa\xi} & 2e^{-2\kappa\xi} & 4\kappa\xi e^{-2\kappa\xi} & [-6 + 4\kappa^2\xi^2] e^{-2\kappa\xi} & 0 \end{pmatrix}.$$

Note that the largest eigenvalue of A_0 is zero. Therefore, all columns of $Y(\xi)$ except for the first are exponentially damped (since $\kappa > 0$); the first column is an eigenvector of A_0 belonging to the eigenvalue zero. As a consequence, the solution $\mathbf{y}(\xi)$ approaches a constant vector proportional to this eigenvector in the limit of large ξ ,

$$\lim_{\xi \rightarrow \infty} \mathbf{y}(\xi) = \frac{3}{16} [C^{-1}\mathbf{y}_0]_1 \mathbf{e}_0, \quad (\text{A.2})$$

where

$$\mathbf{e}_0 \equiv (1, 1, 0, 1, 1, 1)^T,$$

and $[C^{-1}\mathbf{y}_0]_1$ denotes the first component of the vector $C^{-1}\mathbf{y}_0$.

We now formulate two different eigenvalue problems that refer to the shape functions $\psi_{bl}(\xi)$ introduced in §2.2 of chapter 4. For a given ψ_{bl} with the properties (4.44) and (4.45), both eigenvalue problems are based on the system of differential equations (4.29)–(4.34),

$$y'_1 = 2\kappa [-y_1 + y_2], \quad (\text{A.3})$$

$$y'_2 = 2\kappa \left[\frac{1}{2}y_1 - y_2 + \frac{1}{2}y_4 \right], \quad (\text{A.4})$$

$$y'_3 = -2\kappa y_3 - \frac{\sigma}{\kappa} \psi'_{bl} y_1, \quad (\text{A.5})$$

$$y'_4 = 2\kappa [-y_4 + y_5], \quad (\text{A.6})$$

$$y'_5 = 2\kappa \left[\frac{1}{4}y_1 + \frac{1}{2}y_4 - y_5 + \frac{1}{4}y_6 \right], \quad (\text{A.7})$$

$$y'_6 = 2\kappa [y_2 - y_6] + \frac{\sigma}{2\kappa} \psi'_{bl} y_3. \quad (\text{A.8})$$

The first eigenvalue problem is defined by integrating this system from 0 to $\frac{1}{2}$ with initial values (4.35),

$$\mathbf{y}(0) = (0, 0, 0, 0, 0, 1)^T, \quad (\text{A.9})$$

and boundary condition

$$\left[C^{-1} \mathbf{y} \left(\frac{1}{2} \right) \right]_1 = 0. \quad (\text{A.10})$$

With κ and ψ_{bl} as input, we search for the smallest positive value of σ which solves this boundary value problem, denoted as $\sigma^{(1)}\{\psi_{bl}\}(\kappa)$.

The second eigenvalue problem is defined by integrating the system from $\frac{1}{2}$ to 1 with initial values (4.49),

$$\mathbf{y} \left(\frac{1}{2} \right) = (1, 1, 0, 1, 1, 1)^T = \mathbf{e}_0, \quad (\text{A.11})$$

and boundary condition (4.50),

$$y_1(1) = 0. \quad (\text{A.12})$$

Again we search for the smallest positive value of σ which solves this boundary value problem, denoted as $\sigma^{(2)}\{\psi_{bl}\}(\kappa)$.

From the previous discussion it is clear that if one glues the left boundary segment of $\psi_{bl}(\xi)$ at $\xi = \frac{1}{2}$ to the constant function defined by $\psi(\xi) = \frac{1}{2}$ for $\xi > \frac{1}{2}$, takes the result as an input to the system (A.3)–(A.8), and integrates it with initial condition (A.9), then the choice $\sigma = \sigma^{(1)}$ ensures that the solution vector vanishes in the limit $\xi \rightarrow \infty$, since (A.10) sets the prefactor of \mathbf{e}_0 to zero, cf. (A.2). On the other hand, the integration of the second problem starts with this eigenvector, so that for $\sigma = \sigma^{(2)}$ the usual boundary condition posed at the end of the right boundary layer is satisfied. We remark that we do not want to treat the mathematically non-trivial questions concerning the precise properties of the functions ψ_{bl} that can guarantee the existence of the required values $\sigma^{(1)}$ and $\sigma^{(2)}$, but we rather assume that ψ_{bl} is chosen appropriately.

Returning to the evaluation of the right hand side of (4.48), we observe that

$$\lim_{\delta \rightarrow 0} \rho_0\{\psi\}(\kappa) = \min \left\{ \sigma^{(1)}\{\psi_{bl}\}(\kappa), \sigma^{(2)}\{\psi_{bl}\}(\kappa) \right\}. \quad (\text{A.13})$$

Namely, in order to determine ρ_0 we have to integrate the system (4.29)–(4.34) with ψ as input, see (4.46), and make sure that the boundary condition (4.36) is satisfied. When letting δ tend to zero, so that the length of the interior segment of ψ tends to infinity, we are faced with the following alternative at the merging point to the right boundary layer: either the solution vector vanishes, since the prefactor of \mathbf{e}_0 is zero, and consequently the solution will remain the zero-vector in the right boundary layer, or the solution vector is proportional to \mathbf{e}_0 . In the first case

the eigenvalue ρ_0 is by construction equal to $\sigma^{(1)}$, in the second case equal to $\sigma^{(2)}$. Reverting this argument, if $\sigma^{(1)}$ and $\sigma^{(2)}$ have been determined from their eigenvalue problems, two candidates for $\lim_{\delta \rightarrow 0} \rho_0$ have been found. Since ρ_0 is defined as the smallest positive eigenvalue, (A.13) follows. In the rest of this appendix we will show that $\sigma^{(1)}$ and $\sigma^{(2)}$ are actually equal.

To create a link between the two eigenvalue problems, we have to consider a third one. For a given shape function ψ_{bl} we take an ϵ with $-1 < \epsilon < 1$, and define the function

$$\psi_\epsilon(\xi) \equiv \begin{cases} (1 + \epsilon) \psi_{bl}(\xi) & \text{for } 0 \leq \xi \leq \frac{1}{2} \\ \frac{1}{2} (1 + \epsilon) & \text{for } \frac{1}{2} < \xi < \ell + \frac{1}{2} \\ 1 - (1 - \epsilon) \psi_{bl}(\ell + 1 - \xi) & \text{for } \ell + \frac{1}{2} \leq \xi \leq \ell + 1 \end{cases} .$$

This function equals $\psi(\xi)$ as introduced in (4.46), if we set $\epsilon = 0$ and $\ell = (2\delta)^{-1} - 1$. Note that ϵ plays the role of an asymmetry parameter: the constant interior segment is shifted by an amount of $\epsilon/2$ with respect to the previous value $\frac{1}{2}$. Such a shift will turn out to be the key for connecting the eigenvalues $\sigma^{(1)}$ and $\sigma^{(2)}$.

Our third eigenvalue problem again arises from the system (A.3)–(A.8), but now considered in the interval $[0, \ell + 1]$, and the input function ψ_{bl} is replaced by ψ_ϵ . The initial values (A.9) are supplemented by the boundary condition

$$y_1(\ell + 1) = 0.$$

The smallest positive eigenvalue σ will now be written as $\sigma_\ell\{\psi_{bl}\}(\epsilon, \kappa)$.

At this point we resort to a symmetry property of the actual physical problem, namely the point symmetry with respect to $(x = 0, z = \frac{1}{2})$. This symmetry manifests itself in the fact that the spectra of the eigenvalue problem (3.13) for some fixed R and two different functions $\phi_1(z)$ and $\phi_2(z)$ are identical, if both functions are continuously differentiable and satisfy the boundary conditions at $z = 0$ and $z = 1$, and are related by $\phi_2(z) = 1 - \phi_1(1 - z)$. It is *not* required that the two functions obey the profiles’ symmetry condition. Since σ_ℓ corresponds to the passage of the lowest eigenvalue through zero, and since the differential equations depend only on the *absolute* value of the wavenumber, the relation

$$\psi_{-\epsilon}(\xi) = 1 - \psi_\epsilon(\ell + 1 - \xi)$$

leads to the key equation

$$\sigma_\ell\{\psi_{bl}\}(\epsilon, \kappa) = \sigma_\ell\{\psi_{bl}\}(-\epsilon, \kappa). \tag{A.14}$$

Taking the limit $\ell \rightarrow \infty$,

$$\lim_{\ell \rightarrow \infty} \sigma_\ell \{\psi_{bl}\}(\epsilon, \kappa) \equiv \sigma_\infty \{\psi_{bl}\}(\epsilon, \kappa),$$

(A.14) yields

$$\sigma_\infty \{\psi_{bl}\}(\epsilon, \kappa) = \sigma_\infty \{\psi_{bl}\}(-\epsilon, \kappa). \quad (\text{A.15})$$

We can now formulate the

Lemma A.1.1 *Let $\psi_{bl}(\xi)$ be a shape function for the boundary layers. Then we have for all $\kappa > 0$ the identity*

$$\sigma^{(1)} \{\psi_{bl}\}(\kappa) = \sigma^{(2)} \{\psi_{bl}\}(\kappa). \quad (\text{A.16})$$

Proof. For each shape function $\psi_{bl}(\xi)$, rescaled wavenumber $\kappa > 0$, and ϵ taken from the interval $(-1, 1)$, we define

$$\tilde{\sigma}^{(1)} \{\psi_{bl}\}(\epsilon, \kappa)$$

as the smallest positive value of σ for which the boundary value problem posed by (A.3)–(A.8) with $\psi_{bl}(\xi)$ replaced by $(1 + \epsilon) \psi_{bl}(\xi)$, initial values (A.9), and boundary value (A.10) is solved. Likewise, be

$$\tilde{\sigma}^{(2)} \{\psi_{bl}\}(\epsilon, \kappa)$$

the smallest positive value of σ for which the boundary value problem posed by (A.3)–(A.8) with $\psi_{bl}(\xi)$ replaced by $1 - (1 - \epsilon) \psi_{bl}(1 - \xi)$, initial values (A.11), and boundary value (A.12) is satisfied. Because the system (A.3)–(A.8) depends on σ only through the product $\sigma \psi'_{bl}(\xi)$, we obtain

$$\begin{aligned} \tilde{\sigma}^{(1)} \{\psi_{bl}\}(\epsilon, \kappa) &= \frac{1}{1 + \epsilon} \sigma^{(1)} \{\psi_{bl}\}(\kappa), \\ \tilde{\sigma}^{(2)} \{\psi_{bl}\}(\epsilon, \kappa) &= \frac{1}{1 - \epsilon} \sigma^{(2)} \{\psi_{bl}\}(\kappa). \end{aligned}$$

In analogy to the preceding discussion we deduce

$$\lim_{\ell \rightarrow \infty} \sigma_\ell \{\psi_{bl}\}(\epsilon, \kappa) = \sigma_\infty \{\psi_{bl}\}(\epsilon, \kappa) = \min \left\{ \tilde{\sigma}^{(1)} \{\psi_{bl}\}(\epsilon, \kappa), \tilde{\sigma}^{(2)} \{\psi_{bl}\}(\epsilon, \kappa) \right\}.$$

Thus, (A.15) produces the equation

$$\min \left\{ \frac{1}{1+\epsilon} \sigma^{(1)} \{\psi_{bl}\}(\kappa), \frac{1}{1-\epsilon} \sigma^{(2)} \{\psi_{bl}\}(\kappa) \right\} = \min \left\{ \frac{1}{1-\epsilon} \sigma^{(1)} \{\psi_{bl}\}(\kappa), \frac{1}{1+\epsilon} \sigma^{(2)} \{\psi_{bl}\}(\kappa) \right\}. \quad (\text{A.17})$$

If we now assume that $\sigma^{(1)} \neq \sigma^{(2)}$, we may stipulate without loss of generality that $\sigma^{(1)} < \sigma^{(2)}$. Then we choose $0 < \epsilon < 1$ such that

$$\frac{1}{1-\epsilon} \sigma^{(1)} \{\psi_{bl}\}(\kappa) < \frac{1}{1+\epsilon} \sigma^{(2)} \{\psi_{bl}\}(\kappa),$$

and conclude from (A.17)

$$\frac{1}{1+\epsilon} \sigma^{(1)} \{\psi_{bl}\}(\kappa) = \frac{1}{1-\epsilon} \sigma^{(1)} \{\psi_{bl}\}(\kappa).$$

This equation requires $\sigma^{(1)} = 0$, which contradicts the proposition $\sigma^{(1)} > 0$. Hence, we necessarily have $\sigma^{(1)} = \sigma^{(2)}$. \square

Applying this lemma to (A.13), we finally obtain

$$\lim_{\delta \rightarrow 0} \rho_0 \{\psi\}(\kappa) = \sigma^{(1)} \{\psi_{bl}\}(\kappa) = \sigma^{(2)} \{\psi_{bl}\}(\kappa). \quad (\text{A.18})$$

By definition, $\sigma^{(2)} \{\psi_{bl}\}(\kappa)$ is identical to $\sigma_0 \{\psi_{bl}\}(\kappa)$ as employed in §2.2 of chapter 4.

A.2 Compound matrix method for the sixth-order Sturm–Liouville problem

Keeping in mind that we are not interested in the calculation of the entire spectrum furnished by the Sturm–Liouville eigenvalue problem (5.8) and (5.9), but in the determination of that value of R where the smallest eigenvalue passes through zero, we can set $\lambda = 0$ right from the outset. We thus obtain the new sixth-order Sturm–Liouville problem

$$\begin{aligned} v_z^{(6)} - 2 \frac{\phi^{(2)}}{\phi'} v_z^{(5)} - \left\{ 3k^2 + \frac{\phi^{(3)}}{\phi'} - 2 \left(\frac{\phi^{(2)}}{\phi'} \right)^2 \right\} v_z^{(4)} + \left\{ 4k^2 \frac{\phi^{(2)}}{\phi'} + i k_x R \phi' \right\} v_z^{(3)} \\ + \left\{ 3k^4 + 2k^2 \left[\frac{\phi^{(3)}}{\phi'} - 2 \left(\frac{\phi^{(2)}}{\phi'} \right)^2 \right] + i \frac{k_x}{2} R \phi^{(2)} \right\} v_z^{(2)} \end{aligned}$$

$$\begin{aligned}
& - \left\{ 2k^4 \frac{\phi^{(2)}}{\phi'} + ik_x R \left[k^2 \phi' - \phi^{(3)} + \frac{(\phi^{(2)})^2}{\phi'} \right] \right\} v'_z \\
& - \left\{ k^6 + k^4 \left[\frac{\phi^{(3)}}{\phi'} - 2 \left(\frac{\phi^{(2)}}{\phi'} \right)^2 \right] - \frac{1}{4} (k_y R \phi')^2 + \right. \\
& \quad \left. i \frac{k_x}{2} R \left[k^2 \phi^{(2)} - \phi^{(4)} + 3 \frac{\phi^{(3)} \phi^{(2)}}{\phi'} - 2 \frac{(\phi^{(2)})^3}{(\phi')^2} \right] \right\} v_z = 0,
\end{aligned} \tag{A.19}$$

together with the boundary conditions

$$v_z(z)|_{z=0,1} = 0, \quad v'_z(z)|_{z=0,1} = 0, \quad \text{and} \quad \left[v_z^{(2)}(z) - \frac{1}{2k^2} v_z^{(4)}(z) \right] \Big|_{z=0,1} = 0. \tag{A.20}$$

The eigenvalues of this problem are those values of R where both equations (A.19) and (A.20) are satisfied.

In order to integrate (A.19), one has to pose suitable initial conditions at one of the boundaries, let us say $z = 0$. We define the six-vectors

$$\mathbf{V}_z(z) \equiv \left(v_z(z), v'_z(z), v_z^{(2)}(z) - \frac{1}{2k^2} v_z^{(4)}(z), v_z^{(3)}(z), v_z^{(4)}(z), v_z^{(5)}(z) \right)^T,$$

and consider the three linearly independent fundamental solutions $\mathbf{V}_{z,1}(z)$, $\mathbf{V}_{z,2}(z)$, and $\mathbf{V}_{z,3}(z)$ to (A.19) that emerge from the initial values

$$\left. \begin{aligned}
& \mathbf{V}_{z,1}(0) = (0, 0, 0, 1, 0, 0)^T, \quad \mathbf{V}_{z,2}(0) = (0, 0, 0, 0, 1, 0)^T, \\
& \text{and } \mathbf{V}_{z,3}(0) = (0, 0, 0, 0, 0, 1)^T,
\end{aligned} \right\} \tag{A.21}$$

respectively. By construction, each of these three solutions satisfies the conditions (A.20) at $z = 0$, and the most general solution obeying these one-sided b.c. is just a superposition of them. That solution which also satisfies the conditions (A.20) at the other boundary $z = 1$ is then singled out by the requirement

$$\text{Det} \begin{pmatrix} v_{z,1}(1) & v_{z,2}(1) & v_{z,3}(1) \\ v'_{z,1}(1) & v'_{z,2}(1) & v'_{z,3}(1) \\ v_{z,1}^{(2)}(1) - \frac{1}{2k^2} v_{z,1}^{(4)}(1) & v_{z,2}^{(2)}(1) - \frac{1}{2k^2} v_{z,2}^{(4)}(1) & v_{z,3}^{(2)}(1) - \frac{1}{2k^2} v_{z,3}^{(4)}(1) \end{pmatrix} = 0.$$

But from the numerical point of view the evaluation of this determinant, which in most cases necessitates to subtract large numbers of almost equal magnitude from each other, is rather

inconvenient. An efficient and numerically stable way to bypass this difficulty has become known as *compound matrix method* in the literature, see e.g. Straughan (1992) for an introduction to the method, or §3 of chapter 3 for the application to the restricted Couette problem. For applying this technique to the full Couette problem studied in this chapter, we define a new vector $\mathbf{y}(z) = (y_1(z), \dots, y_{20}(z))^T$, the 20 components of which are proportional to the 3×3 minors of the 6×3 solution matrix that contains $\mathbf{V}_{z,1}$ as its first, $\mathbf{V}_{z,2}$ as its second, and $\mathbf{V}_{z,3}$ as its third column:

$$\begin{aligned} y_1 &\equiv k^9 \sum_{\sigma} \text{sign}(\sigma) v_{z,\sigma(1)} v'_{z,\sigma(2)} \left(v_{z,\sigma(3)}^{(2)} - \frac{1}{2k^2} v_{z,\sigma(3)}^{(4)} \right), \\ &\vdots \\ y_{20} &\equiv \sum_{\sigma} \text{sign}(\sigma) v_{z,\sigma(1)}^{(3)} v_{z,\sigma(2)}^{(4)} v_{z,\sigma(3)}^{(5)}. \end{aligned} \tag{A.22}$$

The summations involve all permutations σ of 1, 2, 3. The powers of k multiplying each sum are determined in the following way: the expression defining y_{20} carries the highest total number of derivatives, namely 12; this expression is multiplied by k^0 . Descending in the index from 20 to 1, the number of derivatives is successively diminished; each derivative less gives a factor of k more. This guarantees two things: firstly, the initial conditions (5.13) are independent of k , and secondly, all components have the same order of magnitude.

From (A.19) one then obtains a system of first-order equations that already closely resembles the system (5.12) which we have studied numerically, with the only difference that in each component i ($i = 1, \dots, 20$) the term $-3k y_i$ appearing in (5.12) is still missing. It is obvious that the initial conditions (5.13) and the boundary condition (5.14) follow directly from (A.21) and the definitions (A.22).

This term $-3k y_i$ in the i -th component of the system is of particular importance. The restricted Couette problem has taught us the lesson that the system of first-order equations directly provided by the compound matrix method is not suited for numerical analysis in the high- Re -regime, where one has to monitor large values of k . One rather has to rescale each component of the system by a common exponential damping factor. The reason for this rescaling is related to the fact that the optimized profiles tend to become flat in the interior of the fluid layer when Re becomes high, while the extension of the boundary segments, where the profiles have to bend in order to meet the boundary conditions $\phi(0) = 0$ and $\phi(1) = 1$, tends to zero. This motivates to neglect the profiles' boundary conditions altogether, and to consider (A.19) with a linear profile $\phi(z) = cz$, so that ϕ' becomes equal to the constant c , and all higher profile derivatives vanish. In the limit $c \rightarrow 0$ one then arrives at

$$v_z^{(6)} - 3k^2 v_z^{(4)} + 3k^4 v_z^{(2)} - k^6 v_z = 0, \tag{A.23}$$

with the b.c. (A.20). Applying the compound matrix technique as sketched above to this boundary value problem, one finds a 20-component system of first-order equations as in the case of a general ϕ , but now with constant coefficients. This system can be solved analytically by standard means, but an accurate numerical solution for large k 's will be possible only if the solutions do not grow (or decrease) exponentially. Thus, the intended numerical approach forces us to rescale the system such that the largest eigenvalue of the rescaled system's coefficient matrix is exactly equal to zero. It turns out to be possible to determine the Jordan normal form of the 20×20 matrix resulting from (A.23) analytically; the largest eigenvalue is non-degenerate and equals $3k$. Hence, the transformation

$$\tilde{y}_1(z) \equiv y_1(z) e^{-3kz}, \quad \dots, \quad \tilde{y}_{20}(z) \equiv y_{20}(z) e^{-3kz}, \quad (\text{A.24})$$

has the desired effect. Applying the very same transformation also to the system given by the compound matrix method for the case of a general candidate profile ϕ (and finally omitting the tilde-signs), changes that system merely by adding $-3k y_i$ to the i -th component, and thus produces our system (5.12). We emphasize that the identification of the proper exponential scaling factor, and the actual scaling transformation (A.24), is crucial for obtaining equations that remain numerically stable even in the regime of asymptotically high Reynolds numbers.

A striking feature found in the study of the restricted Couette problem, where the system corresponding to (5.12) consists of merely six equations, is the possibility to reduce that *complex* 6-component system to a *real* 6-component system, thereby halving the number of equations. This simplification could be obtained from taking $\text{Im}(y_1(z)) = 0$, for all z . Even though we have strong numerical evidence that the imaginary part of the component $y_1(z)$ vanishes also in the present case, we did not succeed in deriving a reduced system for arbitrary ϕ . Hence, we make a virtue of necessity and keep the full system (5.12), but exploit our insight for controlling the accuracy of the numerical solutions by monitoring the magnitude of $\text{Im}(y_1(z))$.

A.3 Neglecting divergence-freeness

In this appendix we study the variational problem for energy dissipation in plane Couette flow without requiring that the solutions $\mathbf{V}(\mathbf{x})$ to the eigenvalue problem (3.13) be divergence-free. Then the solutions to this eigenvalue problem are determined in an enlarged space of functions, so that the bound obtainable for this simplified problem can naturally not be as good as the one reported in § 3 of chapter 5. However, the distinct value of this toy model lies in two points. Firstly, we can illustrate, condensed in a nutshell, the principles of both the background flow method itself and the use of the compound matrix technique. Secondly, this model allows an immediate quantitative comparison of our numerically calculated, asymptotic dissipation bound with the corresponding value provided by the Howard–Busse theory.

To begin with, the equations (5.1)–(5.4) for the spectral constraint’s eigenvalue problem simplify enormously when the condition $\nabla \cdot \mathbf{V} = 0$ is skipped:

$$\lambda v_x = -2 \left(\partial_z^2 - k^2 \right) v_x + R \phi' v_z, \quad (\text{A.25})$$

$$\lambda v_y = -2 \left(\partial_z^2 - k^2 \right) v_y, \quad (\text{A.26})$$

$$\lambda v_z = -2 \left(\partial_z^2 - k^2 \right) v_z + R \phi' v_x. \quad (\text{A.27})$$

Equation (A.26) separates from the others, and we immediately obtain a solution that is compatible with the b.c. (5.5) for each λ and k , namely $v_y(z) = 0$. Introducing the new functions $v(z) \equiv v_x(z) - v_z(z)$ and $w(z) \equiv v_x(z) + v_z(z)$, (A.25) and (A.27) transform into

$$\begin{aligned} \lambda v &= -2 \left(\partial_z^2 - k^2 \right) v - R \phi' v, \\ \lambda w &= -2 \left(\partial_z^2 - k^2 \right) w + R \phi' w; \end{aligned}$$

the b.c. read $v(0) = w(0) = 0$ and $v(1) = w(1) = 0$.

We now assume that the profile functions $\phi(z)$ satisfy, besides the b.c. posed in (3.10) and the symmetry requirement $\phi(z) = 1 - \phi(1 - z)$, also the additional monotony condition

$$\phi'(z) \geq 0 \quad \text{for} \quad 0 \leq z \leq 1. \quad (\text{A.28})$$

Our test profiles (5.17) obviously comply with this plausible requirement. Hence, if the component $w(z)$ does not vanish identically, the positive-definiteness of $-\partial_z^2$ will enforce $\lambda > 0$ for positive R . Consequently, for $\lambda = 0$ and $R > 0$ we have $w(z) = 0$, and are left with the second-order Sturm–Liouville boundary value problem

$$v'' - \left(k^2 - \frac{1}{2} R \phi' \right) v = 0, \quad v(0) = v(1) = 0. \quad (\text{A.29})$$

In exact analogy to the full problem, the main task posed by the spectral constraint is to calculate for given ϕ and $k \geq 0$ the smallest R -value $R_0\{\phi\}(k)$ where (A.29) is fulfilled, and then to minimize over all k in order to extract $R_c\{\phi\}$. But now the second-order differential equation (A.29) shows that the *minimizing k -value* $k_c\{\phi\}$ equals zero for each $\phi(z)$. In the final step, the optimal upper bound on $c_\varepsilon(Re)$ follows from inequality (3.18).

The laminar profile $\phi(z) = z$ yields the “energy stability limit” for our toy problem,

$$Re_{ES} = 2\pi^2 \approx 19.74, \quad c_\varepsilon(Re_{ES}) = 1/2\pi^2 \approx 0.05066.$$

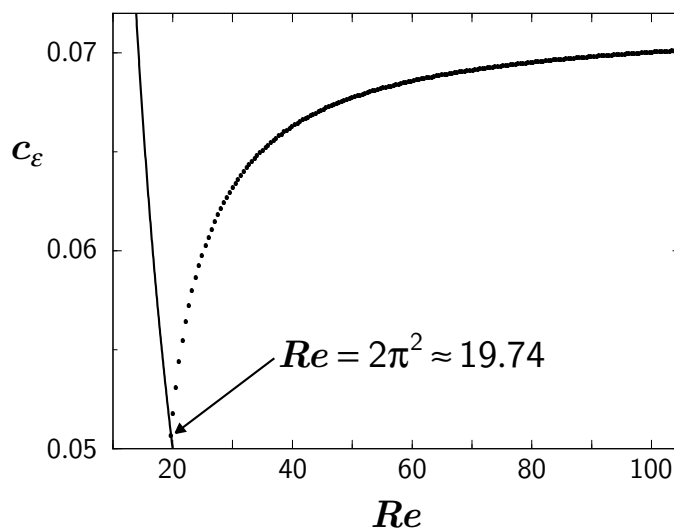


Figure A.1: Bounds on $c_\varepsilon(Re)$ for the plane Couette flow obtained by neglecting the condition $\nabla \cdot \mathbf{V} = 0$ in the eigenvalue equations (3.13). Points denote the variational upper bound $\bar{c}_\varepsilon(Re)$, computed numerically from the test profiles (5.17) with fixed parameter $n = 2$; the solid line on the left is the lower bound $\underline{c}_\varepsilon(Re) = Re^{-1}$.

In order to compute $R_c\{\phi\}$ for non-laminar profiles we now rewrite the second-order equation (A.29) as a system of first-order equations by defining the vector $\mathbf{y}(z) \equiv (v(z), v'(z))^T$. In this way we get

$$y_1' = y_2, \quad y_2' = -\frac{1}{2}R\phi' y_1, \quad (\text{A.30})$$

where we have set $k = 0$; initial conditions at $z = 0$ and b.c. at $z = 1$ are given by

$$\mathbf{y}(0) = (0, 1)^T, \quad y_1(1) = 0. \quad (\text{A.31})$$

This reformulation of the Sturm–Liouville problem (A.29) corresponds precisely to the reformulation provided by the compound matrix method. If one compares this simple boundary value problem (A.30, A.31) to the corresponding boundary value problem (5.12)–(5.14), one gets a vivid impression of the complications introduced into the variational principle by the condition $\nabla \cdot \mathbf{V} = 0$.

Figure A.1 shows the numerically computed variational upper bound on $c_\varepsilon(Re)$ that results from inequality (3.12) when $\nabla \cdot \mathbf{V} = 0$ is neglected, i.e. when the spectral constraint is translated into

(A.30, A.31), and the previous test profiles (5.17) are employed. For simplicity, we have fixed the parameter n to the value $n = 2$. Interestingly, this bound exhibits the same shape as the one that had been found analytically in chapter 2 when another over-restrictive profile constraint stemming from functional estimates had been used instead of the actual spectral constraint; that bound is indicated by the long-dashed line in figure 5.9. The best possible asymptotic upper bound $\overline{c}_\varepsilon(Re)$ for the toy model without $\nabla \cdot \mathbf{V} = 0$ can be found for a non-integer value of n , namely $n_\infty \approx 3.40$:

$$\lim_{Re \rightarrow \infty} \overline{c}_\varepsilon(Re) \approx 0.07071.$$

This value has to be compared to the bound calculated analytically by Howard (1972), also without accounting for divergence-freeness:

$$\lim_{Re \rightarrow \infty} \overline{c}_\varepsilon(Re) = \frac{9}{128} \approx 0.07031.$$

The work of Kerswell (1997) suggests that both the Howard–Busse theory and the background flow method, when fully exhausted, give the same asymptotic upper bound. Even though we have deliberately used test profiles which are *not* specifically adapted to the present toy model, we have missed Howard’s bound by merely 0.57%.

Bibliography

- [Busse (1970)] BUSSE, F. H. 1970 Bounds for turbulent shear flow. *J. Fluid Mech.* **41**, 219–240.
- [Busse (1978)] BUSSE, F. H. 1978 The Optimum Theory of turbulence. *Adv. Appl. Mech.* **18**, 77–121.
- [Busse (1996)] BUSSE, F. H. 1996 Bounds for properties of complex systems. In *Nonlinear physics of complex systems — current status and future trends* (eds. J. Parisi, S. C. Müller & W. Zimmermann). Lecture Notes in Physics, vol. 476, pp. 1–9. Springer.
- [Constantin & Doering (1995)] CONSTANTIN, P. & DOERING, C. R. 1995 Variational bounds on energy dissipation in incompressible flows. II. Channel flow. *Phys. Rev. E* **51**, 3192–3198.
- [Drazin & Reid (1981)] DRAZIN, P. G. & REID, W. H. 1981 *Hydrodynamic stability*. Cambridge University Press.
- [Doering & Constantin (1992)] DOERING, C. R. & CONSTANTIN, P. 1992 Energy dissipation in shear driven turbulence. *Phys. Rev. Lett.* **69**, 1648–1651.
- [Doering & Constantin (1994)] DOERING, C. R. & CONSTANTIN, P. 1994 Variational bounds on energy dissipation in incompressible flows: shear flow. *Phys. Rev. E* **49**, 4087–4099.
- [Doering & Constantin (1996)] DOERING, C. R. & CONSTANTIN, P. 1996 Variational bounds on energy dissipation in incompressible flows. III. Convection. *Phys. Rev. E* **53**, 5957–5981.
- [Doering & Hyman (1997)] DOERING, C. R. & HYMAN, J. M. 1997 Energy stability bounds on convective heat transport: numerical study. *Phys. Rev. E* **55**, 7775–7778.
- [Gebhardt *et al.* (1995)] GEBHARDT, T., GROSSMANN, S., HOLTHAUS, M. & LÖHDEN, M. 1995 Rigorous bound on the plane-shear-flow dissipation rate. *Phys. Rev. E* **51**, 360–365.
- [Grossmann (1995)] GROSSMANN, S. 1995 Asymptotic dissipation rate in turbulence. *Phys. Rev. E* **51**, 6275–6277.
- [Heisenberg (1948)] HEISENBERG, W. 1948 Zur statistischen Theorie der Turbulenz. *Z. Phys.* **124**, 628–657.
- [Hopf (1941)] HOPF, E. 1941 Ein allgemeiner Endlichkeitssatz der Hydrodynamik. *Math. Annalen* **117**, 764–775.

- [Howard (1972)] HOWARD, L. N. 1972 Bounds on flow quantities. *Ann. Rev. Fluid Mech.* **4**, 473–494.
- [Joseph (1976)] JOSEPH, D. D. 1976 *Stability of fluid motions I & II*. Springer.
- [Kerswell (1997)] KERSWELL, R. R. 1997 Variational bounds on shear-driven turbulence and turbulent Boussinesq convection. *Physica D* **100**, 355–376.
- [Kerswell & Soward (1996)] KERSWELL, R. R. & SOWARD, A. M. 1996 Upper bounds for turbulent Couette flow incorporating the poloidal power constraint. *J. Fluid Mech.* **328**, 161–176.
- [Kolmogorov (1941)] KOLMOGOROV, A. N. 1941 The local structure of turbulence in incompressible viscous fluid for very large Reynolds numbers. *C. R. Acad. Nauk USSR* **30**, 301–305.
- [Lathrop, Fineberg & Swinney (1992)] LATHROP, D. P., FINEBERG, J. & SWINNEY, H. L. 1992 Turbulent flow between concentric rotating cylinders at large Reynolds number. *Phys. Rev. Lett.* **68**, 1515–1518.
- [Marchioro (1994)] MARCHIORO, C. 1994 Remark on the energy dissipation in shear driven turbulence. *Physica D* **74**, 395–398.
- [Nicodemus, Grossmann & Holthaus (1997a)] NICODEMUS, R., GROSSMANN, S. & HOLTHAUS, M. 1997a Improved variational principle for bounds on energy dissipation in turbulent shear flow. *Physica D* **101**, 178–190.
- [Nicodemus, Grossmann & Holthaus (1997b)] NICODEMUS, R., GROSSMANN, S. & HOLTHAUS, M. 1997b The background flow method. Part 1. Constructive approach to bounds on energy dissipation. *Preprint* (1997).
- [Nicodemus, Grossmann & Holthaus (1997c)] NICODEMUS, R., GROSSMANN, S. & HOLTHAUS, M. 1997c The background flow method. Part 2. Asymptotic theory of dissipation bounds. *Preprint* (1997).
- [Nicodemus, Grossmann & Holthaus (1997d)] NICODEMUS, R., GROSSMANN, S. & HOLTHAUS, M. 1997d Variational bound on energy dissipation in plane Couette flow. *Preprint* (1997).
- [Nicodemus, Grossmann & Holthaus (1997e)] NICODEMUS, R., GROSSMANN, S. & HOLTHAUS, M. 1997e Variational bound on energy dissipation in turbulent shear flow. *Preprint* (1997).
- [Obukhov (1941)] OBUKHOV, A. M. 1941 On the distribution of energy in the spectrum of turbulent flow. *C. R. Acad. Nauk USSR* **32**, 22–24.
- [Onsager (1945)] ONSAGER, L. 1945 The distribution of energy in turbulence. *Phys. Rev.* **68**, 285.

- [Reichardt (1959)] REICHARDT, H. 1959 Gesetzmäßigkeiten der geradlinigen turbulenten Couetteströmung. *Mitteilungen aus dem Max-Planck-Institut für Strömungsforschung*. Göttingen, No. 22.
- [Stolovitzky & Sreenivasan (1995)] STOLOVITZKY, G. & SREENIVASAN, K. R. 1995 Intermittency, the second-order structure function, and the turbulent energy-dissipation rate. *Phys. Rev. E* **52**, 3242–3244.
- [Straughan (1992)] STRAUGHAN, B. 1992 *The energy method, stability, and nonlinear convection*. Springer.
- [von Weizsäcker (1948)] VON WEIZSÄCKER, C. F. 1948 Das Spektrum der Turbulenz bei großen Reynoldsschen Zahlen. *Z. Phys.* **124**, 614–627.